Preoperative Image-guided Transcranial Histotripsy for Brain Cancer Treatment

by

Sang Won Choi

A dissertation submitted in partial fulfillment
of the requirements for the degree of
Doctor of Philosophy
(Biomedical Engineering)
in the University of Michigan
2023

Doctoral Committee:

Professor Zhen Xu, Chair
Professor J. Brian Fowlkes
Research Scientist Timothy L. Hall
Professor Aditya S. Pandey
Associate Research Scientist Jonathan R. Sukovich

Sang Won Choi

csangwon@umich.edu

ORCID iD: 0000-0001-8532-0756

Dedication

For the anatomical donors and research animals

For the all the wonderful people who have helped me to where I am today

Acknowledgements

I would like to acknowledge and thank all the people who have taught me lessons throughout my Ph.D. I would like to start by thanking my advisor and my mentor Dr. Zhen Xu. She has been extremely patient with me throughout the years of graduate school here at the University of Michigan. She has taught me to grow as a scientist, an engineer, and a person. She has taught me many transferable skills such as oral and written communication, attention to detail, project management, and perspective switch, and I hope to keep cultivating these skills. I would also like to thank the committee members: Dr. Brian Fowlkes, Dr. Aditya Pandey, Dr. Timothy Hall, and Dr. Jonathan Sukovich. Dr. Fowlkes has been just a great resource due to his attention to detail and his curiosity. He has provided me with great insights and questions about my research when I am too lost in the details. Dr. Aditya Pandey has always provided enthusiasm and encouragement for our work. Even when we think our work is trivial, he never failed to give appreciation for our work and shower us with compliments to motivate us in our journey. Without Dr. Timothy Hall, none of the systems evaluated in this dissertation or the experiments would have been possible. He has been the best resource for setting up experiments and taught me foundational laboratory skills with patience. Dr. Sukovich has been another indispensable resource when it comes to cavitation physics and experimental setups. His calm disposure in all situations and thought processes for transcranial histotripsy research have helped me through the journey, and it has been a privilege to work in a team with such an intelligent and humble person.

In addition to my committee, I would like to thank all my histotripsy laboratory former and current members: Jonathan Macoskey, Jonathan Lundt, Tyler Gerhardson, Tejaswi Worlikar,

Hedieh Tamaddoni, Yige Li, Ryan Hubbard, Ning Lu, Greyson Stocker, Ellen Yeats, Scott Haskell, Christina Hendren, Sarah Duclos, Dinank Gupta, Reliza Mcginnis, Tarana Kaovasia, Mikey Komaiha, and Hanna Kim. Without them, the laboratory culture will not have been the same. They have been a very pleasant group of people to work with and I am thankful for their kindness and patience. Our little banters and discussions in the laboratory were a huge positive element in my Ph.D.

I would also like to acknowledge and thank the staff: Dave Choi, Adam Fox, Maria Steele, Rebecca Green, and others in the biomedical engineering department here at the University of Michigan. They have been great resources inside and outside of the laboratory environment, guiding me through what papers to fill out so that I can do graduate school step by step. Staff outside of biomedical engineering programs such as the art and architecture, Duderstadt fabrication lab, Anatomical Donations Program, Michigan Medicine Hospital radiology, Moving & Trucking, etc. Everyone has taken a significant part in my Ph.D. journey and without them, none of the experiments would have been possible.

Now finally to my family and friends, Gy Won, Michele, mom, dad, Jakin, Ravi, Chris, Laura, Kelly, Tim, Egg, Danner, Nick, Nic, Yunus, Pieter, Stephen, Harrison, Samuel, Eric, Julia, Rob, Brian and all those who touched my heart and supported me through the last five years; and also to my Union folks, Dr. Buma, Ben^2, Dan, Brendan, Jamal, Tariq, Harrisonn, and other brothers. Without the moments and conversations we shared, this Ph.D. would not have been the same. I want to thank them for helping me go through tough times, sharing their life views, introducing me to hot sauces, showing me great music, going to tailgates, letting me crash in their couches, plotting against me in stackcups, celebrating Saint Patrick's Day, playing card games, lifting large weights, and just making every ordinary activity extraordinary.

In addition to great research, this Ph.D. journey was full of unforgettable moments with exceptional people. I am deeply grateful and humbled by the opportunity to have shared these moments with you.

Table of Contents

List of Tables

List of Figures

Abstract

Malignant brain tumors remain deadly with a 36% five-year survival rate and 5% for glioblastoma (GBM), the most aggressive and prevalent form of malignant brain tumor. The current standard of care includes invasive surgery guided by preoperative images. This invasive surgery can lead to further morbid complications such as bleeding or healthy brain tissue damage. Less invasive surgical options under investigation include laser interstitial thermal therapy (LITT) and magnetic resonance-guided focused ultrasound (MRgFUS). They both require real-time MR guidance for intraoperative monitoring and this requirement leads to limited availability and expensive cost.

Histotripsy is a noninvasive cavitational ultrasound surgical method that has shown great promise as a neurosurgical technology. This dissertation presents the first preoperative image-guided transcranial histotripsy targeting platform for brain tumor treatment, the first radiological follow-up study after transcranial histotripsy, and the first study on the state of the blood-brain barrier (BBB) after histotripsy. The first chapter introduces preoperative image guidance, brain tumors, the current standard of care, investigative ablation modalities, the mechanism of transcranial histotripsy, and the potential of transcranial histotripsy as a neurosurgical interventional tool.

The second chapter discusses in detail the development of a focused ultrasound stereotactic platform for *in vivo* transcranial histotripsy of murine brains. The stereotactic procedure was guided by preoperative MRI, and the platform was analyzed for sources of error contributing to the targeting uncertainty. The entire system was calibrated using red blood cell (RBC) clot

phantoms. The targeting accuracy of the calibrated system was demonstrated with an in vivo mouse glioblastoma (GBM) model. The accuracy was quantified by the absolute distance difference between the prescribed and ablated points visible on the pre-treatment and post-treatment MR images, respectively. A pre-calibration phantom study (N = 6) resulted in an error of 0.32 ± 0.31, 0.72 ± 0.16, and 1.06 ± 0.38 mm in axial, lateral, and elevational axes, respectively. A post-calibration phantom study (N = 8) demonstrated a residual error of 0.09 ± 0.01, 0.15 ± 0.09, and 0.47 ± 0.18 mm in axial, lateral, and elevational axes, respectively. The calibrated system showed significantly reduced error of 0.20 ± 0.21, 0.34 ± 0.24, and 0.28 ± 0.21 mm in axial, lateral, and elevational axes, respectively, in the in vivo GBM tumor-bearing mice (N = 10).

The third chapter investigates the transcranial histotripsy MRI and histological findings in both normal mice with and without brain tumors and evaluates the changes over time. The stereotactic system developed in the previous chapter was used to treat normal mice and orthotopic GL261 tumor-bearing mice. The tumor burden at the time of treatment was ~3-5mm^3. T2, T2*, T1, and T1-gadolinium (Gd) MR images and H&E histology were acquired on days 0, 2, and 7 for tumor-bearing mice and days 0, 2, 7, 14, 21, and 28 for normal mice. Three mice were used for each time point and the MR images and H&E slides were interpreted by a neuroradiologist and a neuropathologist. T2 best showed anatomical feature changes due to the treatment, T2* the histotripsy ablation, T1 the blood product evolution from oxygenated blood to hemosiderin, and T1-Gd the BBBO that arises from a tumor or histotripsy ablation. These results provide a library of radiological features related to histology and will help better monitor animals in future histotripsy *in vivo* experiments.

The fourth chapter investigates the BBBO induced by transcranial histotripsy for the first time and studies how BBB at the periphery of the histotripsy ablation zone changes over time post-

histotripsy with MRI and tight junction protein (TJP) staining. Fifteen BL6 female healthy mice were treated with the stereotactic transcranial histotripsy platform. T1-gadolinium (Gd) MR images, H&E histology, and TJP-stained (Claudin-5 and Zonula Occludens-1 (ZO-1)) slides of the brain were acquired on days 0, 7, 14, 21, and 28 post-histotripsy (N= 3 at each time point). Analysis of T1-Gd MRI showed that the hyperintense BBBO area was increased for the first 7 days and subsided gradually over time. The area in the center of the histotripsy ablation, showed complete loss of the ZO-1 and claudin-5 immunostaining immediately post histotripsy, while at the border of the ablation, partial recovery of TJ complex was observed on day 7 post-histotripsy, and near-complete recovery of TJ complex was observed on day 21. These results provide the first evidence of transcranial histotripsy-induced BBBO.

The fifth chapter discusses the development of the first neuronavigation-guided transcranial histotripsy (NaviTH). The NaviTH system consists of a 360-element 700kHz, 150mm focal distance, a transcranial histotripsy array with transmit-receive capabilities, a neuronavigation system, and a transducer tracking instrument (TTI). The workflow for treatment delivery using NaviTH was developed. The feasibility and targeting accuracy of the system were evaluated using two excised human skulls and two, <96 hours post-mortem whole-body human cadavers, respectively. The overall system targeting error was divided into target registration error (TRE) and focal shift by skull aberration. TRE was due to errors associated with neuronavigation-to-Kranion (N2K) transformation and transducer tracking instrument (TTI), and the focal shift was due to skull aberration. NaviTH on cadavers produced an overall targeting error of 9 mm, 3.4 mm, and 4.4 mm on the corpus callosum, septum, and thalamus, respectively. This large targeting inaccuracy was found to be due to the design of the old TTI and the imperfect initial workflow, which caused a large TRE. An improvement was made in the TRE by altering the design of TTI.

Pre- and post-calibration TRE by ex vivo skulls were 8.27 and 1.89mm, respectively. The resulting focal shift arising from AC and skull aberration was 0.27mm. The post-calibration system targeting accuracy was evaluated by RBC phantoms and the resulting accuracy was 2.5 mm. Due to limited cadaver availability, post-calibration NaviTH was not tested on additional cadaveric models. This study demonstrated the first treatment of cadaveric models with transcranial histotripsy.

The final chapter summarizes the findings of this dissertation and discusses future work needed to bring transcranial histotripsy closer to the clinic.

Chapter 1 Introduction

This dissertation is focused on the investigation and development of high-intensity focused cavitational ultrasound surgery (histotripsy) as a non-invasive tool for transcranial ultrasound ablation. The technical emphasis of this dissertation is on the development and evaluation of accurate preoperative image-guided transcranial histotripsy targeting systems with a clinical emphasis on brain tumor treatment. The clinical emphasis is on the brain tumor, but transcranial histotripsy surgery has the potential to treat other neurological conditions such as intracranial hemorrhage, hydrocephalus, and Parkinson's disease. This dissertation is presented in five main parts: Chapter 1 introduces pre-operative image guidance in neurosurgery, brain tumors, the current standard of care, investigative ablation modalities, the mechanism of transcranial histotripsy, and the potential of transcranial histotripsy as a neurosurgical interventional tool; Chapter 2 discusses the development of a stereotactic transcranial histotripsy targeting system for *in vivo* murine brain models; Chapter 3 investigates the magnetic resonance imaging (MRI) analysis and characterization of *in vivo* features of transcranial histotripsy ablations in murine models; Chapter 4 discusses the first-pass investigation of the blood-brain barrier (BBB) status following transcranial histotripsy in *in vivo* mice brains, and Chapter 5 presents the development of a neuronavigation-guided transcranial histotripsy (NaviTH) system designed for human and tested using excised human skulls and human cadavers; 6) The final chapter concludes with future pre-clinical research for transcranial histotripsy.

This chapter first introduces pre-operative image guidance, malignant brain tumors, and current treatment options, followed by an overview of treatment methods under investigation. The underlying mechanism of the histotripsy technology is also introduced and its potential advantages for brain tumor treatment is discussed.

1.1 Preoperative Image Guidance in Neurosurgery

Preoperative image-guided surgery in neurosurgery uses high-resolution medical images of the brain such as computed tomography (CT) or magnetic resonance imaging (MRI) to guide an accurate surgery [1]. Image-guidance by preoperative images provide 3D location of the surgical tools relative to the medical images of the patient's brain during an operation. Especially for the brain where a small surgical mistake could mount to large functional loss in the patient, the accuracy of the operation is critical [2].

Typically, CT and MRI are obtained before the operation to noninvasively identify the potential presence of abnormal brain tissue such as a brain tumor, and imaging findings are confirmed with a minimally invasive biopsy. These same images can be used to accurately guide surgeries to remove the tumor and this process has provided surgeons with interactive image guidance, increased the accuracy of the surgery, and alleviated the symptoms of many patients [3-4]. An example of image-guided surgery workflow is as follows: 1) the patient's diagnostic or pre-operational image is obtained; 2) the patient's head is immobilized with a skull clamp; 3) the medical images of the patient and surgical instruments are co-registered via a neuronavigation system; 4) after the biopsy confirms a tumor, the neurosurgeon operates on the patient to resect the whole tumor while avoiding critical structures to minimize collateral damage to surrounding healthy brain tissues [4]. The neuronavigation system has been a critical guidance tool in the operating room and uses an optical tracking camera to co-register the patient, the medical images,

and the surgical instruments all in one virtual space to provide 3D locations of surgical instruments respective to the brain tissues. Image guidance by pre-operative images has been widely adopted in the clinic for any type of noninvasive or invasive surgery and allows clinicians to operate with high accuracy even without intraoperative or real-time imaging guidance, minimize collateral damage to surrounding healthy tissues, and provide flexibility in working in the operating room [5].

1.2 Brain Tumors

Brain tumors refer to any tissues that grow uncontrollably in the brain. Brain tumors, if not managed, can affect the healthy brain cells nearby. Depending on the location of the tumor within the brain, the patient can experience critical functional loss (ex: speech loss, memory loss, motor function loss, etc) [6]. This functional loss can often lead to decreased quality of life for the patient, and for some patients with severe symptoms, the patients experience seizure which can lead to the brain function failure and to eventual death.

In the US, 700,000 people are living with brain tumors [6]. Depending on the origin of the tumor, they are categorized into primary (originating from inside the brain) and secondary (originating from outside the brain) tumors. Primary tumors can be further categorized into benign or malignant tumors, while all secondary tumors are malignant. Regardless of the source, malignant brain tumors show an abysmal five-year survival rate of 33% despite extensive interventional efforts and technological advances [7]. More than half of malignant brain tumors are diagnosed in the cortex region with the highest percentage developing near the frontal lobe (26%) [6]. Often, the location of the tumor (i.e. shallow or deep region of the brain) dictates the operability and the potential complication rates (i.e. healthy tissue damage, bleeding,

inflammation, etc) associated with the surgery, with the complication rates and the difficulty in operability increasing with the depth of the brain.

Glioblastoma multiforme (GBM) is the deadliest and most prevalent malignant brain tumor with an abysmal five-year survival rate of 5% [6]. GBM, whose diameter averages about 5cm upon diagnosis, grows rapidly, increasing intracranial pressure and compromising the function of the brain region it grows and takes the lives of the patients [8]. Due to the diffusive nature of GBM, even after gross total resection, GBM cells can still be found in areas far away from the primary resection zone and will recur (~90%) to take the lives of the patients [9]. Despite the combined-modality approach of resection followed by radiation and chemotherapy, the median survival of glioblastoma patients is only 13 months [10]. The current invasive multi-modal approach only alleviates symptoms temporarily and does not bring significant survival benefits to the patients [11].

1.3 Clinical Treatment Options

For patients with malignant brain tumors, the current standard of care includes craniotomy to provide a surgical window for the tools, and total resection of the tumor, followed by radiation, and chemotherapy [10]. Craniotomy surgery requires creating an initial burr hole in the skull and proceeding to cut a larger window for access to minimally invasive tools. Through this created window into the brain, the neurosurgeon carefully investigates the brain tissue to avoid damaging functional brain tissues and to resect the tumor tissue. Nevertheless, this resection of the brain tumors requires damaging the healthy cells along the path to the target, increasing mortality and complication rates. For deep brain tumors located near the hypothalamus, the surgical option is often avoided due to the increased risks, and only radiation is applied in order to control the mass effect and the overwhelming growth of the tumor.

After resection, stereotactic radiation surgery (SRS), whole-brain radiation therapy (WBRT), and chemotherapy (ex: temozolomide and bevacizumab) are followed to kill any remnant tumor that the surgeon could not extract [12] and prevent further replication of the tumor cells. This combination therapy leads to many side effects including nausea, collateral damage to surrounding healthy brain tissues, and radiation necrosis leading to low quality of life [13]. In addition, chemotherapy debilitates the rest of the body where there are rapidly dividing cells, and the chemical agents have a difficult time passing through the blood-brain barrier (BBB) which serves as a critical barrier between the brain and the rest of the body [14-15]. Despite aggressive efforts to control the tumor and lengthen patient survival, the median survival of malignant brain tumor patients has not improved significantly over the past decades. A surgical option that is less invasive and applicable to both deep and shallow regions of the brain can decrease the mortality and complication rate, increase patient survival, and improve the quality of life of patients burdened with malignant brain tumors.

1.4 Treatment Options under Investigation

Numerous efforts have been made to decrease the invasiveness of brain tumor treatment and diversify therapy options. These options are nanoparticles [16-18] (to bypass the BBB and to better target the tumors), epigenetics [19-20] (to understand and better characterize the malignant tumors), immunotherapy [21-22] (to heighten the immune response against the tumors), and other ablative modalities under investigation. For the scope of this dissertation, the discussion will be limited to the ablative modalities under investigation.

Laser interstitial thermal therapy (LITT) is a minimally invasive laser ablative technology designed to thermally coagulate tissue with a high-intensity laser [23]. LITT guides the laser through fiber optic cable into the brain tissue and exposes malignant tissue to the laser, elevating

the temperature of the tissue, and causing thermal necrosis [24]. LITT is performed in the MRI scanner to visualize the heat increase in the ablation zone via MR thermometry [25]. MR-guidance is required for LITT due to risks associated with high heat laser. Risks include tissue absorption of laser at different wavelengths and potential charring and carbonization of the surrounding tissue that deter proper diffusion of heat [26-27]. Despite the advanced technology and its ability to access deep-seated brain tumors, LITT has shown limited success in clinical adoption because of the little efficacy against brain tumors, and it is mainly used as a secondary option for treating recurring brain metastases and radiation necrosis after the initial failure of radiation therapy [28]. LITT has been demonstrated as a safe and minimally invasive surgical option for brain tumors but the efficacy against tumors still remains unclear, and LITT still remains invasive due to the craniotomy needed to feed the fiber optic cable into the brain [29-30].

Magnetic resonance-guided focused ultrasound (MRgFUS) is a non-invasive thermally ablative ultrasound technology that can heat malignant brain tissues [31]. MRgFUS often applies continuous wave (CW) or high duty cycle ultrasound from outside the skull to heat tissue, which results in a temperature rise in the focal region [32-33]. MRgFUS thermal ablation has been used clinically to treat Essential Tremor [34], and Parkinson's [35]. MRgFUS has also been used to open the BBB for drug delivery to treat various brain diseases, including brain tumors [36] and Alzheimer's disease [37]. However, due to overheating of the skull caused by the CW ultrasound energy, the treatment locations are limited to the deep structures in the brain (<2cm from the skull) while over half of the malignant brain tumors are found in the shallow structures of the brain (i.e. cerebral cortex). Even with deep-seated tumors, there have been clinical trial cases where MRgFUS could not achieve the desired temperature (>55^{o}C) at the focal spot to achieve a therapeutic effect against brain tumors due to either skull heating or transducer technology

limitations [38]. Additionally, a long time is required to achieve small focal spot heating and therefore therapeutic effects by thermal coagulation of the tissue. An example clinical trial case achieved 0.7cm^3 volume ablation with a 4-hour treatment session [38], where the patient's glioma volume observed in the MRI was ten times (6.5cm^3) the volume ablated.

Both LITT and MRgFUS use real-time MR guidance to localize the focal spot of the treatment for accurate thermal dose delivery. However, with MR guidance, there have been cases where the localization of the focal spot was not achieved when there were blood products near the tumor from a prior biopsy [38]. In addition, the limited availability of MR scanners, the special equipment needed for MR compatibility, the slow treatment rate, and patient discomfort due to long hours in the MR scanner hinder its potential widespread clinical use [31].

1.5 Histotripsy

Histotripsy is a non-invasive focused ultrasound surgical technique that mechanically fractionates tissues using cavitation [39-40]. Histotripsy delivers microsecond ultrasound pulses from outside the body to the target, and when the rarefactional pressure exceeds a threshold intrinsic to the tissue (26-28MPa in water-based tissue) in the focal region, the existing nano gas nuclei in the tissue are excited [41]. This excitation leads to the gas nuclei in the focus growing to hundreds of micron-sized bubbles and together they form what is called a bubble cloud. The violent expansion and collapse of the bubble cloud mechanically stress and strain the tissues nearby, bisecting the cells apart [42].

Transcranial histotripsy uses ultrasound pulses delivered from outside the skull and focused inside the brain and has shown promise as a non-invasive neurosurgical tool. Transcranial histotripsy uses microseconds-long ultrasound pulses to avoid overheating of the skull [43], and the therapy can be monitored without MR guidance due to the histotripsy array's ability to localize

cavitation clouds generated in the skull during treatment [44]. Transcranial histotripsy has demonstrated its capabilities as a tumor debulking tool by ablating both deep and shallow regions (~5mm from the skull) within *ex vivo* human skulls [45] and has also successfully ablated large volumes of clots (ranging from 6-59mL) with the clinically relevant ablation rate of 4mL/min through different human skulls, all without raising the skullcap temperature ($\Delta T>4^0C$) [46]. In addition, transcranial histotripsy has demonstrated *in vivo* safety through numerous volumetric ablations of the normal brain in various animals [47-49] and has shown immunogenic effects on glioma-bearing murine models [49].

1.6 Transcranial Histotripsy for the Treatment of Brain Tumors

Transcranial histotripsy avoids craniotomy and any collateral damage associated with invasive surgery, delivers fast treatment, stimulates the immune system, and avoids radiation that impacts surrounding tissues. While ablative modalities such as MRgFUS and LITT require real-time MR guidance, rendering the operation costly, transcranial histotripsy could deliver highly accurate treatment with pre-treatment image guidance and cavitation real-time guidance all with a clinical workflow amenable to the current clinical standards for neurosurgery.

Thus, it is hypothesized that the development of initial models for image-guided stereotactic transcranial histotripsy platform will allow pre-clinical studies that bring a crucial understanding of histotripsy on brain tumors. In this dissertation, neuronavigation-guided transcranial histotripsy is developed and fully characterized to produce submillimeter accuracy for precise targeting of the malignant murine brain tissues in murine models. This low-cost, highly accurate stereotactic system is also used to develop an understanding of radiological and histological characteristics of post-transcranial histotripsy in *in vivo* mice with and without glioma

tumors. Additionally, the impact of transcranial histotripsy on BBB opening (BBBO) is evaluated in in vivo murine models by using Gd-contrast MR and BBB tight junction protein staining.

Finally, a neuronavigation-guided transcranial histotripsy workflow is developed and evaluated using excised human skulls and human cadavers. A neuronavigation system is utilized to co-localize the histotripsy transducer and the cadavers, and the accuracy of the setup is analyzed and improved to understand the system.

1.7 Transcranial Histotripsy and Other Indications

In this dissertation, transcranial histotripsy is introduced as a surgical modality for brain tumors, but its noninvasive ablation capabilities can be translated to ablation for the treatment of other brain indications such as intracranial hemorrhage (ICH), hydrocephalus, and other neurological disorders. Transcranial histotripsy application for ICH has been explored [43,46]. For obstructive hydrocephalus, transcranial histotripsy can create a channel through the septum pellucidum to restore communication between the ventricles.

1.8 Outline of This Dissertation

As mentioned previously, this book is divided into six chapters. The first chapter introduced preoperative image guidance, brain tumors, current treatment options, and the role of transcranial histotripsy in the treatment of brain tumors.

The second chapter discusses in detail the development of a focused ultrasound stereotactic platform for *in vivo* transcranial histotripsy of murine brains. The stereotactic platform consisted of a mouse fixture frame, treatment bed, and histotripsy transducer. An 8-element, 1 MHz histotripsy transducer with a focal distance of 32.5mm was used for this study. Each sub-component of the stereotactic system was analyzed for sources of error contributing to the targeting

uncertainty. The entire system was calibrated using red blood cell (RBC) clot phantoms. The targeting accuracy of the system was demonstrated with an in vivo mouse glioblastoma (GBM) model. The accuracy was quantified by the absolute distance difference between the prescribed and ablated points visible on the pre-treatment and post-treatment MR images, respectively. A pre-calibration phantom study (N = 6) resulted in an error of 0.32 ± 0.31, 0.72 ± 0.16, and 1.06 ± 0.38 mm in axial, lateral, and elevational axes, respectively. A post-calibration phantom study (N = 8) demonstrated a residual error of 0.09 ± 0.01, 0.15 ± 0.09, and 0.47 ± 0.18 mm in axial, lateral, and elevational axes, respectively. The calibrated system showed significantly reduced error of 0.20 ± 0.21, 0.34 ± 0.24, and 0.28 ± 0.21 mm in axial, lateral, and elevational axes, respectively, in the in vivo GBM tumor-bearing mice (N = 10).

The third chapter investigates the transcranial histotripsy MRI and histological findings in both normal mice without brain tumors and mice with brain tumors and evaluates the changes over time. An 8-element, 1 MHz histotripsy transducer with a focal distance of 32.5mm was used to treat normal mice and orthotopic GL261 tumor-bearing mice. The tumor burden at the time of treatment was ~3-5mm^3. T2, T2*, T1, and T1-gadolinium (Gd) MR images and H&E histology were acquired on days 0, 2, and 7 for tumor-bearing mice and days 0, 2, 7, 14, 21, and 28 for normal mice. Three mice were used for each time point and the MR images and H&E slides were interpreted by a neuroradiologist and a neuropathologist. T2 best showed anatomical feature changes due to the treatment, T2* the histotripsy ablation, T1 the blood product evolution from oxygenated blood to hemosiderin, and T1-Gd the BBBO that arises from a tumor or histotripsy ablation. These results provide a library of radiological features related to histology and will help better monitor animals in future histotripsy *in vivo* experiments.

The fourth chapter investigates the BBBO induced by transcranial histotripsy for the first time and studies how BBB at the periphery of the histotripsy ablation zone changes over time post-histotripsy with MRI and tight junction protein (TJP) staining. An 8-element, 1 MHz histotripsy transducer with a focal distance of 32.5mm was used to treat 15 BL6 female healthy mice. T1-gadolinium (Gd) MR images, H&E histology, and TJP-stained (Claudin-5 and Zonula Occludens-1 (ZO-1)) slides of the brain were acquired on days 0, 7, 14, 21, and 28 post-histotripsy (N= 3 at each time point). Analysis of T1-Gd MRI showed that the hyperintense BBBO area was increased for the first 7 days and subsided gradually over time. The area in the center of the histotripsy ablation, showed complete loss of the ZO-1 and claudin-5 immunostaining immediately post histotripsy, while at the border of the ablation, partial recovery of TJ complex was observed on day 7 post-histotripsy, and near-complete recovery of TJ complex was observed on day 21. These results provide the first evidence of transcranial histotripsy-induced BBBO.

The fifth chapter discusses the development of the first neuronavigation-guided transcranial histotripsy (NaviTH) system guided by preoperative images. The NaviTH system consists of a 360-element 700kHz, 150mm focal distance, a transcranial histotripsy array with transmit-receive capabilities, a neuronavigation system, and a transducer tracking instrument (TTI). The workflow for treatment delivery using NaviTH was developed. The feasibility and targeting accuracy of the system were evaluated using two excised human skulls and two, <96 hours post-mortem whole-body human cadavers, respectively. The overall system targeting error was divided into target registration error (TRE) and focal shift by skull aberration. TRE was due to errors associated with neuronavigation-to-Kranion (N2K) transformation and transducer tracking instrument (TTI), and the focal shift was due to the skull aberration. NaviTH on cadavers produced an overall targeting error of 9 mm, 3.4 mm, and 4.4 mm on the corpus callosum, septum,

and thalamus, respectively. This large targeting inaccuracy was found to be due to the design of old TTI and the imperfect initial workflow, which caused a large TRE. An improvement was made in the TRE by altering the design of TTI. Pre- and post-calibration TRE by ex vivo skulls were 8.27 and 1.89mm, respectively. The resulting focal shift arising from AC and skull aberration was 0.27mm. The post-calibration system targeting accuracy, which is the summation of uncertainty from TRE and skull shift, was 1.90mm. Due to limited cadaver availability, post-calibration NaviTH was not tested on additional cadaveric models.

The final chapter summarizes the findings of this dissertation and discusses future work needed to bring transcranial histotripsy closer to the clinic.

1.9 References

[1] K. Cleary and T. M. Peters, "Image-guided interventions: Technology review and clinical applications," *Annu. Rev. Biomed. Eng.*, vol. 12, pp. 119–142, 2010, doi: 10.1146/annurev-bioeng-070909-105249.

[2] U. Spetzger *et al.*, "Error analysis in cranial neuronavigation," *Minim. Invasive Neurosurg.*, vol. 45, no. 1, pp. 6–10, 2002, doi: 10.1055/s-2002-23583.

[3] J. B. West and C. R. Maurer, "Designing optically tracked instruments for image-guided surgery," *IEEE Trans. Med. Imaging*, vol. 23, no. 5, pp. 533–545, 2004, doi: 10.1109/TMI.2004.825614.

[4] A. Khoshnevisan and N. S. Allahabadi, "Neuronavigation: Principles, clinical applications and potential pitfalls," *Iran. J. Psychiatry*, vol. 7, no. 2, pp. 97–103, 2012.

[5] S. Dhawan, Y. He, J. Bartek, A. A. Alattar, and C. C. Chen, "Comparison of Frame-Based Versus Frameless Intracranial Stereotactic Biopsy: Systematic Review and Meta-Analysis," *World Neurosurg.*, vol. 127, pp. 607-616.e4, 2019, doi: 10.1016/j.wneu.2019.04.016.

[6] Q. T. Ostrom, N. Patil, G. Cioffi, K. Waite, C. Kruchko, and J. S. Barnholtz-Sloan, "CBTRUS statistical report: Primary brain and other central nervous system tumors diagnosed in the United States in 2013-2017," *Neuro. Oncol.*, vol. 22, no. Supplement_1, pp. IV1–IV96, 2020, doi: 10.1093/neuonc/noaa200.

[7] National Brain Tumor Society (NBTS). Quick Brain Tumor Facts (NBTS, 2018).

[8] K. Urbanska, J. Sokolowska, M. Szmidt, and P. Sysa, “Glioblastoma multiforme - An overview,” *Wspolczesna Onkol.*, vol. 18, no. 5, pp. 307–312, 2014, doi: 10.5114/wo.2014.40559.

[9] M. Weller, T. Cloughesy, J. R. Perry, and W. Wick, “Standards of care for treatment of recurrent glioblastoma-are we there yet?,” *Neuro. Oncol.*, vol. 15, no. 1, pp. 4–27, 2013, doi: 10.1093/neuonc/nos273.

[10] S. Lapointe, A. Perry, and N. A. Butowski, “Primary brain tumours in adults,” *Lancet*, vol. 392, no. 10145, pp. 432–446, 2018, doi: 10.1016/S0140-6736(18)30990-5.

[11] G. Minniti *et al.*, “Radiotherapy plus concomitant and adjuvant temozolomide for glioblastoma in elderly patients,” *J. Neurooncol.*, vol. 88, no. 1, pp. 97–103, 2008, doi: 10.1007/s11060-008-9538-0.

[12] O. P. Erpoat, M. Akmansu, F. Gokse, H. Bora, E. Yaman, and S. Buyukberber, “Outcome of newly diagnosed glioblastoma patients treated by radiotherapy plus concomitant and adjuvant temozolomide: A long-term analysis,” *Tumori*, vol. 95, no. 2, pp. 191–197, 2009, doi: 10.1177/030089160909500210.

[13] A. H. Palejwala *et al.*, “Laser Interstitial Thermal Therapy for Metastatic Melanoma After Failed Radiation Therapy: A Case Series,” *Oper. Neurosurg.*, vol. 19, no. 2, pp. 9–11, 2020, doi: 10.1093/ons/opaa012.

[14] C. D. Arvanitis, G. B. Ferraro, and R. K. Jain, “The blood–brain barrier and blood–tumour barrier in brain tumours and metastases,” *Nat. Rev. Cancer*, vol. 20, no. 1, pp. 26–41, 2020, doi: 10.1038/s41568-019-0205-x.

[15] N. J. Abbott, A. A. K. Patabendige, D. E. M. Dolman, S. R. Yusof, and D. J. Begley, “Structure and function of the blood-brain barrier,” *Neurobiol. Dis.*, vol. 37, no. 1, pp. 13–25, 2010, doi: 10.1016/j.nbd.2009.07.030.

[16] W. Tang, W. Fan, J. Lau, L. Deng, Z. Shen, and X. Chen, “Emerging blood-brain-barrier-crossing nanotechnology for brain cancer theranostics,” *Chem. Soc. Rev.*, vol. 48, no. 11, pp. 2967–3014, 2019, doi: 10.1039/c8cs00805a.

[17] M. Yang, J. Li, P. Gu, and X. Fan, “The application of nanoparticles in cancer immunotherapy: Targeting tumor microenvironment,” *Bioact. Mater.*, vol. 6, no. 7, pp. 1973–1987, 2021, doi: 10.1016/j.bioactmat.2020.12.010.

[18] N. Shah *et al.*, “Investigational chemotherapy and novel pharmacokinetic mechanisms for the treatment of breast cancer brain metastases,” *Pharmacol. Res.*, vol. 132, pp. 47–68, 2018, doi: 10.1016/j.phrs.2018.03.021.

[19] O. Gusyatiner and M. E. Hegi, “Glioma epigenetics: From subclassification to novel treatment options,” *Semin. Cancer Biol.*, vol. 51, no. October 2017, pp. 50–58, 2018, doi: 10.1016/j.semcancer.2017.11.010.

[20] L. Abballe and E. Miele, “Epigenetic modulators for brain cancer stem cells: Implications for anticancer treatment,” *World J. Stem Cells*, vol. 13, no. 7, pp. 670–684, 2021, doi: 10.4252/wjsc.v13.i7.670.

[21] S. S. Wang, P. Bandopadhayay, and M. R. Jenkins, “Towards Immunotherapy for Pediatric Brain Tumors,” *Trends Immunol.*, vol. 40, no. 8, pp. 748–761, 2019, doi: 10.1016/j.it.2019.05.009.

[22] J. H. Sampson, M. D. Gunn, P. E. Fecci, and D. M. Ashley, “Brain immunology and immunotherapy in brain tumours,” *Nat. Rev. Cancer*, vol. 20, no. 1, pp. 12–25, 2020, doi: 10.1038/s41568-019-0224-7.

[23] M. Bettag *et al.*, “Stereotactic laser therapy in cerebral gliomas.,” *Acta Neurochir. Suppl. (Wien).*, vol. 52, pp. 81–83, 1991, doi: 10.1007/978-3-7091-9160-6_23.

[24] M. A. Leonardi and C. B. Lumenta, “Stereotactic guided laser-induced interstitial thermotherapy (SLITT) in gliomas with intraoperative morphologic monitoring in an open MR: Clinical expierence,” *Minim. Invasive Neurosurg.*, vol. 45, no. 4, pp. 201–207, 2002, doi: 10.1055/s-2002-36203.

[25] J. De Poorter, “Noninvasive MRI thermometry with the proton resonance frequency method: Study of susceptibility effects,” *Magn. Reson. Med.*, vol. 34, no. 3, pp. 359–367, 1995, doi: 10.1002/mrm.1910340313.

[26] S. G. Bown, “Phototherapy of Tumors,” *World J. Surg.*, vol. 7, no. 6, pp. 700–709, 1983.

[27] K. G. Holste and D. A. Orringer, “Laser interstitial thermal therapy,” *Neuro-Oncology Adv.*, vol. 2, no. 1, 2020, doi: 10.1093/noajnl/vdz035.

[28] C. Chen, I. Lee, C. Tatsui, T. Elder, and A. E. Sloan, “Laser interstitial thermotherapy (LITT) for the treatment of tumors of the brain and spine: a brief review,” *J. Neurooncol.*, vol. 151, no. 3, pp. 429–442, 2021, doi: 10.1007/s11060-020-03652-z.

[29] J. Torres-Reveron, H. C. Tomasiewicz, A. Shetty, N. M. Amankulor, and V. L. Chiang, “Stereotactic laser induced thermotherapy (LITT): A novel treatment for brain lesions regrowing after radiosurgery,” *J. Neurooncol.*, vol. 113, no. 3, pp. 495–503, Jul. 2013, doi: 10.1007/s11060-013-1142-2.

[30] C. Hoppe, J. A. Witt, C. Helmstaedter, T. Gasser, H. Vatter, and C. E. Elger, “Laser interstitial thermotherapy (LiTT) in epilepsy surgery,” *Seizure*, vol. 48. W.B. Saunders Ltd, pp. 45–52, May 01, 2017, doi: 10.1016/j.seizure.2017.04.002.

[31] Z. Izadifar, Z. Izadifar, D. Chapman, and P. Babyn, “An Introduction to High Intensity Focused Ultrasound: Systematic Review on Principles, Devices, and Clinical Applications,” *J. Clin. Med.*, vol. 9, no. 2, p. 460, Feb. 2020, doi: 10.3390/jcm9020460.

[32] F. Marquet *et al.*, “Non-invasive ultrasonic surgery of the brain in non-human primates,” *J. Acoust. Soc. Am.*, vol. 134, no. 2, pp. 1632–1639, 2013, doi: 10.1121/1.4812888.

[33] D. Weintraub and W. J. Elias, “The emerging role of transcranial magnetic resonance imaging–guided focused ultrasound in functional neurosurgery,” *Mov. Disord.*, vol. 32, no. 1, pp. 20–27, 2017, doi: 10.1002/mds.26599.

[34] N. Lipsman *et al.*, “MR-guided focused ultrasound thalamotomy for essential tremor: A proof-of-concept study,” *Lancet Neurol.*, vol. 12, no. 5, pp. 462–468, 2013, doi: 10.1016/S1474-4422(13)70048-6.

[35] N. Y. Jung, C. K. Park, M. Kim, P. H. Lee, Y. H. Sohn, and J. W. Chang, “The efficacy and limits of magnetic resonance–guided focused ultrasound pallidotomy for Parkinson’s disease: A Phase I clinical trial,” *J. Neurosurg.*, vol. 1306, no. 6, pp. 1853–1861, 2019, doi: 10.3171/2018.2.JNS172514.

[36] T. Mainprize *et al.*, “Blood-Brain Barrier Opening in Primary Brain Tumors with Non-invasive MR-Guided Focused Ultrasound: A Clinical Safety and Feasibility Study,” *Sci. Rep.*, vol. 9, no. 1, pp. 1–7, Dec. 2019, doi: 10.1038/s41598-018-36340-0.

[37] N. Lipsman *et al.*, “Blood-brain barrier opening in Alzheimer’s disease using MR-guided focused ultrasound,” *Nat. Commun.*, vol. 9, no. 2336, 2018, doi: 10.1038/s41467-018-04529-6.

[38] D. Coluccia *et al.*, “First noninvasive thermal ablation of a brain tumor with MR-guided focused ultrasound,” *J. Ther. Ultrasound*, vol. 2, no. 1, pp. 1–7, 2014, doi: 10.1186/2050-5736-2-17.

[39] Z. Xu *et al.*, “Controlled ultrasound tissue erosion.,” *IEEE Trans. Ultrason. Ferroelectr. Freq. Control*, vol. 51, no. 6, pp. 726–736, 2004, doi: 10.1109/TUFFC.2004.1304271.

[40] J. E. Parsons, C. A. Cain, G. D. Abrams, and J. B. Fowlkes, “Pulsed cavitational ultrasound therapy for controlled tissue homogenization,” *Ultrasound Med. Biol.*, 2006, doi: 10.1016/j.ultrasmedbio.2005.09.005.

[41] A. D. Maxwell, C. A. Cain, T. L. Hall, J. B. Fowlkes, and Z. Xu, “Probability of Cavitation for Single Ultrasound Pulses Applied to Tissues and Tissue-Mimicking Materials,” *Ultrasound Med. Biol.*, vol. 39, no. 3, pp. 449–465, 2013, doi: 10.1016/j.ultrasmedbio.2012.09.004.

[42] E. Vlaisavljevich, A. Maxwell, L. Mancia, E. Johnsen, C. Cain, and Z. Xu, "Visualizing the Histotripsy Process: Bubble Cloud–Cancer Cell Interactions in a Tissue-Mimicking Environment," *Ultrasound Med. Biol.*, vol. 42, no. 10, pp. 2466–2477, Oct. 2016, doi: 10.1016/J.ULTRASMEDBIO.2016.05.018.

[43] T. Gerhardson, J. R. Sukovich, A. S. Pandey, T. L. Hall, C. A. Cain, and Z. Xu, "Effect of Frequency and Focal Spacing on Transcranial Histotripsy Clot Liquefaction, Using Electronic Focal Steering," *Ultrasound Med. Biol.*, vol. 43, no. 10, pp. 2302–2317, 2017, doi: 10.1016/j.ultrasmedbio.2017.06.010.

[44] J. R. Sukovich, J. J. MacOskey, J. E. Lundt, T. I. Gerhardson, T. L. Hall, and Z. Xu, "Real-Time Transcranial Histotripsy Treatment Localization and Mapping Using Acoustic Cavitation Emission Feedback," *IEEE Trans. Ultrason. Ferroelectr. Freq. Control*, vol. 67, no. 6, pp. 1178–1191, 2020, doi: 10.1109/TUFFC.2020.2967586.

[45] J. R. Sukovich *et al.*, "Targeted Lesion Generation Through the Skull Without Aberration Correction Using Histotripsy," *IEEE Trans. Ultrason. Ferroelectr. Freq. Control*, vol. 63, no. 5, pp. 671–682, 2016, doi: 10.1109/TUFFC.2016.2531504.

[46] T. Gerhardson *et al.*, "Histotripsy Clot Liquefaction in a Porcine Intracerebral Hemorrhage Model," *Clin. Neurosurg.*, vol. 86, no. 3, pp. 429–436, 2020, doi: 10.1093/neuros/nyz089.

[47] N. Lu *et al.*, "Transcranial MR-guided Histotripsy System," *IEEE Trans. Ultrason. Ferroelectr. Freq. Control*, vol. 68, no. 9, pp. 2917–2929, 2021, doi: 10.1109/TUFFC.2021.3068113.

[48] S. W. Choi *et al.*, "Stereotactic Transcranial Focused Ultrasound Targeting System for Murine Brain Models," *IEEE Trans. Ultrason. Ferroelectr. Freq. Control*, vol. 68, no. 1, pp. 154–163, 2021, doi: 10.1109/TUFFC.2020.3012303.

[49] T. Gerhardson, "Transcranial Therapy for Intracerebral Hemorrhage and Other Brain Pathologies using Histotripsy," Dissertation, 2020.

Chapter 2 Stereotactic Transcranial Focused Ultrasound Targeting System for Murine Brain Models

This chapter has been published *in IEEE Transactions on Ultrasonics, Ferroelectrics, and Frequency Control*. 2021; 68(1) 154-163.

2.1 Introduction

An essential component of success for non-invasive procedures such as focused ultrasound (FUS) is accurate targeting. The focus of an ultrasound transducer needs to be precisely placed on the target tissue (e.g., tumor) inside the body to avoid damage to surrounding healthy tissues [20]. For focused ultrasound brain procedures, a small mistargeting of the ultrasound focus can lead to damage to nearby normal tissues including critical structures followed by life-long complications [2]. In this paper, an accurate and inexpensive transcranial FUS stereotactic targeting method guided by pre-treatment magnetic resonance imaging (MRI) was developed specifically for rodent brain models, and its accuracy was evaluated in a murine glioblastoma model.

Stereotactic approaches have been widely adopted clinically to achieve high accuracy targeting in minimally and non-invasive procedures [3-11]. Stereotactic guidance refers to an approach that immobilizes the anatomic part of interest in a frame equipped with fixed fiducials, and uses pre-procedural images, associated three dimensional coordinates, and fiducial locations to accurately locate and target tissue deep inside the body [3].

Transcranial FUS delivers ultrasound from outside the skull and focuses into the target brain tissue to induce desired bioeffects. There has been rapidly increasing interest in studying transcranial FUS for treatment of various neurological diseases [12-16]. Transcranial MRI guided FUS (tcMRgFUS) has been approved by the FDA for treatment of essential tremor, and there are

clinical trials ongoing for the treatment of brain tumors, Parkinson's disease, and Alzheimer's disease [17-18]. The FUS modalities under investigation include thermal FUS [20,26], mechanical FUS (termed histotripsy) [21-23], blood-brain barrier opening using low amplitude ultrasound and contrast agent injection [24-25,44], and FUS neuromodulation [19,45].

Murine brain models have been an essential animal model for preclinical FUS brain research [25,39-41]. For the mouse brain, accurate targeting is critical because the mouse brain is small (~10 x 17 x 8mm^3) compared to the ultrasound focal volume (~1 x 1 x 3mm^3). A targeting error greater than 1mm can lead to damage to surrounding critical brain structures. For example, an inaccurate targeting on a tumor near a ventricle that damages it can lead to severe complications for a mouse [40].

Real-time MRI guidance is an essential tool for transcranial FUS targeting and monitoring. MRI provides volumetric images with high resolution and high tissue-tumor contrast [28-32]. MRI thermometry can be used to visualize ultrasound focal points and monitor tissue damage in real-time. Real-time MRI guidance has been successfully used to guide and monitor focused ultrasound treatment of the brain (e.g., tcMRgFUS) [14]. However, a real-time MR-guided FUS system for mice can be difficult to achieve in some research facilities due to the high cost associated with MR-compatible equipment (MR-compatible driving electronics, positioner, etc.) and high technical barriers that require extensive MR expertise [47].

In this paper, we describe in detail a low-cost stereotactic transcranial FUS mouse system guided by pre-treatment MRI scans and quantitatively measure its accuracy in phantoms and a well-established *in vivo* murine glioblastoma (GBM) GL261 model. This stereotactic approach exploits the high soft-tissue contrast advantages of pre-procedural MRI to achieve high accuracy without the requirement of an MR-compatible FUS system and extensive MR expertise. The FUS

system presented here was tested for transcranial histotripsy in the murine GBM model but can be easily adapted to be used with other transcranial rodent models and modalities, such as transcranial thermal FUS, FUS BBB opening, and FUS neuromodulation. We hope and believe that this stereotactic FUS brain system will enable more researchers to join the rapidly growing and prospective field of FUS brain research.

2.2 Materials and Methods

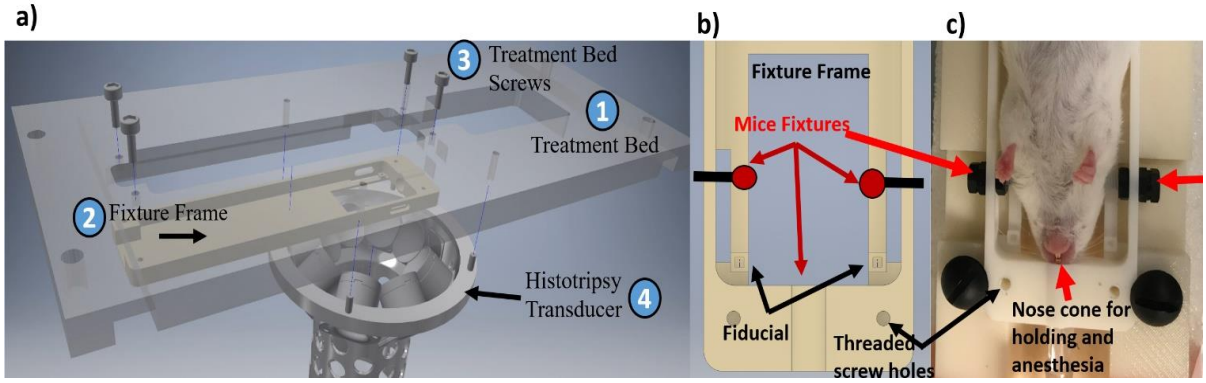

Figure 2.1.Mouse fixture frame and the stereotactic setup. a) shows the stereotactic setup and the sequence used for co-registration. The fixture frame (2) is screwed (3) into the treatment bed (1), and pins of histotripsy transducer (4) are inserted into the treatment bed for completion of co-registration. CAD design of the fixture frame is shown on panel **b)**. Panel **c)** shows a photograph of the frame holding a mouse head with ear bars.

First, a stereotactic FUS murine system was designed, fabricated, and described in ***A. Stereotactic FUS Setup***. Second, the associated workflow was presented in ***B. Stereotactic FUS Workflow***. We characterized the error for each sub-component of the system in ***C. Sub-component Error Analysis.*** Next, the localization error for the entire system was evaluated in ***D. System Error Analysis*** via clot phantom and *in vivo* (glioma bearing mice) experiments.

2.2.1 Stereotactic FUS Setup

Key hardware components of the stereotactic FUS setup consisted of the mouse fixture frame, treatment bed, and histotripsy transducer (Fig. 2.1a). The 3D-printed fixture frame contained two fiducial markers, mouse fixture ear bars, a nose cone, and threaded screw holes (Fig. 2.1b). The plastic print material was MR-compatible and allowed imaging of the animal in the MRI scanner before the treatment. The ear bars were placed to fix the skull of the mouse with a force sufficient for skull immobilization but not excessive so as to avoid appreciable discomfort. These ear bars were held in place by nylon nuts. The nose cone provided oxygen and isoflurane for inhalational anesthesia and held the nose immobile. The nose cone and the ear bars ensured that the mouse brain was held in a fixed position and orientation for the entire period from pre-treatment imaging to post-treatment MRI scans. The fiducial markers acted as fixed reference points from which the target tissue could be localized. Threaded screw holes on the fixture frame (shown in Fig. 2.1b & 2.1c) aided in co-registering the treatment bed and frame.

The stereotactic setup CAD schematic is shown in Fig. 2.1a. The treatment bed (1) contained a slot for the mouse fixture frame (2). After imaging the mouse in the frame, the frame was placed in the treatment bed, aligned via the threaded holes, and screwed (3) to the treatment bed. To co-register the transducer with the treatment bed, four alignment pins attached to the lip of the histotripsy transducer (4) were inserted in matching pinholes of the treatment bed. This attachment process ensured that the exact location of the fiducial markers and histotripsy transducer focus was known with respect to the treatment bed and thus the location of the target relative to the focus.

Other stereotactic setup hardware included a 3-axis positioner, water tank, and positioner-transducer connection illustrated in Fig. 2.2a. The 3-axis motor positioner was used to move the histotripsy transducer to the ablation target.

2.2.2 Stereotactic FUS Workflow

Here we explain a step-by-step workflow associated with stereotactic FUS procedures for an *in vivo* treatment in a glioma mouse model, which contains five steps. 1) The head of the mouse was fixed within the fixture frame (Fig. 2.1c). 2) Pre-treatment MRI images were acquired using a 7T small animal MRI scanner (Varian, Inc., Palo Alto, CA, USA), and a T2-weighted fast spin-echo (T2w FSE) sequence (Table 2.1) was used to achieve contrast between brain tissue and the tumor. 3) After imaging, the animal was transferred in an induction box (5.25L Induction Chamber, Midmark Corp. Versailles, OH, USA) filled with oxygen and isoflurane from the MRI scanner to the histotripsy procedure room. In the FUS procedure room, components were co-registered (Fig. 2.1a), and targeting was planned by identifying fiducial markers and tumor locations with a MATLAB GUI (Mathworks Inc., Natick, MA, USA) (Fig. 2.3). The animal was held by the fixture frame during the entire process. 4) Histotripsy was delivered with set parameters. 5) Post treatment, the mouse brain was scanned, and the post-treatment scan was compared with the pre-treatment scan to evaluate the targeting accuracy of the system (Fig. 2.4).

A radiofrequency (RF) volume coil positioner was fabricated to hold the mouse fixture frame and ensure repeatable placement of the mouse in the main magnetic field. This consistent placement in the MRI scanner allowed treatment planning and analysis of prescriptions and post-treatment lesions easier.

Table 2.1. 7T MRI IMAGING PARAMETERS

Imaging Object	Clot Phantom	GBM Mouse
TR (ms)	2000	4000
ESP (ms)	10	15
Kzero	1	4 (TE = 60ms)
ETL	8	8
Slice thickness (mm)	0.5	0.5
Data Matrix	128 x 128	128 x 128
FOV (mm^2)	30 x 30	30 x 30
Pixel Size (mm)	0.23	0.23
# of averages	4	4
Scanning Time (minutes)	~4.5	~9

TR = Time to Repetition, ESP = echo spacing, ETL = echo train length, FOV = field of view.

2.2.3 Sub-component Error Analysis

All the hardware components and procedures related to stereotactic FUS described above contribute to registration error of the entire system due to imperfections (e.g., manufacturing tolerances, motor positioner imprecision, mouse motion). We analyzed individual components and procedures for uncertainties to investigate the sources of inaccuracy with this system. We assumed these errors are random, independent, and each has a normal distribution with a mean of 0 and a standard deviation estimated by experiments or calculations. The total standard deviation, σ_{total}, is obtained as follows:

$$\sigma_{total} = sqrt[\sigma_H^2 + \sigma_{MO}^2 + \sigma_W^2 + \sigma_{PTC}^2 + \sigma_{MRI}^2 + \sigma_{TP}^2 + \sigma_A^2]$$

where H stands for key hardware, MO for motorized 3-axis positioner, W for water tank, PTC for positioner-transducer connection, MRI for MRI images, TP for treatment planning process, and A for aberration due to the ultrasound propagation through the mouse skull and brain tissue.

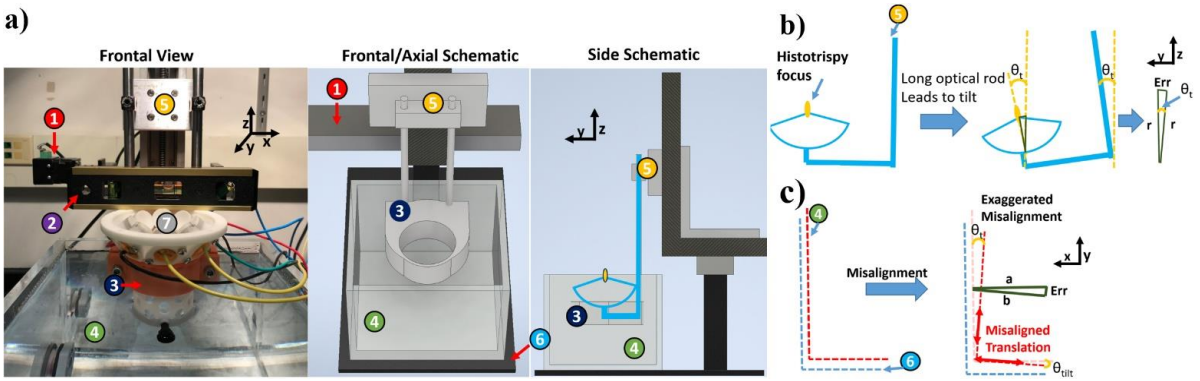

Figure 2.2.Axial and frontal setup of the stereotactic FUS setup and the associated components. Major components of the stereotactic setup are ultrasound transducer, treatment bed, and fixture frame. Minor components of the stereotactic setup include a water tank, a transducer holder and a 3-axis positioner **(a)**. All components were adjusted to minimize angular registration errors. **b)** & **c)** illustrate ways these associated components (motor positioner to transducer connection and water tank misalignment) can contribute to imperfect co-registration of the stereotactic setup. An optical rod that is connected to the motor holds both the transducer holder and the histotripsy transducer. The longer the optical rod hangs down, the larger the tilt, as illustrated in **(b)**. In addition, the motor stage, on which the motor is mounted to, needs to align with the water tank **(c)**. Any source of misalignment causes misdirected translation by the motor system. These errors can be calculated by the cosine law. Labels: 1) motorized 3-axis positioner, 2) spirit level, 3) transducer holder, 4) water tank, 5) Positioner to transducer connector, 6) motor stage, 7) Histotripsy transducer.

i. Hardware Uncertainty Analysis

Key system components—Co-registration uncertainties associated with the manufacturing of key system components (i.e. frame, treatment bed, and transducer) were derived from the tolerances from design and fabrication resolution provided by the manufacturer.

Other hardware components included the 3-axis positioner, water tank, and positioner-transducer connection (Fig. 2.2a).

Motorized 3-axis positioner—The motorized 3-axis positioner (stepper motor: 17MDSI102S, Anaheim Automation, Anaheim, CA, USA) (linear motion system: MS33-100218, Thomson Linear Motor System, Radford, VA, USA) precision was critical to the experiment since the transducer was mechanically steered by the positioner. The listed manufacturer precision for the linear motion system was 5 μm and the stepper motor step size resolution was 0.225°. However, because the motor and positioner slides were purchased separately, a three-step experiment was devised to characterize the motorized positioner.

A commercial disposable hemocytometer (C-Chip DHC-F01, Chungnam-do, Republic of Korea) was used as a geometry reference. A 100 μm fiber (F-MLD-C-5FC, Newport Corporation, Irvine, CA, USA) was attached to the positioner, placed directly in front of the hemocytometer, and moved in fixed amounts to measure the repeatability of the positioner. The distances traveled were extracted from preliminary phantom studies and averaged 15mm in vector length. The three steps were as follows: 1) the fiber started in the middle of the hemocytometer, 2) traveled 15mm to a point away from the hemocytometer, and 3) was steered back to the middle of the hemocytometer. Images were captured with a camera (PointGrey, FLIR Systems Inc., Wilsonville, OR, USA) pre- and post-travel to determine how close the fiber returned to its original position. Each measurement was taken ten times to study the precision. This setup was repeated to evaluate all three axes of the motor positioning system. Each image pixel was 2.7μm in size and the edge spread function (ESF, 10%-90%) resolution was 16 μm. In addition, we noticed a vibration in the room. This vibration was imaged by capturing the stationary fiber 60 times with a 20Hz frame rate. 20 Hz was the maximum frame rate achievable by the video capture system.

Water tank—The water tank needed to be aligned with the lateral and elevational motion (xy-axis) of the 3-axis positioner (Fig. 2.2c). Its relationship to the positioner is illustrated (Fig.

2.2a). The frontal/axial schematic provides the location of the water tank (labeled 4 in Fig. 2.2a) respective to the motor stage (labeled 6 in Fig. 2.2a). The 3-axis positioner was screwed onto the motor stage, and the portable water tank and its parallel alignment to the motor stage ensured consistent translation of the transducer with respect to the treatment bed, which lay on and aligned with the water tank. If the water tank was not aligned with the 3-axis positioner, this led to tilted translation which was exacerbated with longer travel (Fig. 2.2c). This relationship was estimated by the cosine law given below:

$$Err^2 = a^2 + b^2 - 2(ab)\cos(\theta_{tilt})$$

where *Err* is the travel error in the transverse plane caused by the misalignment between the water tank and the motor stage, θ_{tilt} is the tilt between the water tank and the motor stage, a is the mistranslated coordinate caused by θ_{tilt}, and b is the true-translation coordinate when in perfect alignment.

Positioner-transducer connection—The positioner-transducer connection uncertainty is illustrated in Fig. 2.2b. The positioner is connected to the transducer by long optical rods (Thorlabs, Newton, NJ, USA). The long motor optical rods that connect the transducer holder and transducer were tilted due to the length of the rods and the inconsistent holding point. The transducer and the transducer holder were detached for different experiments on the workstation and putting it back on and off introduced uncertainties. This tilt was measured using a spirit level and protractor.

ii. Procedural and Aberration Uncertainty Analysis

As mentioned previously in the workflow subsection, imaging the animal with MRI, transporting the animal from the MRI coil to the surgery room, and treatment planning were part of the workflow. Another source of error apparent in all *in vivo* ultrasound experiments was aberration due to the ultrasound propagation through the mouse skull and brain tissue. These

procedures and components are briefly explained except for transporting errors due to an inability to adequately quantify. Transporting is briefly explained in the *Results & Discussion*.

MRI—Treatments were planned based on MRI images of the mouse brain. In doing so we needed to account for small image distortions associated with calibration of imaging gradient coils. We performed calibration measurements of our apparatus, using samples with known geometry and location. Additionally, for each experiment we used fiducial markers integrated into the fixture frame (Fig. 2.3). Both calibration experiments and measured fiducial marker locations in our images gave consistent results, indicating that our MR images (acquired at the iso-center of the magnet) appeared dilated by 106% parallel to the B0 field and 104% orthogonal to the B0 field. Fundamentally, this means that the applied field gradient pulse strength in the imaging experiments exceeds the nominal pulse strength by those respective amounts, at the iso-center of the MRI system.

We corrected for this simple distortion by rescaling with a constant multiplicative factor based on the fiducial marker positions for each experiment. The multiplicative factor was calculated by dividing the distance between the fiducial markers measured by MRI divided by that measured by a caliper. Multiple clot phantom experiments were conducted, and the constant multiplicative factors calculated from n=6 experiments were averaged to derive the constant multiplicative factor to be used in the post-calibration phantom and *in vivo* mouse experiments. A simple dilation approximation applied to all three gradient directions was thought to be sufficient because the volume of interest (a sphere of diameter 10mm around iso-center) was much smaller than the volume of the gradient set (120mm transverse x 80mm longitudinal).

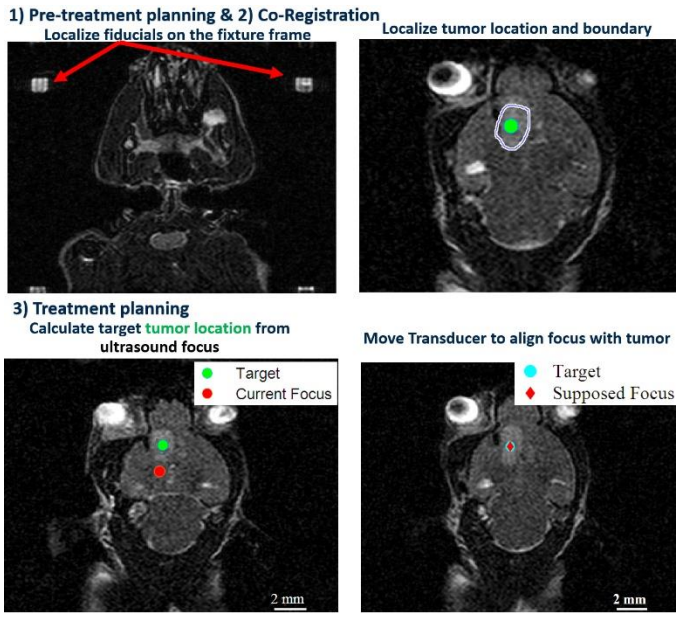

Figure 2.3. Treatment planning procedure for murine stereotactic FUS. Fiducial markers (1) and tumor (2) are localized. Center of the tumor is prescribed as an ablation point (3) and the transducer is steered towards the target point before initiating FUS.

Treatment planning software—The treatment planning software built from MATLAB required hand-drawing of the fiducial markers and tumors (Fig 2.3). Such method of hand-drawing/selecting features is widely practiced in the clinic by radiologists. For this study, a single author (S.W. Choi) repeated the hand-drawing process 20 times on the same image set, and the intra-observer error was calculated. This resulted in 20 different motor travel coordinates and these values produced a mean and a standard deviation. We considered the standard deviation from this to be the uncertainty associated with treatment planning.

Aberration—Finally, we considered the case for aberration due to the ultrasound propagation through the skull and brain, which can result in a shift of the focus of the histotripsy transducer. Even in cases of small animals, the ultrasound path may change due to the speed of sound difference and angle of incidence (refraction) caused by the various tissues along the beam. For example, the speed of sound in the skull (~2.3mm/us) [38] is known to be substantially different from the speed of sound in water (~1.49mm/us). The mice skull averages about 245μm

in thickness and the thickness varies from 100μm to 650μm [43]. In addition to the ultrasound arriving at the skull interface differently, the amount of soft tissue (speed of sound = ~1.54mm/us) [34] that the ultrasound beam encountered, however small (2-6mm), affects the arrival time of sound at the focus. If the tumor were located on the right ventricle and assuming symmetric geometry of the mouse head, an ultrasound pulse from one side of the transducer would travel through approximately 6mm of tissue and a pulse from the contralateral side only 2-3mm.

2.2.4 System Error Analysis

For all experiments, a 1MHz, 8-element ultrasound transducer delivered histotripsy pulses and each element produced a 1.5-cycle sinusoid. Each animal or phantom was treated with 100 pulses at 1 Hz pulse repetition frequency (PRF), creating a single ablation zone. The acoustic parameters were chosen to ensure accuracy of the ablation by avoiding cavitation memory effect [42]. The estimated peak negative pressure in a free field was 32 MPa based on pressure measurements from fiber optic hydrophone, and this set of parameters created an ellipsoid lesion of 1mm in the minor axis and 3mm in the major axis on clot phantoms. The 3-axis positioner mechanically moved the histotripsy transducer to target the centroid of the prescribed volume.

To determine a single point target to conduct accuracy testing of the setup for both clot phantoms and tumor-bearing mice, 3D volume representations of the tumors were created using a series of 2D tumor masks. The centroid of the tumor volume was prescribed as a point target, and pre- and post-treatment images were compared to analyze the differences between prescription and resultant ablation points. To quantify the accuracy of the system, internal brain structures were used as co-registration features to calculate the discrepancy between the prescribed point and centroids of the histotripsy ablations (Fig. 2.4). The accuracy was calculated by obtaining the absolute difference between prescription and ablation centroids.

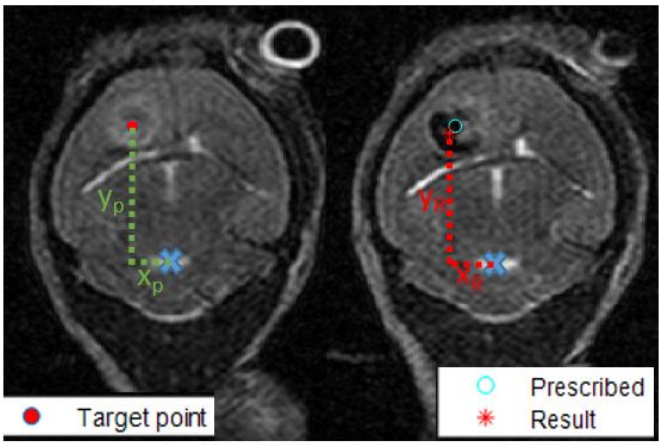

Figure 2.4.Calculating the targeting error. From the center of a fixed internal brain structure marked in x, the distance to the prescribed region and the distance to the centroid of the histotripsy lesion are compared to determine the targeting inaccuracy.

2.2.5 Clot Phantom Experiments

In this model, agarose gel (AG-SP, LabScientific Inc., Highlands, NJ, USA) represented brain tissue and clot represented the tumor target. Fresh bovine blood was acquired from a local abattoir (Dunbar Meat Packing Co., Milan, MI, USA) and refrigerated up to a week with citrate phosphate dextrose (CPD) (Boston Bioproducts, Boston, MA, USA) with a CPD-to-blood ratio of 1:10. Bovine blood clots and clot phantom have been widely used in preclinical studies [23,35,42].

The clot phantom was created by warming the blood to 38^{o} C, and mixing calcium chloride (Honeywell 21114 Fluka, Charlotte, NC, USA) in a 20:1 (blood:CaCl) ratio before embedding the mixture onto a 1.5 % agarose gel. The clot phantom was imaged in the fixture frame, treated, and re-imaged. Because the clot has a shorter T2 relaxation time than agarose gel, blood appeared dark and agar bright on T2-weighted MR images (Fig. 2.5b). When treated by histotripsy, the clots experienced a conformational change that lengthened the T2 time [35]. This ablated zone appeared bright on T2-weighted images, and the images were used to analyze where the histotripsy ablation zone was formed within the clot phantoms. The phantoms were used to evaluate any system error associated with calibration.

2.2.6 In Vivo Mice Glioblastoma (GBM) Experiments

GL261-Luciferase positive cells (Perkin-Elmer, Walktham, MA, USA) were cultured and $1x10^5$ cells were stereotactically injected into B6 Albino female mice (Charles River, Wilmington, MA, USA) in 1 µl of serum-free Dulbecco's Modified Eagle Medium (DMEM) media [36]. Mice were fixed in the prone position. A 2cm incision was made at the midline of the skull along the sagittal suture. Using an electric burr drill, a burr hole was placed 1mm posterior to the coronal suture, and 2.5-3mm to the right of the sagittal suture. and the cells were injected 2mm deep into the burr hole, placing the tumor adjacent to lateral corpus collosum and the lateral ventricle. Tumor growth was confirmed using bioluminescence imaging and tumor volume was monitored using both bioluminescence imaging and T2-weighted fast spin-echo MRI. Histotripsy was applied to the tumors when they reached 5-15mm^3 in volume. To determine the tumor volume, the tumor boundaries were outlined on each 2D MR image. The delineated area was calculated from each slice, multiplied by the slice thickness of the MR image, and then summed over all slices to calculate the tumor volume.

On the day of histotripsy treatment, inhalation of isoflurane (1.5-2.0%) in 1 L/min of oxygen (SurgiVet V704001, Smiths Medical, Waukesha, WI, USA) were used to induce and maintain general anesthesia of the mice. All animals were injected with Carprofen (Rimadyl, Pfizer, NY, USA) analgesic (5mg/kg) subcutaneously prior to histotripsy treatment and once every 24 hours for 2 days after histotripsy procedure. The mouse hair was clipped, and chemical depilation was performed (Nair, Church & Dwight Co., Ewing Township, NJ, USA) to ensure no trapped air bubbles could block acoustic access.

The temperature of the mice during MR image acquisition was maintained at 36-37^{o}C using an MR-compatible fiber optic temperature module and MR-compatible heater system for small animals, which are controlled by the 1025T Monitoring and Gating System (SA instruments, Stony Brook, NY, USA). The mouse temperature, breathing rate, isoflurane level and oxygen level were recorded in 15 minutes interval. During histotripsy treatment, the transducer was submerged in a degassed water tank and the water temperature was maintained 36-38^{o}C using a coil heater. A rectal temperature probe (item #: 50304 Stoelting Co, Wood Dale, IL, USA) was also used to check and sustain the temperature of the mice during the histotripsy treatment.

Ten GBM tumor-bearing mice were treated with the stereotactic FUS setup after calibrating the system accuracy with the clot phantoms as described above. The protocol described in this manuscript and all mouse procedures have been approved by the University of Michigan Institutional Animal Care and Use Committee (IACUC).

2.3 Results & Discussion

2.3.1 Sub-component Error

Uncertainties of individual system components were measured or estimated as described in *Methods*. The values are summarized in Table 2.2 and are explained in the following subsections.

i. Hardware Uncertainties

Key system components—The tolerances from the design and fabrication resolution provided by the manufacturer (SLA Normal Resolution, Protolabs, Maple Plain, MN, USA) were 0.254mm and 0.10mm, respectively. Assuming a normal distribution of errors with these values of standard deviations yields an estimated combined uncertainty of 0.27mm ($= \sqrt{0.254^2 + 0.10^2}$).

Motorized 3-axis positioner—Images of the fiber were captured and analyzed. Comparing the ESF center points of the pre- and post-travel, the maximum shift was equivalent to 8.1μm. The vibration in the room captured by the camera was also 8.1μm. As a result, we calculated the standard deviation of 9.1μm ($= \sqrt{(8.1)^2+(8.1/2)^2}$) associated with the positioning system.

Table 2.2. Sources of errors, individual estimates and total estimate

Sources of error	**Estimate Distribution (mm)**
Hardware (H)	*N(*0,0.27)
Motorized Positioner (MO)	*N(*0,0.0091)
Water Tank Misalignment (W)	*N(*0,0.13)
Positioner-Transducer Connection (PTC)	*N(*0,0.57)
MRI Geometric Inaccuracy (MRI)	*N(*0,0.75)
Treatment Planning Software (TP)	*N(*0,0.12)
Aberration (A)	*N(*0,0.13)
Total Uncertainty	*N(*0,1.00)

Water tank—Regarding the water tank position relative to the positioner, we assumed the uncertainty associated was 0.5-degrees, as no tilt visible to the naked eyes was observed. 0.5-degree tilt angle was sufficiently small and not detectable by eyes. This uncertainty can produce 0.13mm of mistranslation in the transverse plane (XY) for a positioner movement of 15mm.

Positioner-transducer connection—An average of 1 degree of tilt was recorded, which can result up to 0.57mm shift in the focus of the transducer in the ZY direction (Fig. 2.2b).

ii. Procedural and Aberration Uncertainty

MRI—15mm of average travel was assumed and 105% average gradient-induced image dilation to produce 0.75mm of uncertainty.

Treatment planning software—The calculated intra-observer standard deviation of the 20 treatment planning procedures was 0.12mm.

Aberration—We considered the maximum aberration uncertainty related to the skull (i.e. 100μm of skull encountered by one element and 650μm by the contralateral element). In this case, the acoustic wave from the minimum thickness side will exit the skull and encounter soft tissue 0.12μs faster than the maximum thickness side. This will amount to the sound from the thinner side arriving at the focus 0.18mm earlier than the thicker side. For brain tissue and for a tumor near a lateral ventricle, considering the unique ultrasound path to reach these tumors, we assumed the standard deviation of aberration related to brain tissue to be 0.13mm in the GBM mice. The total uncertainty estimated by aberration due to skull and brain tissue combined amounts to 0.22mm ($= \sqrt{(0.18)^2+(0.13)^2}$).

Transport of the mouse from the MR scan room to the FUS procedure room was a component of the workflow. The transport involved walking the stereotactic frame about 200 feet,

a flight of stairs and six doors. The frame was designed to hold the animal as rigidly as possible, ensuring positional consistency between pre- and intra-operative images. This workflow produced some vibration on the animal due to walking, and a finite skin shift was expected. However with our setup and comparing pre- and post-treatment images, we have not observed any noticeable shifts of skin and brain (image resolution 0.23mm). Hence we treated this variable as an unknown.

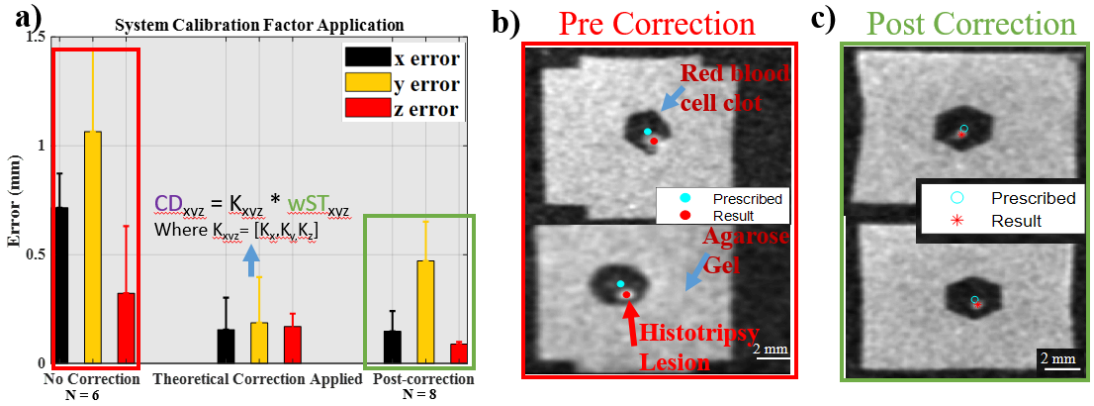

Figure 2.5. Stereotactic FUS system calibration through a linear correction factor. Without correction ("No Correction"), the difference between prescribed point to ablation point, i.e., error, was >1 millimeter. After understanding that a system bias exists and a constant multiplicative factor can be applied to reduce the targeting error ("*Theoretical Correction Applied*"), another batch of clot phantom experiments showed reduced error to submillimeter ("*Post-correction*"). On **a)**, CD stands for correct distance, K for constant multiplicative factor, and wST for wrong steering distance originally calculated that did not account for the system bias.

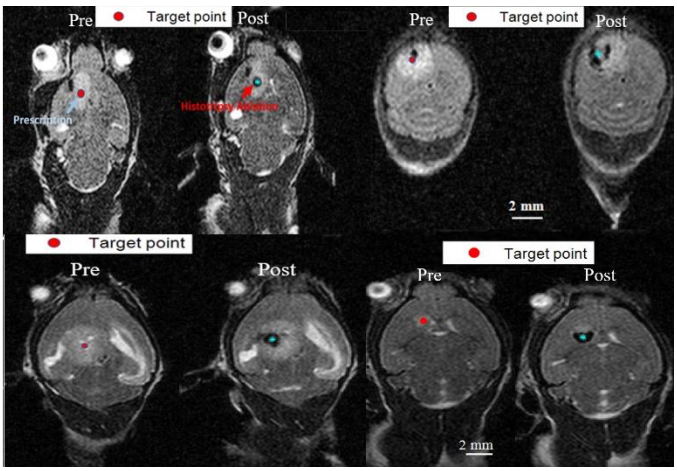

Figure 2.6. Histotripsy ablation of multiple tumor-bearing mice. T2 weighted pre-treatment image shows GBM tumor (left) with red dots as prescribed ablation points. The ablated region appears dark (thought to be coagulated blood) on the post-treatment image (right) indicated by the blue dot. The tumor appears in the left brain in the images because the mice are lying supine when imaged.

2.3.2 System Error

Without system calibration, the inaccuracy produced from initial clot phantom (N=6) experiments was 0.32 ± 0.31, 0.72 ± 0.16, and 1.06 ± 0.38mm in axial, lateral and elevational axes, respectively, which result in a total error of 1.4mm ("*No correction*" in Fig. 2.5a & 2.5b). After applying the multiplicative factor from the system calibration, another set of clot phantom experiments (N=8) yielded a targeting error of 0.09 ± 0.01, 0.15 ± 0.09, and 0.47 ± 0.18mm in axial, lateral and elevational axes, respectively ("*Post-correction*" in Fig. 2.5a & 2.5c) and a total error of 0.50 mm. The errors here refer to the absolute difference between prescription and resultant ablation zone centroids.

The calibrated stereotactic system was tested on *in vivo* GBM mice. In all 10 *in vivo* mice tested, a single point ablation was successfully produced within the tumor (Fig. 2.6). By comparing pre- and post-treatment MRI scans, the targeting accuracy was measured to be 0.20 ± 0.21, 0.34 ± 0.24, and 0.28 ± 0.21mm in axial, lateral, and elevational axes, respectively, which add to a total error of 0.48mm.

Sub-millimeter accuracy was achievable after applying a constant multiplicative factor from the system calibration. Of all the error sources, the primary contributor that was compensated by the multiplicative factor was MRI field gradient-induced error. The constant multiplicative factor improved the accuracy (~1.4mm to ~0.5mm), and the amount of accuracy improved (~0.9mm improvement) was similar to the amount of total uncertainty estimated (~1mm). The remaining inaccuracy also implies that there are unidentified uncertainties that contributed to the

error of the stereotactic system and the system can be further improved. As mentioned previously, this submillimeter accuracy was necessary for the mouse model due to the small size of the brain and the tumor.

2.3.3 Statistical Analysis of the Errors

1-way ANOVA tests were conducted to initially assess the difference between pre-calibration phantom, post-calibration phantom and *in vivo* mice experiments. Three ANOVA tests were conducted for each dimension (i.e. lateral, elevational, and axial). ANOVA tests for lateral and elevational dimension showed statistically significant differences ($p = 3.6x10^{-5}$, $p = 2.7x10^{-5}$, respectively), but ANOVA on axial axis failed to reject the null hypothesis ($p = 0.25$).

Because ANOVA tests showed significant differences in lateral and elevational axes, subsequent t-tests were conducted to further analyze the differences among the lateral and elevational axes. The tests showed significant differences in the accuracies of post- vs. pre-calibration clot phantom experiments in both lateral and elevational axes ($p<0.05$). The accuracies in the *in vivo* GBM mouse experiment were significantly better compared to the pre-calibration clot phantom in lateral and elevational axes ($p=3.6x10^{-7}$, $p=6.6x10^{-4}$, respectively), but were worse compared to the post-calibration clot experiments ($p=0.02$, $p= 0.04$, respectively).

T-tests showed significant differences ($p<0.05$) between post-calibration clot experiments and *in vivo* mice. It is thought that these differences were caused by the added uncertainties introduced by a live subject (i.e. mouse) instead of a gel phantom, on which the system calibration was performed.

2.3.4 Potential improvements

The current system can be modified to further improve targeting accuracy. First, the overall number of hardware components in the system can be reduced to decrease component-associated uncertainties. Each component contributes small amounts of variability to the system, and this can be resolved by building an integrated design. For example, the positioner-transducer connection was composed of five parts: positioner attachment plate, optical posts, optical rods, transducer holder, and histotripsy transducer. Each part introduces uncertainty of its own and combining some of these parts can help reduce component-associated variability.

Another improvement can come from acquiring computed tomography (CT) images to fuse with MRI to reduce geometric distortion of images. CT images are known to be geometrically accurate, and the fusion of CT and MRI is widely used in the clinic [37]. Usually, both pre-treatment CT and MRI are obtained prior to stereotactic localizations, so the image geometric inaccuracy experienced in this small animal system will not be a large source of error when geometrically calibrated MRI is used or MRI images are fused with CT images. Finally, the current system uncertainty can be reduced further by decreasing the transport distance from the MRI scanner to the procedure room.

2.3.5 Adopting stereotactic FUS setup

To set up for other FUS applications such as BBB opening and neuromodulation, a rigid treatment bed that holds a rodent fixture frame and connects the FUS transducer needs to be designed similarly as shown in Fig. 2.1a. Co-registration features need to be added to the FUS transducer to inform the location of the ultrasound focus when connected to the treatment bed, and the fixture frame containing MR-visible fiducials will hold the mouse during pre- and post-treatment MRI and the FUS treatment.

Of note, while we did not perform tail vein injection of microbubbles in this study, this stereotactic setup support two possible modes of access if needed. First, prior to placing the mouse in the fixture frame, the tail vein can be cannulated and secured, and the mouse subsequently fixed in the frame. Alternatively, an IV can be placed after the animal is already fixed in the frame as the tail is not encapsulated by the hardware.

We have explored a step-by-step process of analyzing individual components of a highly accurate stereotactic FUS system for rodent brain models. The proof-of-concept of the stereotactic FUS brain setup has been demonstrated, and the targeting error was measured to be well below one millimeter (~0.5mm on both clot phantoms and in vivo tumor-bearing mice), comparable to the accuracy of real-time MR-guided rodent systems [46]. We believe this stereotactic system will provide an inexpensive and accurate alternative targeting approach for various applications of ultrasound research in rodent brain models. This stereotactic system described in this study was designed to be easily fabricated and does not require treatment inside an MRI scanner.

2.4 References

[1] S. W. Choi *et al.*, "Stereotactic Transcranial Focused Ultrasound Targeting System for Murine Brain Models," *IEEE Trans. Ultrason. Ferroelectr. Freq. Control*, vol. 68, no. 1, pp. 154–163, 2021, doi: 10.1109/TUFFC.2020.3012303.

[2] P. Ghanouni *et al.*, "Transcranial MRI-guided focused ultrasound: A review of the technologic and neurologic applications," *Am. J. Roentgenol.*, vol. 205, no. 1, pp. 150–159, 2015.

[3] M. Carter and J. Shieh, "Stereotaxic Surgeries and In Vivo Techniques," *Guid. to Res. Tech. Neurosci.*, no. Chapter 4, pp. 73–88, 2015.

[4] M. Safaee, J. Burke, and M. W. Mcdermott, "Techniques for the Application of Stereotactic Head Frames Based on a 25-Year Experience." *Cureus.*, vol. 8, no. 3. 2016.

[5] P. W. A. Willems, J. W. B. Van Der Sprenkel, C. A. F. Tulleken, M. A. Viergever, and M. J. B. Taphoorn, "Neuronavigation and surgery of intracerebral tumours," *J. Neurol.*, vol. 253, no. 9, pp. 1123–1136, 2006.

[6] S. B. Omay and G. H. Barnett, “Surgical navigation for meningioma surgery,” *J. Neurooncol.*, vol. 99, no. 3, pp. 357–364, 2010.

[7] B. Lippitz, C. Lindquist, I. Paddick, D. Peterson, K. O’Neill, and R. Beaney, “Stereotactic radiosurgery in the treatment of brain metastases: The current evidence,” *Cancer Treat. Rev.*, vol. 40, no. 1, pp. 48–59, 2014.

[8] R. B. Jimenez *et al.*, “The impact of different stereotactic radiation therapy regimens for brain metastases on local control and toxicity,” *Adv. Radiat. Oncol.*, vol. 2, no. 3, pp. 391–397, Jul. 2017.

[9] P. J. Kelly, S. J. Goerss, and B. A. Kall, “Evolution of contemporary instrumentation for computer-assisted stereotactic surgery,” *Surg. Neurol.*, vol. 30, no. 3, pp. 204–215, 1988.

[10] G. H.K., W. D.C., and L. C.B., “BrainLab VectorVision neuronavigation system: Technology and clinical experiences in 131 cases,” *Neurosurgery*, vol. 44, no. 1, pp. 97–105, 1999.

[11] L. Leksell, D. Leksell, and J. Schwebel, “Stereotaxis and nuclear magnetic resonance,” *J. Neurol. Neurosurg. Psychiatry*, vol. 48, no. 1, pp. 14–18, 1985.

[12] N. Lipsman *et al.*, “MR-guided focused ultrasound thalamotomy for essential tremor: A proof-of-concept study,” *Lancet Neurol.*, vol. 12, no. 5, pp. 462–468, 2013.

[13] C. T. Curley, N. D. Sheybani, T. N. Bullock, and R. J. Price, “Focused ultrasound immunotherapy for central nervous system pathologies: challenges and opportunities,” *Theranostics*, vol. 7, no. 15, pp. 3608-3623., 2017.

[14] Burgess *et al.*, “Alzheimer disease in a mouse model: Mr imaging-guided focused ultrasound targeted to the hippocampus opens the blood-brain barrier and improves pathologic abnormalities and behavior,” *Radiology*, vol. 273, no. 3, pp. 736–745, 2014.

[15] J. R. Sukovich, Z. Xu, Y. Kim, H. Cao, T.-S. Nguyen, A. S. Pandey, T. L. Hall, C. A. Cain, “Targeted lesion generation through the skull without aberration correction using histotripsy,” *IEEE Trans Ultrason Ferroelectr Freq Control*, vol. 63, no. 5, pp. 671-682, May 2016.

[16] L. da Costa, N. Lipsman, A. Bethune, T. Mainprize, and K. Hynynen, “MRIgFUS in the treatment of spontaneous intracerebral hemorrhage TL - 3,” *J. Ther. Ultrasound*, vol. 3 VN-re, no. S1, p. 1, 2015.

[17] N. Y. Jung, C. K. Park, M. Kim, P. H. Lee, Y. H. Sohn, and J. W. Chang, “The efficacy and limits of magnetic resonance–guided focused ultrasound pallidotomy for Parkinson’s disease: A Phase I clinical trial,” *J. Neurosurg.*, vol. 1306, no. 6, pp. 1853–1861, 2019.

[18] N. Lipsman *et al.*, “Blood-brain barrier opening in Alzheimer’s disease using MR-guided focused ultrasound,” *Nat. Commun.*, vol. 9, no. 2336, 2018.

[19] S. Kubanek, Jan, “Neuromodulation with transcranial focused ultrasound,” *Neurosurg. Focus*, vol.

44, no. 2, 2018.

[20] T. A. Leslie and J. E. Kennedy, “High-intensity focused ultrasound principles, current uses, and potential for the future,” *Ultrasound Q.*, vol. 22, no. 4, pp. 263–272, 2006.

[21] K. Lin, Y. Kim, A. D. Maxwell, T. Wang, T. L. Hall, Z. Xu, B. Fowlkes, C. A. Cain, “Histotripsy beyond the “intrinsic” threshold using very short ultrasound pulses: “microtripsy”,” *IEEE Trans Ultrason Ferroelectr Freq Control*, vol. 61, no. 2, pp. 251-265, Feb. 2014.

[22] K. B. Bader, E. Vlaisavljevich, and A. D. Maxwell, “For Whom the Bubble Grows: Physical Principles of Bubble Nucleation and Dynamics in Histotripsy Ultrasound Therapy,” *Ultrasound Med. Biol.*, vol. 45, no. 5, pp. 1056–1080, 2019.

[23] T. Gerhardson, J. R. Sukovich, A. S. Pandey, T. L. Hall, C. A. Cain, and Z. Xu, “Catheter Hydrophone Aberration Correction for Transcranial Histotripsy Treatment of Intracerebral Hemorrhage: Proof-of-Concept,” *IEEE Trans. Ultrason. Ferroelectr. Freq. Control*, vol. 64, no. 11, pp. 1684–1697, 2017.

[24] K. Hynynen, N. McDannold, N. A. Sheikov, F. A. Jolesz, and N. Vykhodtseva, “Local and reversible blood-brain barrier disruption by noninvasive focused ultrasound at frequencies suitable for trans-skull sonications,” *Neuroimage*, vol. 24, no. 1, pp. 12–20, 2005.

[25] K. C. Wei *et al.*, “Focused Ultrasound-Induced Blood-Brain Barrier Opening to Enhance Temozolomide Delivery for Glioblastoma Treatment: A Preclinical Study,” *PLoS One*, vol. 8, no. 3, pp. 1–10, 2013.

[26] D. Jeanmonod *et al.*, “Transcranial magnetic resonance imaging–guided focused ultrasound: noninvasive central lateral thalamotomy for chronic neuropathic pain,” *Neurosurg. Focus*, vol. 32, no. 1, p. E1, 2011.

[27] E. Martin, D. Jeanmonod, A. Morel, E. Zadicario, and B. Werner, “High-intensity focused ultrasound for noninvasive functional neurosurgery,” *Ann. Neurol.*, vol. 66, no. 6, pp. 858–861, 2009.

[28] Y. S. Kim *et al.*, “Volumetric MR-HIFU ablation of uterine fibroids: Role of treatment cell size in the improvement of energy efficiency,” *Eur. J. Radiol.*, vol. 81, no. 11, pp. 3652–3659, 2012.

[29] M. O. Köhler *et al.*, “Volumetric HIFU ablation guided by multiplane MRI thermometry,” in *AIP Conference Proceedings*, 2009.

[30] J. E. Kennedy *et al.*, “High-intensity focused ultrasound for the treatment of liver tumours,” *Ultrasonics*, vol. 42, no. 1–9, pp. 931–935, 2004.

[31] T. Uchida *et al.*, “Five years experience of transrectal high-intensity focused ultrasound using the Sonablate device in the treatment of localized prostate cancer,” *Int. J. Urol.*, 2006.

[32] . Shoji, “Magnetic resonance imaging-transrectal ultrasound fusion image-guided prostate biopsy:

Current status of the cancer detection and the prospects of tailor-made medicine of the prostate cancer," *Investig. Clin. Urol.*, 2019.

[33] F. Fry and J. E. Barger, "Acoustical properties of the human skull." *J. Acoust. Soc. Am.*, vol.63, no. 5, pp 1576- 1590, 1978.

[34] "Speed of Sound," *Speed of Sound " ITIS Foundation*. [Online]. Available: https://itis.swiss/virtual-population/tissue-properties/database/acoustic-properties/speed-of-sound/. [Accessed: 06-Dec-2019].

[35] S. P. Allen, "Magnetic Resonance Imaging Guidance for Histotripsy Therapy," Ph.D dissertation, Biomedical Medical Engineering, University of Michigan, Ann Arbor, MI, USA, 2016.

[36] B. C. Baumann, J. F. Dorsey, J. L. Benci, D. Y. Joh, and G. D. Kao, "Stereotactic intracranial implantation and in vivo bioluminescent imaging of tumor xenografts in a mouse model system of glioblastoma multiforme," *J. Vis. Exp.*, no. 67, Sep. 2012.

[37] K. I. Saima Altaf, "Brain Gliomas CT-MRI Image Fusion for Accurate Delineation of Gross Tumor Volume in Three Dimensional Conformal Radiation Therapy," *Omi. J. Radiol.*, vol. 04, no. 02, 2015.

[38] H. Estrada, J. Rebling, and D. Razansky, "Broadband acoustic properties of a murine skull," Phys. Med. Biol, vol. 61, p. 1932, 2016.

[39] E. Thévenot *et al.*, "Targeted delivery of self-complementary adeno-associated virus serotype 9 to the brain, using magnetic resonance imaging-guided focused ultrasound," *Hum. Gene Ther.*, vol. 23, no. 11, pp. 1144–1155, 2012.

[40] R. Chopra, L. Curiel, R. Staruch, L. Morrison, and K. Hynynen, "An MRI-compatible system for focused ultrasound experiments in small animal models," *Med. Phys.*, vol. 36, no. 5, pp. 1867–1874, 2009.

[41] S. B. Raymond, L. H. Treat, J. D. Dewey, N. J. McDannold, K. Hynynen, and B. J. Bacskai, "Ultrasound enhanced delivery of molecular imaging and therapeutic agents in Alzheimer's disease mouse models," *PLoS One*, vol. 3, no. 5, pp. 1–7, 2008.

[42] J. E. Lundt, S. P. Allen, J. Shi, T. L. Hall, C. A. Cain, and Z. Xu, "Noninvasive, Rapid Ablation of Tissue Volume Using Histotripsy." doi: 10.1016/j.ultrasmedbio.2017.08.006.

[43] L. Ghanbari *et al.*, "Craniobot: A computer numerical controlled robot for cranial microsurgeries," *Sci. Rep.*, vol. 9, no. 1, Dec. 2019.

[44] T. Ilovitsh *et al.*, "Enhanced microbubble contrast agent oscillation following 250 kHz insonation," *Sci. Rep.*, vol. 8, no. 16347, 2018.

[45] G. F. Li *et al.*, "Improved Anatomical Specificity of Non-invasive Neuro-stimulation by High Frequency (5 MHz) Ultrasound," *Sci. Rep.*, vol. 6, no. April, 2016.

[46] N. P. K. Ellens *et al.*, "The targeting accuracy of a preclinical MRI-guided focused ultrasound

system," vol. 42, no. 1, pp. 430–439, 2015.

[47] M. E. Poorman *et al.*, "Open-source, small-animal magnetic resonance-guided focused ultrasound system," *J. Ther. Ultrasound*, vol. 4, p. 22, 2016.

Chapter 3 Histotripsy Treatment of Murine Brain and Glioma: Temporal Profile of MRI and Histological Characteristics Post-treatment

This Chapter has been submitted as a full paper to Ultrasound in Medicine and Biology, and is under review.

3.1 Introduction

Craniotomy remains the mainstay diagnostic and therapeutic modality for the treatment of brain tumors [1-2]. Craniotomy requires an incision, penetration of normal tissues to reach oncological tissue, and manipulation of normal surrounding cerebral tissue when removing oncological tissue. In addition, tumors at the skull base or deep within the brain are not easily accessible to craniotomy-based approaches. To overcome these craniotomy-based shortcomings, minimally invasive and non-invasive techniques for brain tumors and lesions have been developed. These include radiation therapy [3-6], laser interstitial thermal therapy (LITT) [7-10], and transcranial magnetic resonance-guided focused ultrasound (tcMRgFUS) [11-14]. The use of radiation therapy is limited due to the safety limit of cumulative radiation dose, the radiosensitive nature of adjacent structures in the brain, and the radio-resistance of certain tumors [15]. LITT is a minimally invasive histotripsy method that uses a thin optical fiber inserted in the brain to create thermal necrosis; however, it requires penetration of cerebral tissue to reach the target. LITT has shown success for brain radiation necrosis but is limited by treatment shape and volume [16].

tcMRgFUS is a non-invasive therapy technology that can ablate deep brain structures with ultrasound. tcMRgFUS often uses continuous wave ultrasound energy applied from outside the

skull to heat tissue, which results in temperature rise in the focal region and thermal necrosis [14]. tcMRgFUS thermal ablation has been FDA approved to treat Essential Tremor [17] and Parkinson's disease with tremors [18]. However, due to overheating of the skull caused by the ultrasound, the treatable locations and volumes are highly limited. tcMRgFUS with very low-pressure ultrasound pulses combined with microbubbles can temporarily open the blood-brain barrier (BBB) thus allowing for drug delivery to the brain for various brain diseases, including brain tumors [19-20] and Alzheimer's disease [21].

In contrast to tcMRgFUS, histotripsy uses high-pressure, microsecond-length ultrasound pulses to mechanically fractionate the target tissues into acellular homogenates via cavitation [22-26]. The high strain and stress resulting from cavitation mechanically disrupt the cells in the target tissue. Histotripsy has been investigated to treat a wide range of cancers in preclinical studies and is in a clinical trial as a non-invasive treatment for liver cancer [27]**.** Transcranial histotripsy uses a very low duty cycle (<0.1%) to mitigate the heating of the skull (<4^{o}C) while maintaining effective cavitation [30]. Transcranial histotripsy has shown great promise by ablating wide ranges of cerebral locations inside the skull through *ex vivo* human skulls and in *in vivo* porcine experimental models [28-33].

Due to its non-invasive and non-ionizing nature, MRI is the clinical gold standard for the diagnosis of brain diseases and post-treatment changes. Different clinical MRI sequences visualize specific features of the brain tumor and the response of the therapy delivered. For example, both LITT and tcMRgFUS can be visualized with T2 sequences immediately after treatment with features including a central hypointense core and a thick hyperintense periphery [34]. T2* has been utilized to visualize any bleeding after such procedures. T1-gadolinium (Gd) coupled with

tcMRgFUS has been used to observe BBB opening allowing for drug delivery into the brain as well as regression or progression of brain tumor growth [20].

This paper aims to characterize the post-histotripsy MRI features of the murine brain with and without tumors. Because histotripsy fractionates tissue via a different physical mechanism than other non-invasive treatment modalities such as radiation, LITT, and tcMRgFUS thermal ablation, there is a need to understand the MRI characteristics of the brain with and without tumors post histotripsy treatment including the temporal profile of changes. We aim to address the following two goals. 1) To correlate MRI features with histology post-histotripsy treatment of normal and tumor-bearing mouse brain, including histotripsy zone boundary, histotripsy homogenate, and residual tumor. 2) To establish the natural evolution of histotripsy-treated murine brain tissue as characterized by MRI and histology. This library of images will be instrumental in identifying histotripsy-related features for future clinical transcranial histotripsy brain therapy.

3.2 Materials and Method

3.2.1 Tumor model

The murine glioma GL261 model was used. For tumor-bearing mice, GL-261 cells were cultured and were stereotactically injected into BL6 female mouse brains (Taconic Farms, Rensselaer, NY, USA) as described in [36]. The tumor cells were injected 1mm posterior to the coronal suture, 2.5mm to the right of the sagittal suture, and 2mm deep.

3.2.2 Animal Procedure

Tumor growth was monitored weekly via MRI, and transcranial histotripsy was delivered when tumor volume approached ~5mm^3, which corresponded to approximately 10-14 days post-

implantation. The workflow described in [36] was used, and after histotripsy treatment, both normal and tumor-bearing mice were monitored via MRI.

The timeline of the study is detailed in Figure 3.1. The study was planned so that transcranial histotripsy on both tumor-bearing and normal mice could be observed. Normal mice were survived up to day 28 post-histotripsy with six time points (Day 0, 2, 7, 14, 21, and 28) while the tumor-bearing mice survived up to day 7 post-histotripsy with three time points (Day 0, 2, and 7). Tumor-bearing mice survived for a shorter period because of the aggressive nature of the glioma cell line used and because this study did not aim to observe the survival benefit of histotripsy. A total of 8 groups and 3 mice per group were used.

For each time point, T2, T2*, T1, and T1-Gadolinium (ProHance 279.3mg/ml, Bracco, NJ, USA) images were obtained with a 7T small animal scanner (Varian Inc., Palo Alto, CA, USA) and changes in MRI histotripsy size were measured and recorded. The sequence parameters are listed in Table 3.1. 0.1ml gadolinium was administered via the intraperitoneal cavity and the T1 images were acquired 10 minutes after administration. At the end of the time point, the mice were euthanized from CO_2 overdose and their brains were extracted for H&E histology.

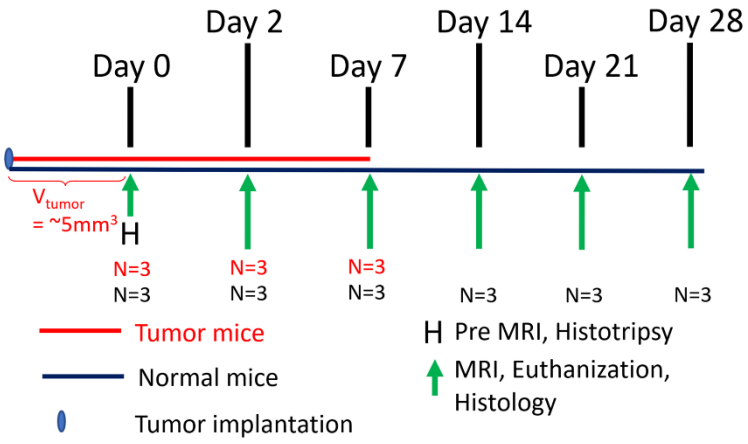

Figure 3.1. Timeline of this study. Tumor-bearing mice are indicated by red and normal mice by dark blue. The treatment for tumor-bearing mice was initiated when the tumor reached approximately 5mm3 in size, and the mice were imaged on days 0, 2, and 7 post-treatment. Day 0

is at the histotripsy treatment day, which corresponded to 10-14 days after tumor implantation. The normal mice were imaged at days 0, 2, 7, 14, 21, and 28 after histotripsy. There were 3 mice for each time point. At the designated study endpoint, the mice were euthanized with brains dissected for histology.

Table 3.1. MR Parameters

	Fsems T2	**Gems T2***	**Fsems T1**
TR/TE (ms)	2000/45	200/5.5	500/8
Flip Angle (degree)	90/180	20/30	90/180
Slice Thickness (mm)	1	1	1
Field of view (mm)	25.6	25.6	25.6
Matrix (frequency x phase)	128 x 128	128 x 128	128 x 128
Scan Time (minutes)	4	4	4

Fsems = fast spin echo multi slice, Gems = gradient echo multi slice

On the day of histotripsy treatment and during MRI, an inhalation of isoflurane (1.5%-2.0%) in 1L/min of oxygen (SurgiVet V704001, Smiths Medical, Waukesha, WI, USA) was used to induce and maintain general anesthesia and respiratory rate of approximately 80 breathes per minute. Carprofen (Rimadyl, Pfizer, NY, USA) analgesic (5mg/kg) was injected subcutaneously prior to histotripsy treatment and subsequently once every 24 h for two days after the histotripsy procedure. Before the treatment, mice hair on the head was shaved and chemically depilated (Nair, Church & Dwight Company, Ewing Township, NJ, USA) to ensure that no trapped air bubbles could block acoustic access. After every histotripsy or MRI procedure, the animal was placed in a warm recovery chamber to fully wake up and rest before returning to the original cage with other mice.

The temperature of the mice during MR image acquisition was maintained at 36ºC-37ºC using an MR-compatible fiber optic temperature module and an MR-compatible heater system for small animals (1025T monitoring and gating system, SA instruments, Stony Brook, NY, USA). Every 15 minutes, the mouse temperature, breathing rate, isoflurane level, and oxygen level were recorded. During histotripsy treatment, the mouse head was partially submerged in a degassed water tank, and this water temperature was maintained at 36ºC-38ºC using an immersion heater. A rectal temperature probe (#: 50304 Stoelting Co, Wood Dale, IL, USA) was also used to check and sustain the temperature of the mice. The protocol described in this manuscript and all mouse procedures were approved by the University of Michigan Institutional Animal Care Use Committee (IACUC).

3.2.3 Histotripsy treatment

A 1 MHz, 8-element small animal histotripsy transducer with a focal distance of 32.5mm which produced a peak rarefaction pressure of >28MPa was used to create histotripsy cavitation.

Approximately 3-5mm^3 volume histotripsy was delivered to both tumor-bearing and normal mice, targeting the tumor in tumor-bearing mice and similar location in normal mice. The treatment grid was formed by dividing the prescribed volume into 0.25mm spaced grid points for a raster scan. Each grid point was delivered with 15 pulses at 5Hz pulse repetition frequency (PRF).

3.2.4 MRI evaluation for treatment assessment

T2, T2*, T1, and T1-Gd (gadolinium) images were acquired to evaluate the transcranial histotripsy zone. T2 yielded the best histotripsy contrast and the clearest anatomy of the brain to detect any deformation caused by inflammation induced by the treatment. T2* highlighted any blood products in the mice, T1 combined with T2 signal exhibited the state of the blood product

from oxygenated, deoxygenated, methemoglobin, hemichromes to hemosiderin [39-40], and T1-Gd indicated whether the blood-brain-barrier (BBB) was open.

For quantitative evaluation in the MRI, all sequences were analyzed for hypointense pixels around the histotripsy zone to follow the hypointense volume change over time, and T1-Gd images were analyzed for hyperintense pixels around the histotripsy zone. Four standard deviations below or above the contralateral healthy region were used as a threshold to determine the pixels of interest. To extract volume information, the pixels of interest were counted and used for volume calculation:

$$V = sum([\#\ of\ pixels]_{HT} * res_{xy}^2) * (SliceThickness)$$

Where res_{xy} is the lateral resolution of MR image, and $[\#\ of\ pixels]_{HT}$ is the number of pixels that the histotripsy zone occupied. These data points were normalized and plotted to assess the treated volume change over time in both normal and tumor-bearing mice.

3.2.5 Histology

After euthanization of the animal, the skull was partially cut open along the suture and fixed in 10% formalin for over 24 hours. The brains were kept in shape by fixing them inside their skulls. Subsequently, the samples were extracted, cut coronally in half, and the front half of the brain, which included the olfactory bulbs, was packaged in a cassette to be sent to the University histology core (iLab, University of Michigan, Ann Arbor, MI, USA) to be embedded in paraffin and stained in H&E. 4um thick hematoxylin and eosin (H&E) slides were obtained every 1mm to correlate to MR images.

3.2.6 Interpretation of MRI and Histology

A blind reading of MR images and H&E histology slides was done to identify histotripsy boundary, homogenate, glioma tumor, and blood products with the help of a board-certified neuro-radiologist (Dr. Neeraj Chaudary, 14 years of experience) and a board-certified neuro-pathologist (Dr. Sandra Camelo-Piragua, 12 years of experience), respectively.

3.3 Result

3.3.1 Histotripsy on normal mice

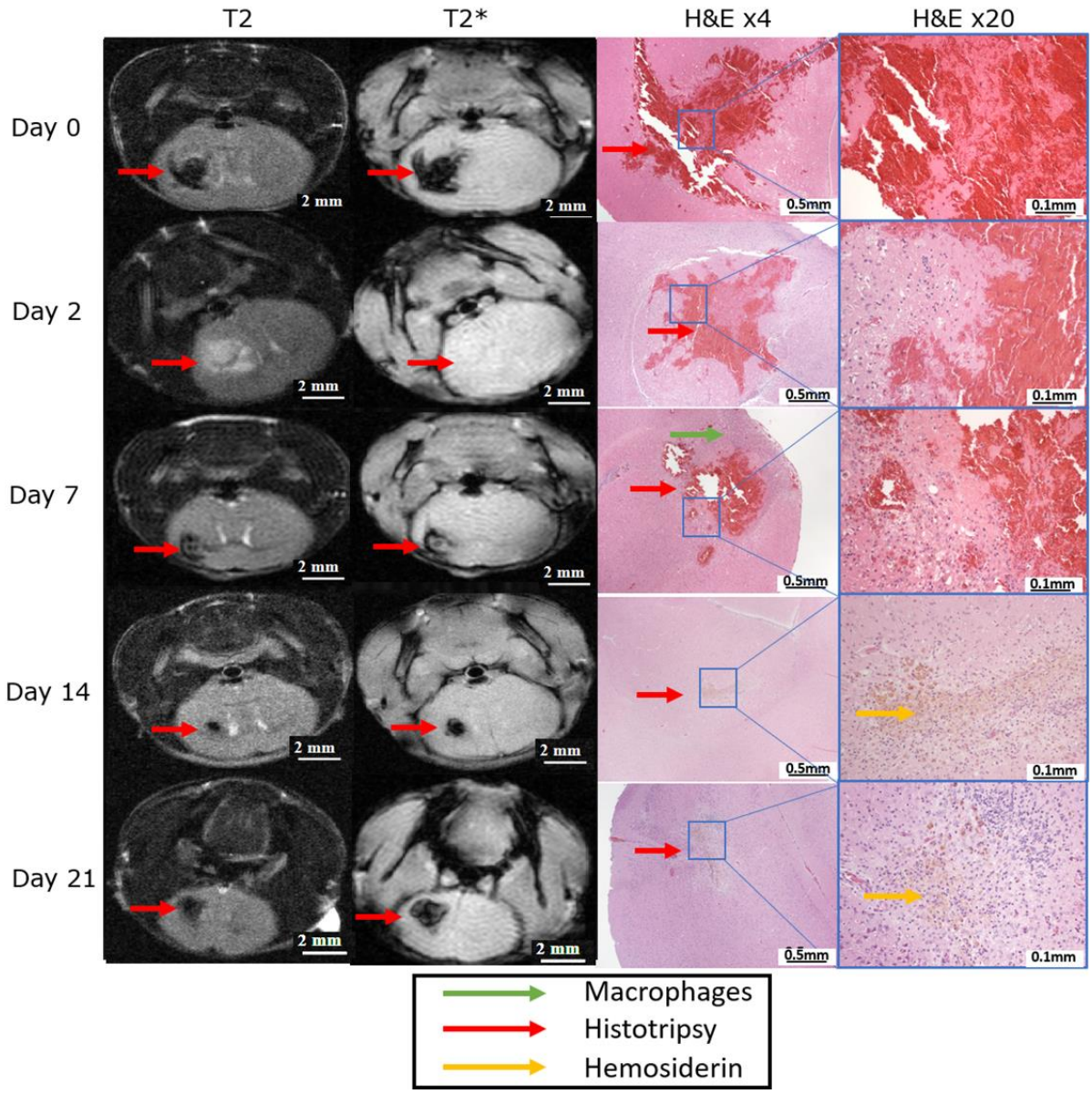

Figure 3.2. T2 and T2* MRI and H&E stained slides of normal mouse brain post-histotripsy. Histotripsy zones are pointed by red arrows, hemosiderin by orange arrows, and macrophages by the green arrow. Zoomed-in images of hemosiderin of day 28 mice can be found in Supplemental Figure 3.1. Day 0 is the day of histotripsy treatment.

MRI and histology of normal mouse brain treated by histotripsy led to acute, localized bleeding and subsequent wound healing (Fig. 3.2). On day 0, the histotripsy zone appeared hypointense on both T2 and T2* MR images and this could be seen as blood products in H&E slides. On day 2, the inflammation-induced edema appeared hyperintense on T2 and isointense on

T2*. This was evident in H&E slides with pockets of edema and liquid content surrounded by histotripsy-induced blood products. Day 7, the histotripsy boundary appeared hypointense on both T2 and T2* and the central area appeared hyperintense on T2. There was a significant clearance of blood products compared to mice on day 0 and the presence of macrophages around the histotripsy zone, indicative of the wound healing process. On day 14, the histotripsy zone still appeared hypointense on T2 and T2* but the red blood products had been resolved and the lesion was now present with hemichromes and hemosiderin residuals (orange arrow) and macrophages (green arrow). Macrophage intracellular hemosiderin shortened T2 and rendered the histotripsy zone hypointense. Similarly, on day 21, the histotripsy zone appeared hypointense on T2 and T2* MR images, and the lesion was covered by hemosiderin on H&E slides. These immune cells resided near the histotripsy zone after and resulted in a hypointense MR signal.

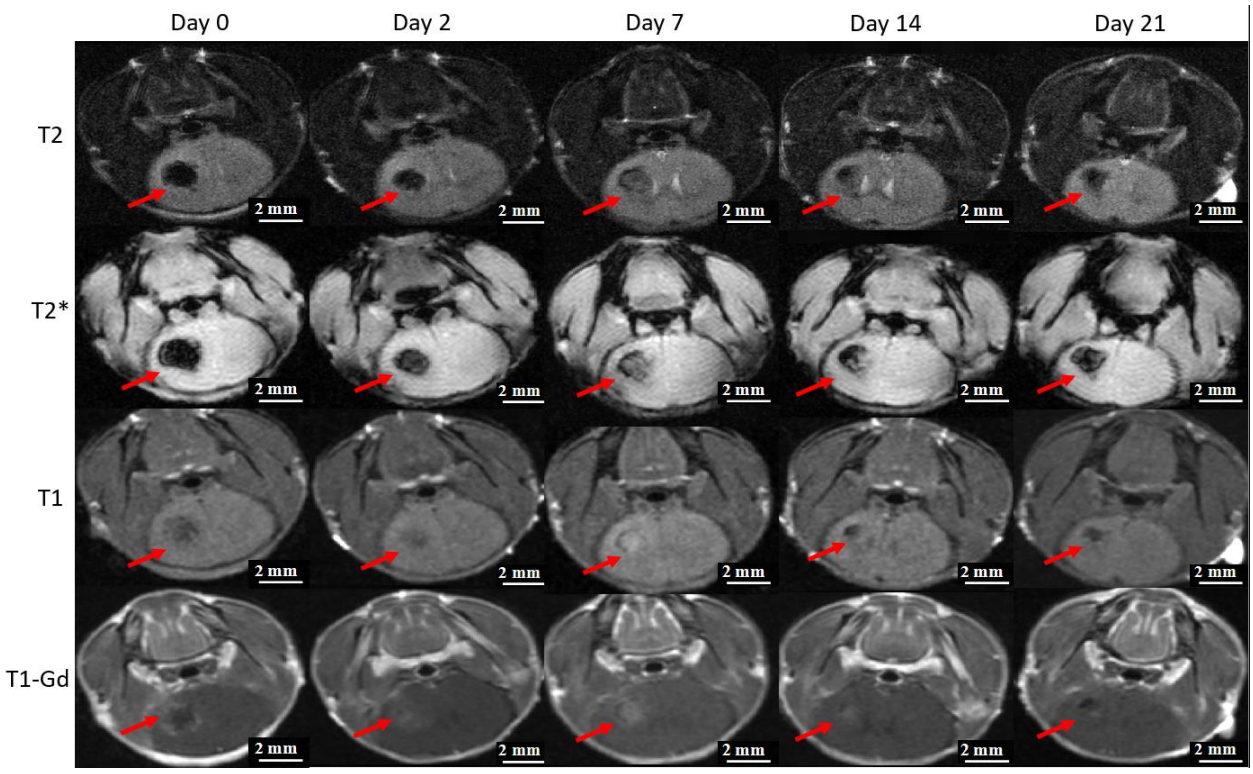

Figure 3.3. MRI of the normal mouse brain on days 0, 2,7, 14, and 21 post histotripsy. The red arrows show where the mouse brain was targeted. On day 0, the histotripsy zone on T2 and T2* images appeared hypointense, and on day 2, the zone stayed hypointense but smaller in size. This

is different from the response seen in the day 2 mouse in Figure 3.2. However, consistent throughout all the mice was the hypointense appearance of the histotripsy boundary on days 0, 7, 14, 21, and 28. On days 0 and 2 of the T1 images, the histotripsy zone appeared iso to hypointense, on day 7 hyperintense, and on days 14 and 21 hypointense. On day 0 of the T1-Gadolinium (Gd) image, Gd penetrated through the blood-brain barrier (BBB), and the periphery of the histotripsy zone was hyperintense. On day 2, the low, diffuse hyperintensity was observed, on day 7, peak hyperintensity was observed, and on days 14 and 21, the intensity gradually subsided.

The time evolution of the transcranial histotripsy ablation zone on all 4 sequences is captured in Figure 3.3**.** On T2 and T2* MRI, the appearance of the histotripsy boundary stayed hypointense with perimeter changes over time after treatment. A different response was observed on day 2 in the example shown in Figure 3.3 compared to the mouse observed on day 2 in Figure 3.2. For this particular mouse (Fig. 3.3), the histotripsy zone stayed hypointense, and in the mouse in Figure 3.2 and other mice observed, the histotripsy zone was hyperintense due to edema (Supplementary Fig. 3.2).

The ability of T1 and T2 to capture the state of blood products evolving from oxygenated blood, deoxygenated blood, methemoglobin, hemichrome, and to hemosiderin has been well documented [39-40]. On days 0 and 2, the histotripsy zone was hypointense due to the presence of deoxygenated blood resulting in long T1 and short T2. On day 7, the ablated zone was hyperintense on T1 and faintly hyperintense on T2 (more day 7 mice on Supplemental Figure 3.3), correlating to the T2 lengthening and T1 shortening effect of methemoglobin. Then the histotripsy zone evolved to a combination of hypo and hyperintense on T2 and isointense T1, suggesting the transformation to hemichromes on day 14. On day 21, the hypointensity was more evident than on day 14, suggesting the transformation of extracellular hemichromes digested to hemosiderin (long T1, short T2) by macrophages.

T1-Gd images displayed the BBB opening caused by histotripsy, both within and at the rim of the histotripsy region. Histotripsy mechanically disrupted the brain tissue and led to BBB opening which may be due to damage to the vasculature and the tight junction or inflammation as part of

the wound healing. This was observed immediately after the treatment: hyperintense rim suggesting BBB opening coupled with hypointense core, which was assumed to be a lack of gadolinium delivery in that area due to the destruction of blood vessels. On days 2 and 7, BBB remained open, marked by its hyperintensity, low intensity on day 2 most likely due to the presence of edema and inflammation preventing the Gd particles to exude, and peak intensity observed on day 7 as inflammation subsided. On day 14, the hyperintensity subsided and on day 21, the hyperintensity was unclear. This was concurrent with the wound healing seen in histological data in Figure 3.2.

The histotripsy zone was hypothesized to be mostly healed (e.g., devoid of blood products and presence of fibrosis) according to information from Figure 3.2 on days 14 and 21. Therefore, the ferromagnetic effect of iron particles remaining in the histotripsy zone and their ability to shorten T2 should be considered when interpreting the images. Through all this time, no significant changes in the appearance (e.g., fur color and weight) nor any behavior (e.g., grooming and exploration) changes of the mice were observed. However, adverse effects such as appearance and behavior changes (e.g., untidy fur and hyperreactivity upon gentle touch) were observed when histotripsy ruptured the ventricles in two mice. In this event, the overflowing cerebral fluid was visible under T2 images.

3.3.2 Histotripsy on tumor-bearing mice

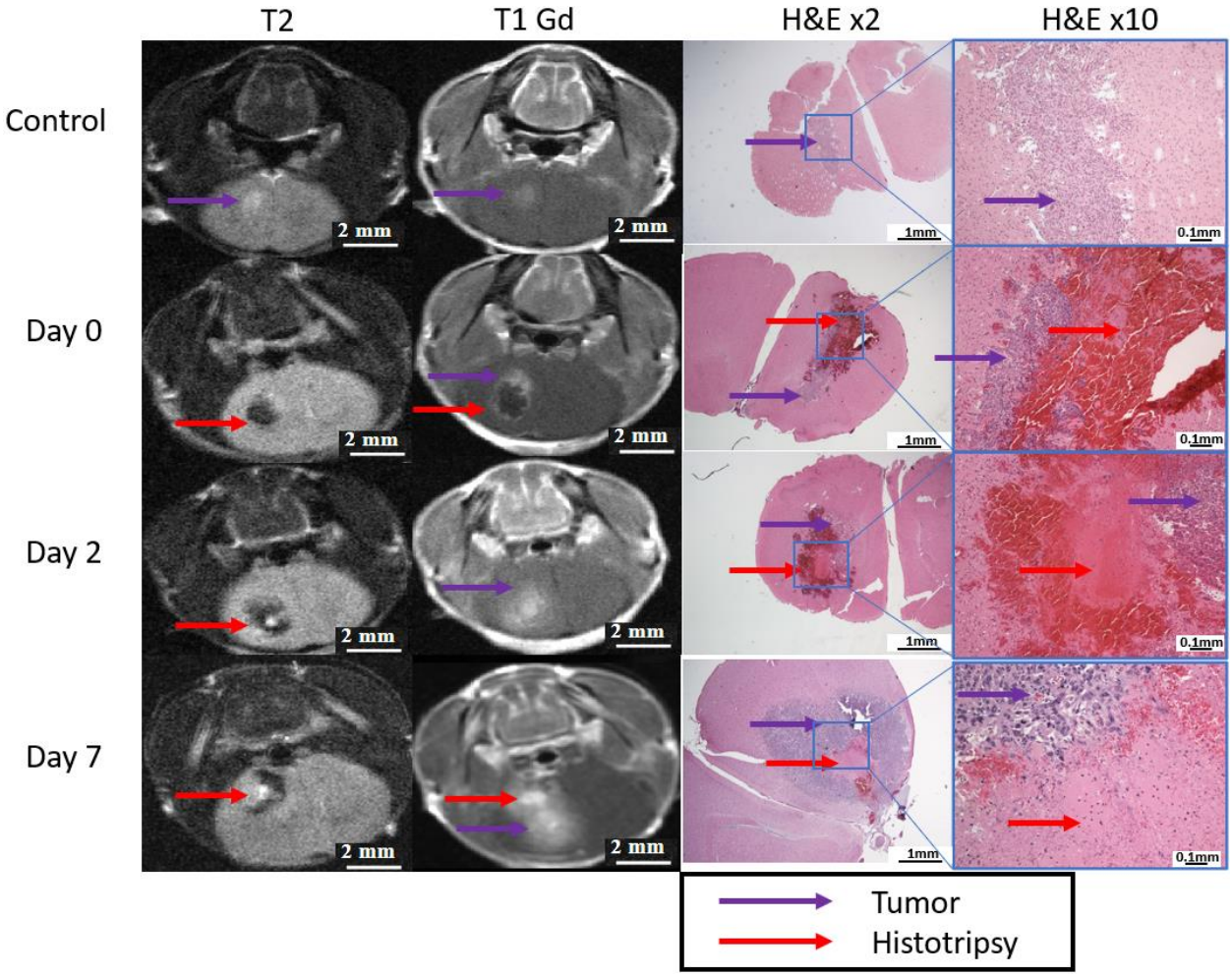

Figure 3.4. T2 and T1-Gd MRI and histology of tumor-bearing mice at days 0, 2, and 7 post histotripsy. The tumor was hyperintense, pointed with purple arrows and hypointense histotripsy zones with red arrows. The control untreated mouse is shown in the top row. On the T2 MR image, the tumor appeared hyperintense due to fluid content accumulated by the rapidly dividing glioma cells. On the T1-Gd MR image, the tumor appeared hyperintense due to the BBB opening caused by the glioma cells and the lack of tight junction formed during the rapid division, and this was shown in the H&E slide with disorganized purple tumor cells juxtaposed with pink evenly distributed healthy cells surrounding the tumor. The purple appearance was attributed to the dense population of nuclei present in the tumor region. Immediately after histotripsy (day 0), the histotripsy lesion was visible under T2 and T1-Gd. Additionally, T1-Gd highlighted the residual tumor cells indicated by purple arrows, which corresponded to the tumor cells distinguishable on histology. On day 2, the histotripsy zone was visible under T2 and not in T1-Gd, with the hyperintense central histotripsy zone in T2. This was correlated to homogenized acellular debris shown in H&E and the tumor cells were observed via T1-Gd but not with distinct clarity as seen on day 0. On day 7, the histotripsy lesion was still visible under T2 and the tumor under T1-Gd. H&E showed the cancerous cells rapidly replicating due to the aggressive nature of the glioma cell line used in this study.

T2 and T1-Gd MR images of tumor-bearing mice treated with histotripsy and corresponding H&E histology showed histotripsy lesion and tumor can be distinguished using radiological features (Fig. 3.4). On day 0, the tumor (hyperintense) and histotripsy ablation volume (hypointense) were well visualized on the T1-Gd image. On day 2, the histotripsy ablation zone was hypointense on T2 and the tumor was hyperintense on T1-Gd, but rather difficult to distinguish. On day 7, a histotripsy ablation was visible under T2 and the tumor under T1-Gd.

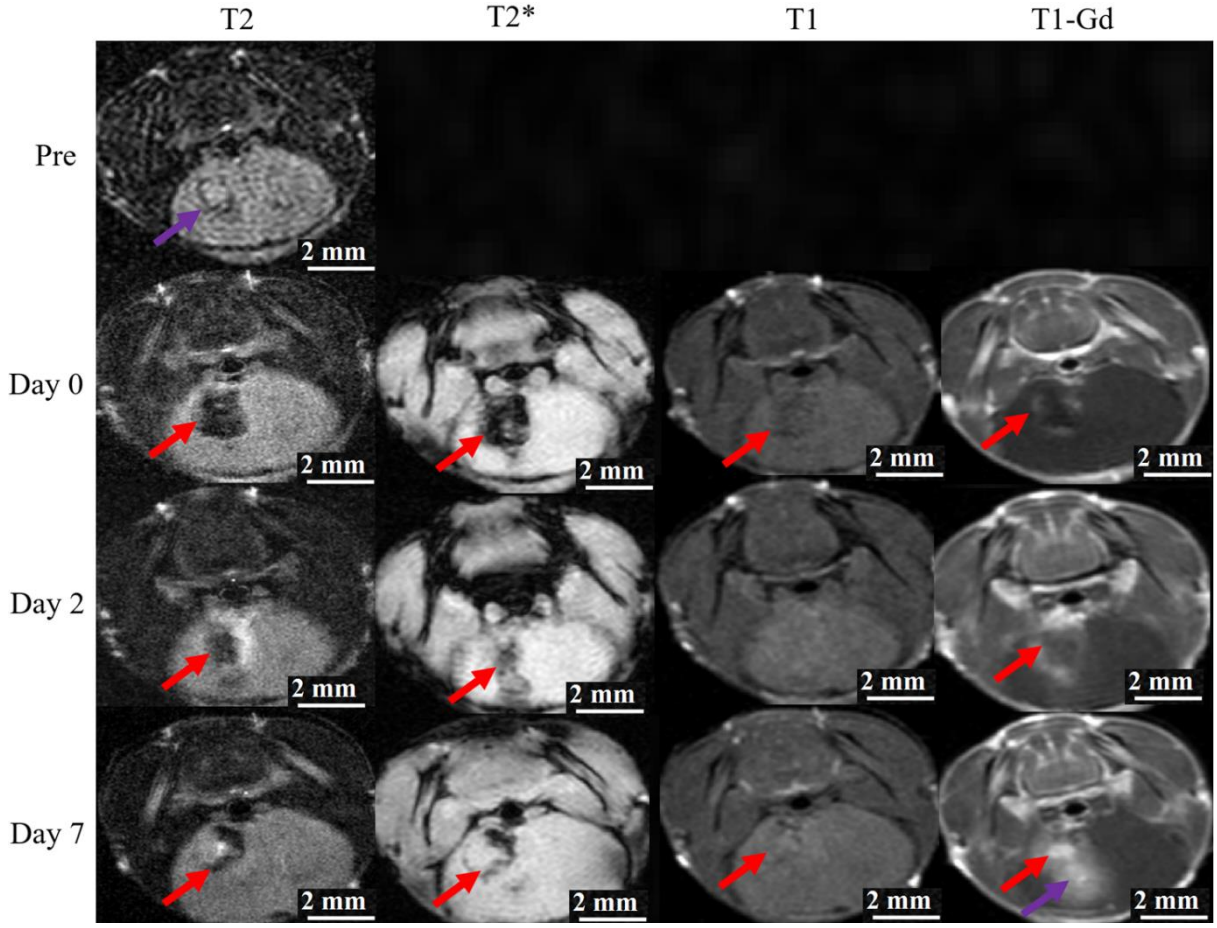

Figure 3.5. Representative MR images of a tumor-bearing mouse ablated at days 0, 2, and 7 post histotripsy. These MR images correspond to the day 7 mouse in Figure 4. For pre-treatment, only a T2 MR image was acquired to shorten the anesthetic duration of the mice used in this experiment. For post-treatment, T2, T2*, T1, and T1-Gd MR images are shown. The red arrows indicate the histotripsy zones, and the purple arrows denote residual tumors. Immediately after histotripsy (day 0), the histotripsy zone appeared hypointense on T2 and T2* and hypo to isointense to hypointense on T1 MRI. Gadolinium only lighted up the periphery of the histotripsy zone, showing a very similar appearance to normal mouse post-histotripsy. On day 2, T2 and T2* showed diffuse

histotripsy zone. On T1, the histotripsy zone could not be distinguished, but the histotripsy zone and residual tumors could be identified on T1-Gd. On day 7, the histotripsy zone has reduced in size, and a central hyperintensity was observed on T2. T1-Gd image indicated two different hyperintensity zones, one stronger and a weak hyperintense area.

The histotripsy zone was generally hypointense on T2 and T2* in the tumor-bearing mice, while in T1-Gd images, the histotripsy zone and tumor exhibited different hyperintensities (Fig. 3.5). The appearance of the histotripsy zone on T1-Gd was very similar to the appearance of the histotripsy zone in the normal mouse brain immediately after treatment, with central histotripsy zone hypointensity and peripheral hyperintensity due to Gd leakage. On day 2, the existing hypointensity was surrounded by a hyperintense rim in T2 MRI, due to inflammation-induced edema. Similarly, the histotripsy zone on day 2 appeared less hypointense and more diffuse than day 0 on T2* MRI, turned isointense on T1 MRI, and assumed a more diffuse hyperintense appearance in T1-Gd compared to day 0. On day 7, both hypointensity and hyperintensity around the histotripsy zone subsided, but a central hyperintensity remained on T2 MRI, which was correlated to the histotripsy-generated acellular homogenate according to histology.

On day 7 of T1 MRI, a mixture of hyperintense and hypointense pixels indicated the evolution of blood products to methemoglobin and hemosiderin inside the histotripsy zone. Finally, on T1-Gd MRI, two distinct hyperintense zones were present, one strong and one weak. The weak hyperintense area was correlated with the tumor according to histology, and the strong hyperintensity was correlated to the histotripsy zone. By day 7, the histotripsy zones were mostly indistinguishable on T1 and T1-Gd MRI but could be located with T2 and T2* MR images.

3.3.3 Histotripsy ablation zone evolvement over time

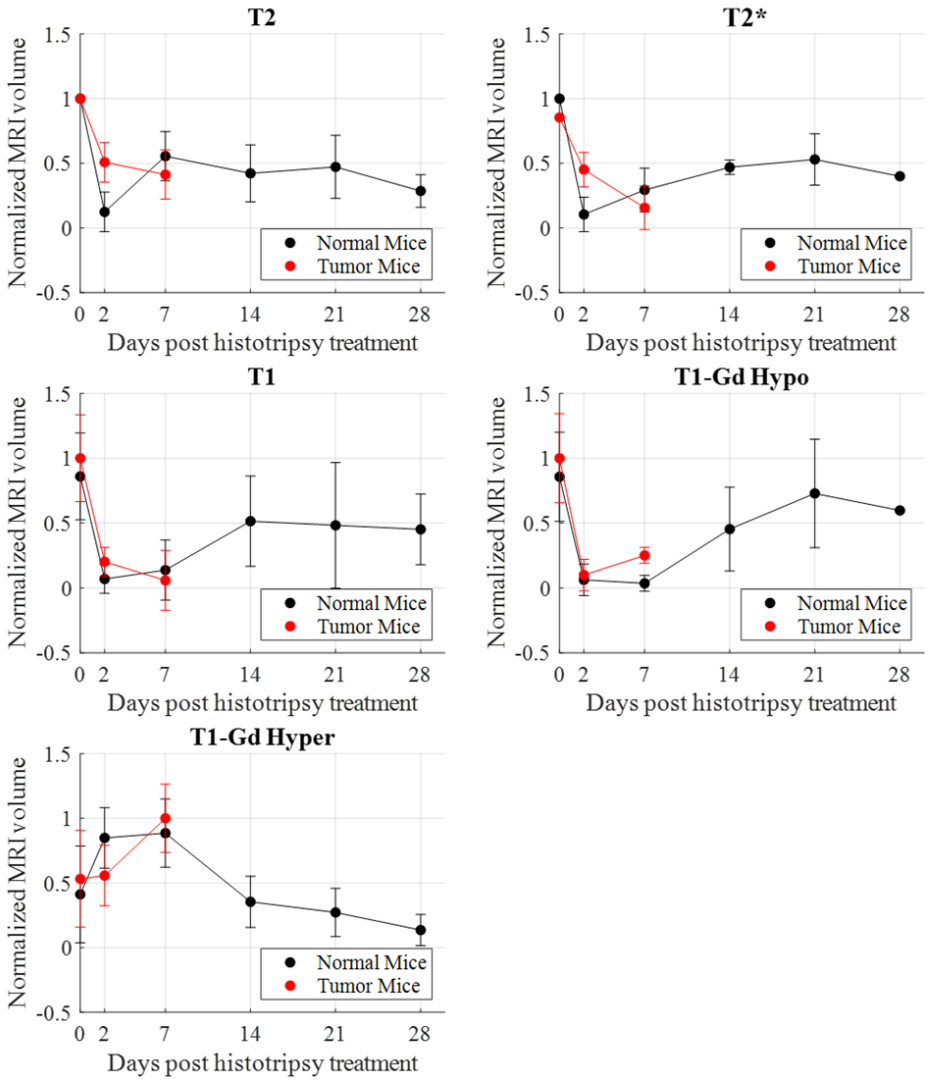

Figure 3.6. MRI hypo/hyperintense volume changes over time for tumor-bearing (red) and normal (black) mice. The graphs of T2, T2*, and T1 displayed hypointense volume only while the T1-Gd plot displayed both hypointense and hyperintense volumes. All volume points were normalized.

Different MRI sequences were used to analyze the change in the histotripsy ablation zone over time (Fig. 3.6). For both normal and tumor-bearing mice, there was a significant decrease in the hypointense volume on all sequences from day 0 to day 2 and a subsequent increase and maintenance of the hypointense histotripsy volumes. The largest volumes on day 0 of T2, T2*, T1, and T1-Gd were hypothesized to be due to the inflammation and bleeding that exaggerated the histotripsy size (i.e., blooming artifact), while throughout the next four weeks, the cleanup of the

histotripsy homogenate and decrease in the histotripsy zone size contributed to a smaller histotripsy volume observed in all images. However, the decrease in histotripsy size was offset by macrophages digesting the hemosiderin and residing in the histotripsy zone to distort the MR field as seen in Figure 3.2.

The T1-Gd hyperintensity is caused by the BBB opening induced by transcranial histotripsy. The T1-Gd hyperintense region in the brain of normal mice peaked between days 2 and 7, and continually subsided over days 14 through 28. Similar observations for all images were made in the acute to the subacute phase of tumor-bearing mice but no longitudinal trend could be established due to the exponential growth of the glioma tumor.

On H&E slides, the histotripsy zone was filled with red blood cells on day 0 and with edema on day 2. By day 7, the histotripsy zone decreased in size due to infiltration of macrophages and wound healing. By days 14 and 21, the majority of the red blood cells were removed, and the cavity created by histotripsy had decreased to a small pocket of hemosiderin. There was a mismatch between the decreasing histotripsy ablation zone (macroscopically and on histology) with time and the persistent presence of the hypointense zone in MRI after Day 7. This was likely attributed to the presence of hemosiderin in the macrophages residing near the ablation zone distorting the local MR field (blooming artifact).

3.3.4 MRI features of histotripsy follow-up

Table 3.2 summarizes the MRI features and the appearances (i.e., hypo or hyper-intense) of identifiable objects. The identifiable objects were histotripsy-generated acellular homogenate, histotripsy boundary, tumor, and blood products. On all days, the histotripsy zone mostly appeared hypointense on T2 and T2* MR images and hyperintense on T1-Gd. Within the histotripsy zone, damaged red blood cells exuded water and appeared hyperintense on T2 MR images. The tumor

appeared hyperintense on T2 MRI due to the high fluid content of the tumor cells and hyperintense on T1-Gd due to disruption of the BBB. The histotripsy-induced blood products were mostly hypointense on T2 and T2* MRI, but the T1 sequence displayed varied intensities, suggesting the subtle evolution of blood products from deoxygenated blood to methemoglobin and then to hemosiderin. The blood-brain barrier (BBB) opening caused by histotripsy appeared to close over time, evident by reduced hyperintensity on T1-Gd around the histotripsy perimeter. However, the state of BBB disruption induced by histotripsy needs further investigation.

Table 3.2. MRI appearances for objects of interest

Sequence	Identifying Object	T2		T2*		T1	T1-Gd
Day 0	**a)** Histotripsy (HT) Boundary **b)** HT Homogenate **c)** GBM Tumor **d)** Blood Product	a) Hypo b) Hyper c) Hyper	d) Hypo	a) Hypo b) Hyper c) Iso	d) Hypo	a) Iso b) Iso c) Iso d) Iso/hypo	a) Hyper b) N/A c) Hyper
Day 2			d) Hypo		d) Hypo	a) Iso b) Iso c) Iso d) Iso/hypo	
Day 7			d) Hyper		d) Iso	a) Hypo b) Iso c) Iso d) Hyper	
Day 14 & 21			d) Hypo		d) Hypo	a) Hypo b) N/A* c) N/A** d) Hypo	a) Hypo b) N/A c) Hyper

* Histotripsy homogenate is not easily distinguishable under T1.
** Tumor is not easily differentiable in T1.

Table 3.3 summarizes the MR imaging sequence that best visualizes certain features of the brain after histotripsy based on our observation. T2 is best for estimation of histotripsy zone respective to other anatomical features and the changes that may arise from inflammation such as

midline shift, T2* for isolating histotripsy zone, T1 for blood product evolution, and T1-Gd for BBB disruption that arises from the residual tumor or histotripsy zone.

Table 3.3. Recommendation of MR sequences for transcranial histotripsy

Sequence	Edema/inflammation/midline shift	Histotripsy Zone	Blood Product Evolution	Residual Tumor	BBB Disruption
T2	+++	++	++	+	-
T2*	-	+++	-	-	-
T1	+	-	+++	-	-
T1-Gd	++	+	-	+++	+++

3.4 Discussion

This paper investigated the MRI features for transcranial histotripsy follow-up of tumor-bearing mice and normal mouse brains. In the acute phase, both normal mice and tumor-bearing mice treated with histotripsy displayed similar MR features that were correlated to histological features. Both T2 and T2* visualized the histotripsy zone; T1 best visualized the evolution of histotripsy blood product; T1-Gd best visualized the residual tumor and the BBB opening induced by the mechanism of histotripsy.

Overall, the tumor-bearing mice displayed a similar MR appearance as seen in normal mice in the acute phase (days 0 and 2): hypointense histotripsy damage core on T2, T2*, and hypointense core with a hyperintense rim on T1-Gd. However, by day 7, the aggressive nature of the tumor hindered proper distinction between histotripsy and tumor. This difficulty can be mitigated by using multi-sequence MR images to separately identify the residual tumors and histotripsy zone. For example, T2 and T2* can identify the histotripsy zone, and T1-Gd images can distinguish GBM tumors. In future studies, specialized MR sequences such as dynamic contrast-enhancement (DCE) [40] can be utilized to further investigate the vascular dynamic differences between GBM

tumors and histotripsy zones and diffusion-weighted sequences (DWI) [41] to characterize histotripsy zone by mitigating the signal distortion effects of iron and to estimate the size of histotripsy volume. From the set of limited data on DCE T1-Gd images, the histotripsy zone on day 7 displayed more hyperintensity than the residual tumor surrounding the histotripsy zone. In a previous study on ex vivo tissue, apparent diffusion coefficient (ADC) images were used to identify the histotripsy zone [42].

The limitation of this study includes the short observation period for tumor-bearing mice treated with histotripsy. The GL261 cell line is highly aggressive and invasive [43]. In this study, partial treatment was applied intentionally to leave a residual tumor to distinguish on MRI from the histotripsy zone. If a less aggressive cell line were to be used, a longer period of radiological and histological data could have been obtained to further investigate the therapeutic effects of transcranial histotripsy in the presence of a tumor.

The temporal evolution of brain histotripsy was studied in the *in vivo* mouse brain. This histotripsy treatment recovery followed a standard healing process observed post-damage: acute (days 0 and 2) minor bleeding and minor edema to subacute (days 7 to 14) immune activity, and chronic (day >14) residual hemosiderin. Bleeding was not found outside the histotripsy zone and quickly subsided after treatment. No observable complications (i.e. weight, appearance, and behavior) were detected in mice treated with histotripsy for the duration of this study. In addition, we were able to characterize the nature and characteristics of the BBB opening induced by histotripsy. Our study suggests that the BBB opening induced by histotripsy is temporary as it is evident within hours of treatment and is restored at the 14-21 day window. We plan to quantify the size of the BBB opening induced by histotripsy using varying diameter dextran particles [44] and the tight junction damage and recovery via histology.

The MR appearance and the evolution of the histotripsy zone exhibited a very similar appearance to the hematoma in the brain [38]. One minor discrepancy was in the hyperacute phase (day 0 or less than 24 hours) of histotripsy. When a hematoma forms, oxygenated blood first fills the space which appears isointense on T1 and hypointense on T2. However, in the case of histotripsy, the cavitation mechanically fractionated tissue as well as red blood cells in the focal region, and therefore, the ruptured red blood cells lost oxygen quickly, leading to minor hypointense T1 and hypointense T2 in the treated mice. After this stage, the appearance of the histotripsy zone stayed consistent with literature where deoxygenated blood transformed into methemoglobin, hemichrome, and finally to hemosiderin.

There was a discrepancy between MRI features and histological features in the late stages of transcranial histotripsy. By days 14 and 21, the histotripsy zone underwent wound closing and was devoid of red hemoglobin, and the size of the histotripsy zone decreased. However, in MR images, the histotripsy zone did not change in size and appeared hypointense. This was attributed to the subtlety of the state and the location of the blood product [38,39]. In the chronic phase of histotripsy, the macrophages encountered extracellular hemichromes which did not impact T1 but slightly elongated T2 (i.e. isointense T1 and slightly hyperintense T2) and removed them by absorbing them. These macrophages then absorbed the blood products to intracellular hemosiderin, which elongated T1 and shortened T2 (i.e. hypointense T1 and T2) despite the decreased size of the histotripsy zone on histology.

The radiological and histological features of histotripsy treatment were different from traditional neuro-interventional technologies such as radiofrequency, transcranial magnetic resonance-guided focused ultrasound (tcMRgFUS), LITT, and radiosurgery. For thermal therapies such as radiofrequency, tcMRgFUS, and LITT, little blood products were observed due to slow

heating of the tissue, and a large edema ring defined the perilesional area [33]. On the other hand, radiosurgery lesions only became evident a month after therapy on MRI. The transcranial histotripsy produced a treatment zone that was immediately visible on MRI. There was acute, localized bleeding, but was resolved within a week of treatment and was safely handled by the treated animal.

There were concerns of the high-pressure ultrasound used in histotripsy that may negatively impact the well-being of the animal. The histotripsy transducer in this experiment produced >28MPa of rarefactional pressure in the focal region. This led to the expansion and subsequent collapse of the bubble cloud [37]. There was hemorrhage, edema, and inflammation within the histotripsy targeted region, but no evidence of damage or blood products outside of the targeted region. There was no observable mouse behavior change, indicating histotripsy treatment was well tolerated.

This study investigated the basic MRI features of transcranial histotripsy in correlation with histological findings in the murine brain and murine glioma model, leading to a better understanding of the long-term safety of transcranial histotripsy as well as the temporal profile of changes post histotripsy treatment. This natural history of transcranial histotripsy MRI and histology information on mice will be instrumental for future histotripsy brain studies.

3.5 Appendix

Supplemental Figure 3.1—Day 28 normal mice histotripsy T2, T2* MRI, and corresponding H&E histology. The red arrow indicates histotripsy zone and the yellow arrows point to the hemosiderin, which appear brown/orange in H&E slides.

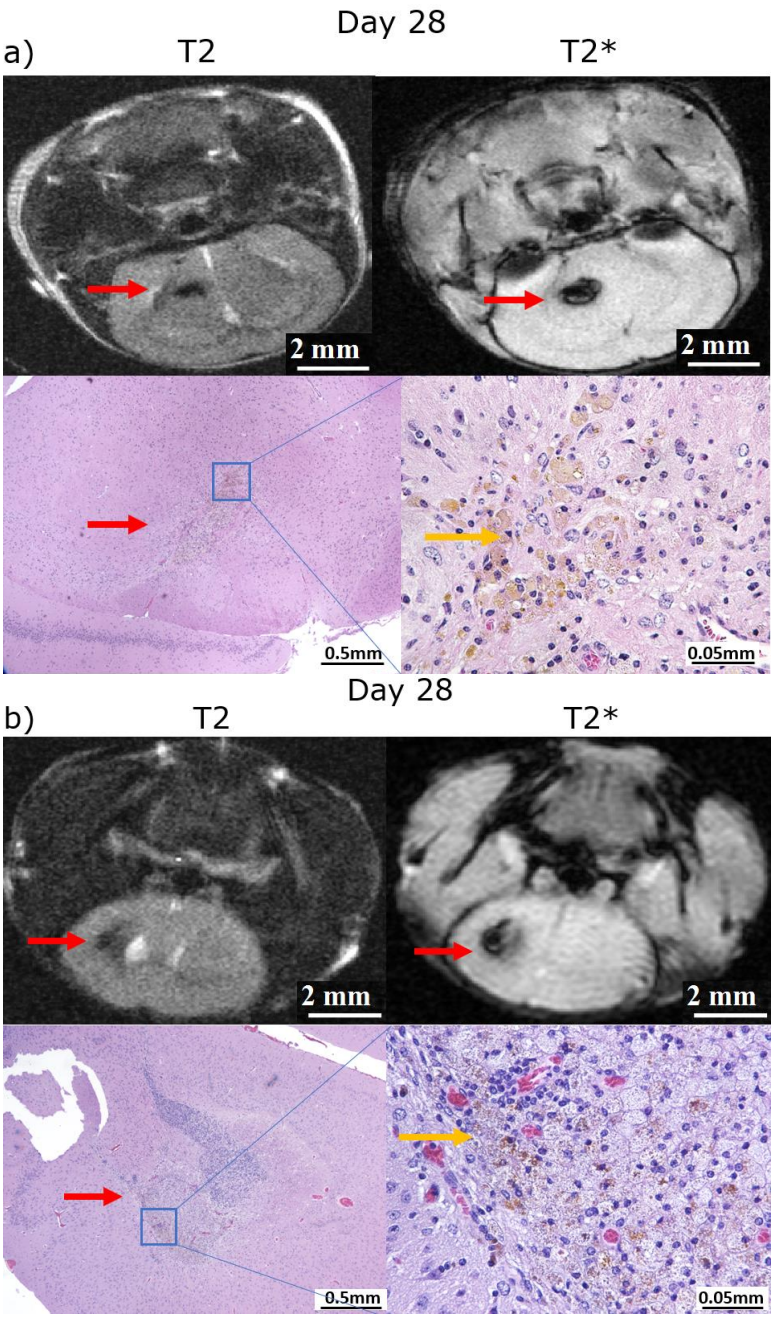
Day 28
a)
T2
T2*
2 mm
2 mm
0.5mm
0.05mm
Day 28
b)
T2
T2*
2 mm
2 mm
0.5mm
0.05mm

Supplemental Figure 3.2—day 2 normal mice brain MRI collage. 3 mice are presented in total and the histotripsy target is pointed by red arrows. On day 2, histotripsy zones appear hyperintense on T2 or are invisible under T2* and T1, due to edema. T1-Gd images show faint hyperintensity, indicating slow penetration of Gd across the BBB opening. However, the Mouse 1 T1-Gd image showed uncharacteristic hyperintensity. This may be attributed to the histotripsy zone located near the perimeter of the brain and resulting in Gd leakage into non-brain locations.

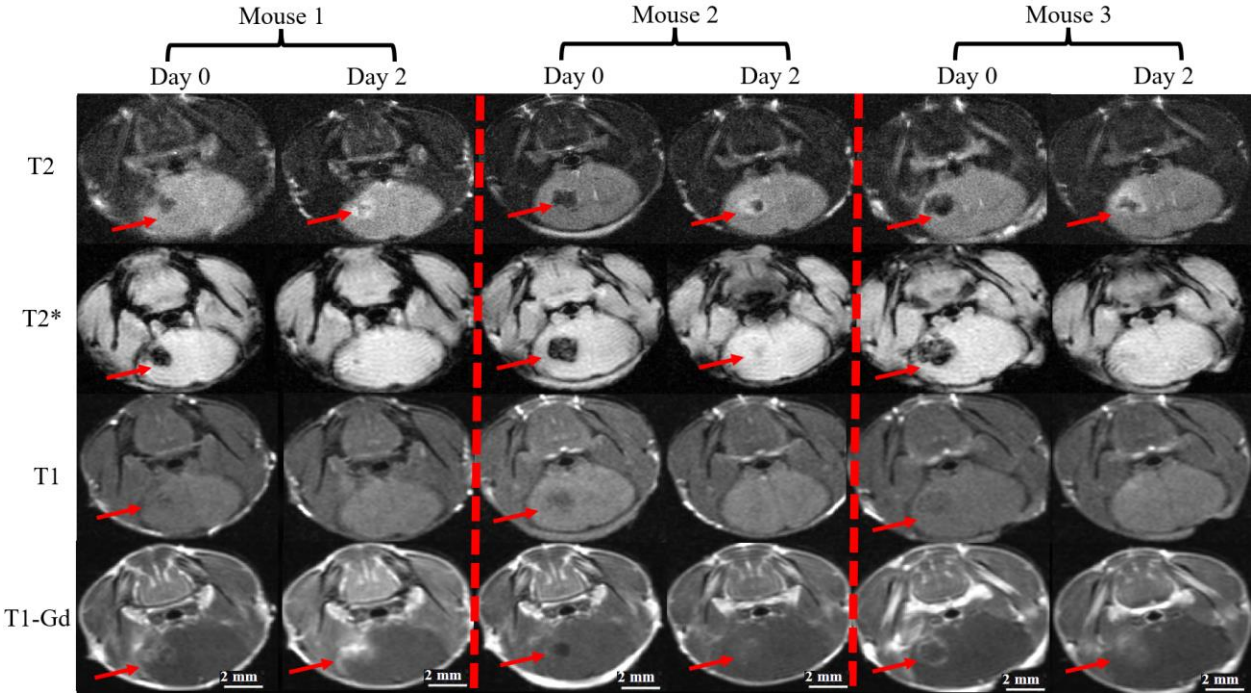

Supplemental Figure 3.3—Day 7 normal mice MRI and H&E slides. As mentioned, the central histotripsy zone in T2 and T2* on day 7 of transcranial histotripsy on normal mice brain appear hyperintense. This is due to the macrophages cleaning up excessive hemoglobin around the histotripsy zone and leaving behind histotripsy homogenates. Histotripsy leads to rupturing of cells and blood products and exuding of intercellular fluid, which appears hyperintense on T2 and T2* MR images.

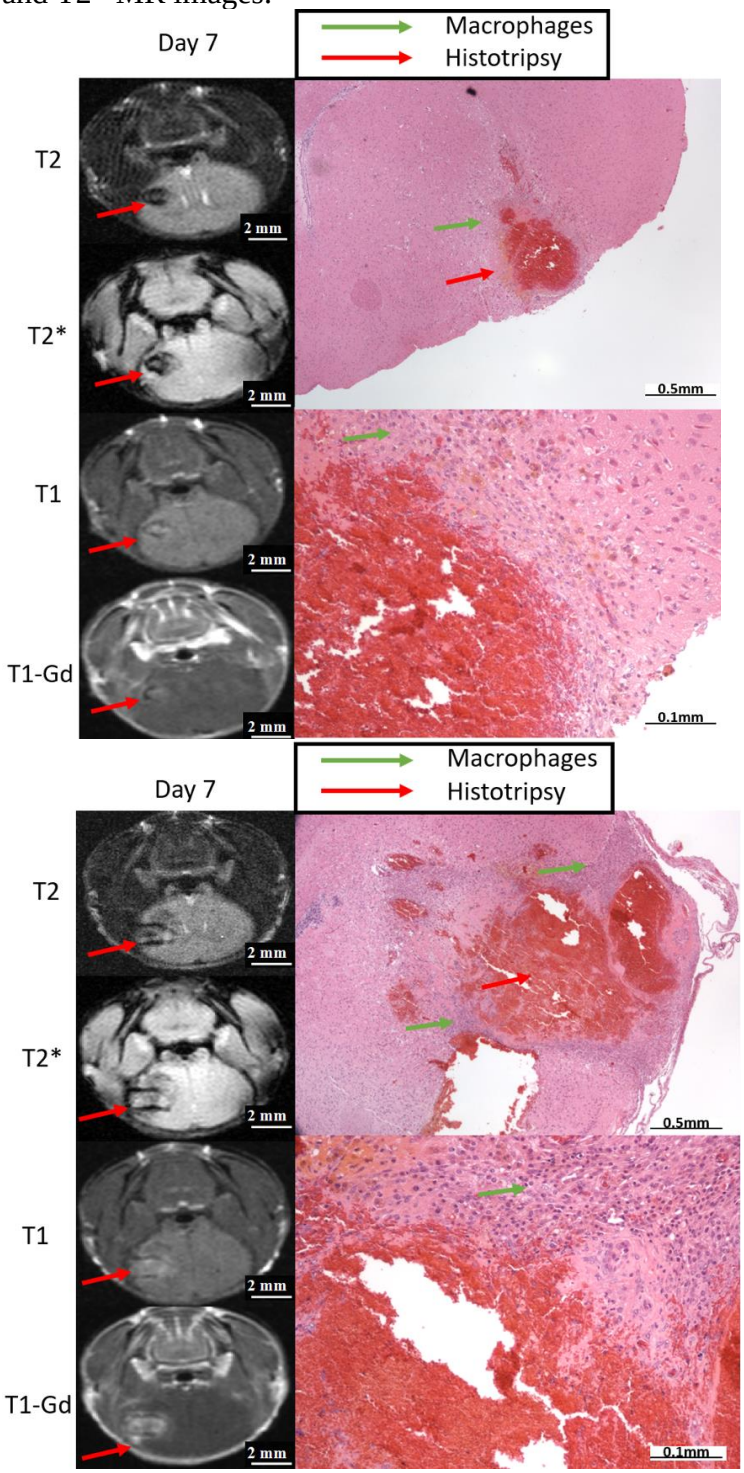

3.6 Reference

[1] S. J. Groiss, L. Wojtecki, M. Sudmeyer, and A. Schnitzler, "Deep brain stimulation in Parkinson's disease," *Ther. Adv. Neurol. Disord.*, vol. 2, no. 6, pp. 379–391, 2009, doi: 10.1177/1756285609339382.

[2] A. F. Hottinger, K. G. Abdullah, and R. Stupp, *Current Standards of Care in Glioblastoma Therapy*. 2016.

[3] R. A. Patchell, P. A. Tibbs, J. W. Walsh, and R. J. Dempsey, "A Randomized trial of surgery in the treatment of single metastases to the brain," *New English J. Med.*, vol. 322, no. 8, pp. 494–500, 1990.

[4] R. Sawaya *et al.*, "Neurosurgical Outcomes in a Modern Series of 400 Craniotomies for Treatment of Parenchymal Tumors," *Neurosurgery*, vol. 42, no. 5, pp. 1044–1055, May 1998, doi: 10.1097/00006123-199805000-00054.

[5] R. J. Komotar, M. L. Otten, G. Moise, and E. S. Connolly, "Radiotherapy plus concomitant and adjuvant temozolomide for glioblastoma—A critical review," *Clin. Med. Oncol.*, vol. 2, pp. 421–422, 2008, doi: 10.4137/cmo.s390.

[6] P. W. Sperduto *et al.*, "Survival in Patients with Brain Metastases: Summary Report on the Updated Diagnosis-Specific Graded Prognostic Assessment and Definition of the Eligibility Quotient," *J. Clin. Oncol.*, vol. 38, no. 32, pp. 3773–3784, 2020, doi: 10.1200/JCO.20.01255.

[7] A. Carpentier *et al.*, "Real-time magnetic resonance-guided laser thermal therapy for focal metastatic brain tumors," *Neurosurgery*, vol. 63, no. 1 SUPPL., pp. 21–29, 2008, doi: 10.1227/01.NEU.0000311254.63848.72.

[8] R. Medvid *et al.*, "Current applications of MRI-guided laser interstitial thermal therapy in the treatment of brain neoplasms and epilepsy: A radiologic and neurosurgical overview," *Am. J. Neuroradiol.*, vol. 36, no. 11, pp. 1998–2006, 2015, doi: 10.3174/ajnr.A4362.

[9] A. Franzini *et al.*, "Ablative brain surgery: an overview," *Int. J. Hyperth.*, vol. 36, no. 2, pp. 64–80, 2019, doi: 10.1080/02656736.2019.1616833.

[10] [H. J. Schwarzmaier *et al.*, "MR-guided laser-induced interstitial thermotherapy of recurrent glioblastoma multiforme: Preliminary results in 16 patients," *Eur. J. Radiol.*, vol. 59, no. 2, pp. 208–215, 2006, doi: 10.1016/j.ejrad.2006.05.010.

[11] Z. Izadifar, Z. Izadifar, D. Chapman, and P. Babyn, "An Introduction to High Intensity Focused Ultrasound: Systematic Review on Principles, Devices, and Clinical Applications," *J. Clin. Med.*, vol. 9, no. 2, p. 460, Feb. 2020, doi: 10.3390/jcm9020460.

[12] Y. Meng *et al.*, "MR-guided focused ultrasound enhances delivery of trastuzumab to

Her2-positive brain metastases," vol. 4011, no. October, pp. 1–9, 2021.

[13] . M. Jones, M. A. O'Reilly, and K. Hynynen, "Transcranial passive acoustic mapping with hemispherical sparse arrays using CT-based skull-specific aberration corrections: A simulation study," *Phys. Med. Biol.*, vol. 58, no. 14, pp. 4981–5005, Jul. 2013, doi: 10.1088/0031-9155/58/14/4981.

[14] D. Weintraub and W. J. Elias, "The emerging role of transcranial magnetic resonance imaging–guided focused ultrasound in functional neurosurgery," *Mov. Disord.*, vol. 32, no. 1, pp. 20–27, 2017, doi: 10.1002/mds.26599.

[15] M. Rao, E. Hargreaves, A. Khan, B. Haffty, and S. Danish, "Magnetic Resonance-Guided Laser Ablation Improves Local Control for Postradiosurgery Recurrence and/or Radiation Necrosis," *Congr. Neurol. Surg.*, vol. 74, no. 6, 2014, doi: 10.1227/NEU.0000000000000332.

[16] N. Lipsman *et al.*, "MR-guided focused ultrasound thalamotomy for essential tremor: A proof-of-concept study," *Lancet Neurol.*, vol. 12, no. 5, pp. 462–468, 2013, doi: 10.1016/S1474-4422(13)70048-6.

[17] N. Y. Jung, C. K. Park, M. Kim, P. H. Lee, Y. H. Sohn, and J. W. Chang, "The efficacy and limits of magnetic resonance–guided focused ultrasound pallidotomy for Parkinson's disease: A Phase I clinical trial," *J. Neurosurg.*, vol. 1306, no. 6, pp. 1853–1861, 2019, doi: 10.3171/2018.2.JNS172514.

[18] D. Coluccia *et al.*, "First noninvasive thermal ablation of a brain tumor with MR-guided focused ultrasound," *J. Ther. Ultrasound*, vol. 2, no. 1, pp. 1–7, 2014, doi: 10.1186/2050-5736-2-17.

[19] T. Mainprize *et al.*, "Blood-Brain Barrier Opening in Primary Brain Tumors with Non-invasive MR-Guided Focused Ultrasound: A Clinical Safety and Feasibility Study," *Sci. Rep.*, vol. 9, no. 1, pp. 1–7, Dec. 2019, doi: 10.1038/s41598-018-36340-0.

[20] N. Lipsman *et al.*, "Blood-brain barrier opening in Alzheimer's disease using MR-guided focused ultrasound," *Nat. Commun.*, vol. 9, no. 2336, 2018, doi: 10.1038/s41467-018-04529-6.

[21] A. D. Maxwell, T. Y. Wang, L. Yuan, A. P. Duryea, Z. Xu, and C. A. Cain, "A tissue phantom for visualization and measurement of ultrasound-induced cavitation damage," *Ultrasound Med. Biol.*, 2010, doi: 10.1016/j.ultrasmedbio.2010.08.023.

[22] T. L. Hall, J. B. Fowlkes, and C. A. Cain, "A real-time measure of cavitation induced tissue disruption by ultrasound imaging backscatter reduction," *IEEE Trans. Ultrason. Ferroelectr. Freq. Control*, vol. 54, no. 3, pp. 569–575, 2007, doi: 10.1109/TUFFC.2007.279.

[23] S. P. Allen, "Magnetic Resonance Imaging Guidance for Histotripsy Therapy," 2016, [Online]. Available: https://deepblue.lib.umich.edu/handle/2027.42/133238.

[24] R. Singh, A. J. Putnam, B. Fowlkes, E. Johnsen, and C. Cain, "Histotripsy Intrinsic Threshold for Cavitation," vol. 41, no. 6, pp. 1651–1667, 2016, doi: 10.1016/j.ultrasmedbio.2015.01.028.Effects.

[25] Z. Xu, T. L. Hall, and C. A. Cain, "Histotripsy : focused ultrasound therapy by mechanical tissue fractionation," 2003.

[26] T. J. Ziemlewicz, C. S. Cho. (2021, January 27 – 2026, January). "The HistoSonics System for Treatment of Primary and Metastatic Liver Tumors using Histotripsy." Clinical Trial Identifier: NCT04572633. https://clinicaltrials.gov/ct2/show/NCT04572633

[27] T. Gerhardson, J. R. Sukovich, A. S. Pandey, T. L. Hall, C. A. Cain, and Z. Xu, "Catheter Hydrophone Aberration Correction for Transcranial Histotripsy Treatment of Intracerebral Hemorrhage: Proof-of-Concept," *IEEE Trans. Ultrason. Ferroelectr. Freq. Control*, vol. 64, no. 11, pp. 1684–1697, 2017, doi: 10.1109/TUFFC.2017.2748050.

[28] J. R. Sukovich, J. J. MacOskey, J. E. Lundt, T. I. Gerhardson, T. L. Hall, and Z. Xu, "Real-Time Transcranial Histotripsy Treatment Localization and Mapping Using Acoustic Cavitation Emission Feedback," *IEEE Trans. Ultrason. Ferroelectr. Freq. Control*, vol. 67, no. 6, pp. 1178–1191, 2020, doi: 10.1109/TUFFC.2020.2967586.

[29] T. Gerhardson *et al.*, "Histotripsy Clot Liquefaction in a Porcine Intracerebral Hemorrhage Model," *Clin. Neurosurg.*, vol. 86, no. 3, pp. 429–436, 2020, doi: 10.1093/neuros/nyz089.

[30] T. Gerhardson, J. R. Sukovich, A. S. Pandey, T. L. Hall, C. A. Cain, and Z. Xu, "Effect of Frequency and Focal Spacing on Transcranial Histotripsy Clot Liquefaction, Using Electronic Focal Steering," *Ultrasound Med. Biol.*, vol. 43, no. 10, pp. 2302–2317, 2017, doi: 10.1016/j.ultrasmedbio.2017.06.010.

[31] J. R. Sukovich *et al.*, "Targeted Lesion Generation Through the Skull Without Aberration Correction Using Histotripsy," *IEEE Trans. Ultrason. Ferroelectr. Freq. Control*, vol. 63, no. 5, pp. 671–682, 2016, doi: 10.1109/TUFFC.2016.2531504.

[32] Lu *et al.*, “Transcranial MR-guided Histotripsy System,” *IEEE Trans. Ultrason. Ferroelectr. Freq. Control*, vol. 68, no. 9, pp. 2917–2929, 2021, doi: 10.1109/TUFFC.2021.3068113.

[33] W. J. Elias *et al.*, “A magnetic resonance imaging, histological, and dose modeling comparison of focused ultrasound, radiofrequency, and Gamma Knife radiosurgery lesions in swine thalamus,” *J. Neurosurg.*, vol. 119, no. 2, pp. 307–317, 2013, doi: 10.3171/2013.5.JNS122327.

[34] T. Worlikar *et al.*, “ Effects of Histotripsy on Local Tumor Progression in an in vivo Orthotopic Rodent Liver Tumor Model,” *BME Front.*, vol. 2020, pp. 1–14, 2020, doi: 10.34133/2020/9830304.

[35] S. W. Choi *et al.*, “Stereotactic Transcranial Focused Ultrasound Targeting System for Murine Brain Models,” *IEEE Trans. Ultrason. Ferroelectr. Freq. Control*, vol. 68, no. 1, pp. 154–163, 2021, doi: 10.1109/TUFFC.2020.3012303.

[36] W. N. Arifin and W. M. Zahiruddin, “Sample Size Calculation in Animal Studies Using Resource Equation Approach,” *Malays. J. Med. Sci.*, vol. 24, no. 5, p. 101, Sep. 2017, doi: 10.21315/MJMS2017.24.5.11.

[37] J. J. Macoskey *et al.*, “Soft-Tissue Aberration Correction for Histotripsy,” *IEEE Trans. Ultrason. Ferroelectr. Freq. Control*, 2018, doi: 10.1109/TUFFC.2018.2872727.

[38] W. G. Bradley, “MR appearance of hemorrhage in the brain,” *Radiology*, vol. 189, no. 1, pp. 15–26, 1993, doi: 10.1148/radiology.189.1.8372185.

[39] . Allkemper *et al.*, “Acute and subacute intracerebral hemorrhages: Comparison of MR imaging at 1.5 and 3.0 T - Initial experience,” *Radiology*, vol. 232, no. 3, pp. 874–881, 2004, doi: 10.1148/radiol.2323030322.

[40] A. C. Crouch, A. A. Cao, U. M. Scheven, and J. M. Greve, “In Vivo MRI Assessment of Blood Flow in Arteries and Veins from Head-to-Toe Across Age and Sex in C57BL/6 Mice,” *Physiol. Behav.*, vol. 176, no. 5, pp. 139–148, 2017, doi: 10.1007/s10439-019-02350-w.In.

[41] V. Baliyan, C. J. Das, R. Sharma, and A. K. Gupta, “Diffusion weighted imaging: Technique and applications,” *World J. Radiol.*, vol. 8, no. 9, p. 785, 2016, doi: 10.4329/wjr.v8.i9.785.

[42] S. P. Allen *et al.*, “The response of MRI contrast parameters in in vitro tissues and tissue mimicking phantoms to fractionation by histotripsy,” *Phys. Med. Biol.*, vol. 62, no. 17, pp. 7167–7180, 2017, doi: 10.1088/1361-6560/aa81ed.

[43] D. A. Reardon *et al.*, “Glioblastoma eradication following immune checkpoint blockade in an orthotopic, immunocompetent model,” *Cancer Immunol. Res.*, vol. 4, no. 2, pp. 124–135, 2016, doi: 10.1158/2326-6066.CIR-15-0151.

[44] H. Chen and E. E. Konofagou, “The size of blood-brain barrier opening induced by focused ultrasound is dictated by the acoustic pressure,” *Journal of Cerebral Blood Flow and Metabolism*, vol. 34, no. 7. pp. 1197–1204, 2014, doi: 10.1038/jcbfm.2014.71.

Chapter 4 Characterization of Blood-Brain Barrier (BBB) Opening Induced by Transcranial Histotripsy in Murine Brains

This Chapter has been submitted as a full paper to Ultrasound in Medicine and Biology and is under review.

4.1 Introduction

The blood-brain barrier (BBB) is a highly selective and restrictive barrier that exists at the interface between the blood vessel wall and the neuronal tissue in the brain which serves as a critical defense, preventing harmful agents or hematologically mediated antigens from entering the brain parenchyma [1]. The unique property of BBB is the existence of a well-developed junctional complex between brain endothelial cells, particularly the tight junctional complex to eliminate any paracellular space and exchange between neighboring cells [2]. However, BBB limits more than 98% of small-molecule drugs and nearly all large-molecule drugs from reaching the brain parenchyma in therapeutically relevant concentrations [3], which is the major hurdle for drug-based brain therapy. ZO-1 and Claudin-5 are tight junctional proteins (TJPs) reported to play key roles in the restrictive permeability property of BBB. ZO-1 is hypothesized to regulate the recruitment and anchoring of transmembrane tight junctional proteins (i.e claudin-5), while claudin-5 plays a major role in limiting the paracellular space. Any dysfunction associated with the disorganization of the tight junction complex leads to BBB permeability often seen in various neuropathological conditions like neurodegenerative and neuroinflammatory [2].

Low-amplitude ultrasound combined with microbubbles has been demonstrated to temporally open the BBB [4-5]. Using ultrasound applied from outside the skull, microbubbles can be activated to oscillate in the blood vessels and apply shear stress to the vessel wall, which causes the opening of the tight junction in the BBB and can be used to open the BBB selectively and reversibly for localized drug delivery [6-7]. Numerous preclinical works have been done to investigate microbubble-mediated focused ultrasound (FUS) induced BBB opening (BBBO) for the delivery of various components such as antibodies [8-9] and therapeutic agents [10-11]. Microbubble-mediated FUS BBB opening typically uses frequencies of 200kHz – 5MHz and peak pressure of 0.3 – 1.5 MPa. The pulse duration of 10-100 milliseconds and a duty cycle of 1-20% are often used [12], although continuous wave [13] or microsecond-length pulses [14] have also been shown effective in BBBO. Multiple clinical trials are ongoing using magnetic resonance-guided FUS (MRgFUS) and implantable FUS devices for drug delivery in human patients to treat brain tumors [15] and Alzheimer's disease [16].

Histotripsy is a focused ultrasound ablation technique that generates cavitation to mechanically fractionate the target tissue using high-pressure, microsecond-length ultrasound pulses [17-18]. The rapid expansion and collapse of cavitation microbubbles exert high strain and stress on the targeting tissue and disrupt the cellular membrane and structures [19]. Transcranial histotripsy has been shown to successfully ablate various locations inside the brain in preclinical studies *in vivo* porcine and mouse brains [20-21]. In contrast to the microbubble-mediated FUS that uses very low pressure (<1.5MPa) and relatively long ultrasound pulses (millisecond-length), histotripsy uses extremely high rarefaction pressure, (>20MPa) microsecond-length pulses and does not require microbubble injection [22]. Microbubble-mediated FUS typically induces stable cavitation [23], while histotripsy produces inertial cavitation, resulting in significantly higher

mechanical strain and stress [19]. There was early evidence of BBBO in the peripheral region of the histotripsy ablation zone. The mechanical stress induced by cavitation are known to decrease with distance away from the cavitation bubble, and this BBBO observed at the periphery of the histotripsy ablation zone could be due to the reduced mechanical stress at a farther distance from the inertial cavitation bubbles or the vessel endothelial damage induced by histotripsy.

In this study, the temporal characteristic of transcranial histotripsy-induced BBBO was studied for the first time via T1-gadolinium (Gd) MRI and TJ protein stains. In the normal brain, BBB prevents any molecules above 400 Da from entering, unless through transmembrane receptors, and therefore, no Gd enters the healthy brain parenchyma [24]. In the presence of a brain tumor (e.g. glioblastoma) or BBB opening, Gd, as a paramagnetic substance with a molecular weight of 574 Da, can enter the brain parenchyma and drastically shorten the T1 of surrounding molecules, appearing as hyperintense [25], making Gd a great tool for monitoring BBB opening. We used T1-Gd to qualitatively assess the BBB opening induced by histotripsy, H&E to assess damage to brain tissues and TJ protein immunofluorescent staining of ZO-1 and Claudin-5 to characterize the BBB tight junction complex within, at the boundary, and outside the histotripsy ablation zone. The knowledge gained would have an important indication for the development of transcranial histotripsy brain treatment.

4.2 Materials and Methods

4.2.1 Animal Procedure

Transcranial histotripsy was delivered to the normal brain of fifteen 8-10 weeks old BL6 female mice (Taconic Farms, Rensselaer, NY, USA) with the stereotactic procedure described in

[21] (Fig. 4.1). The stereotactic platform was used to avoid targeting the ventricles due to adverse reactions observed in previous studies.

After treatment, each mouse was monitored via MRI on days 0, 7, 14, 21, and 28 with the T1-Gd (Fast spin-echo multi-slice T1, TR/TE (500/8ms), slice thickness 1mm, lateral resolution 0.5mm, scan time 4 minutes) and T2* MRI (Gradient-echo multi-slice, TR/TE (200/5.5ms, flip angle: 20/30), slice thickness 1mm, lateral resolution 0.5mm, scan time 4 minutes) sequences (N=3 for each time point). 0.1ml of gadolinium (Gadoteridol: 558.7 Da [26], ProHance, 279.3mg/ml, Bracco, NJ, USA) was injected via the intraperitoneal cavity. A T2* MR image was acquired before Gd injection, and T1-Gd image was acquired approximately 10 minutes after injection. For each time point, after MRI, mice were euthanized from CO_2 overdose, and their brains were extracted for H&E, Claudin-5, and ZO-1-stained histology.

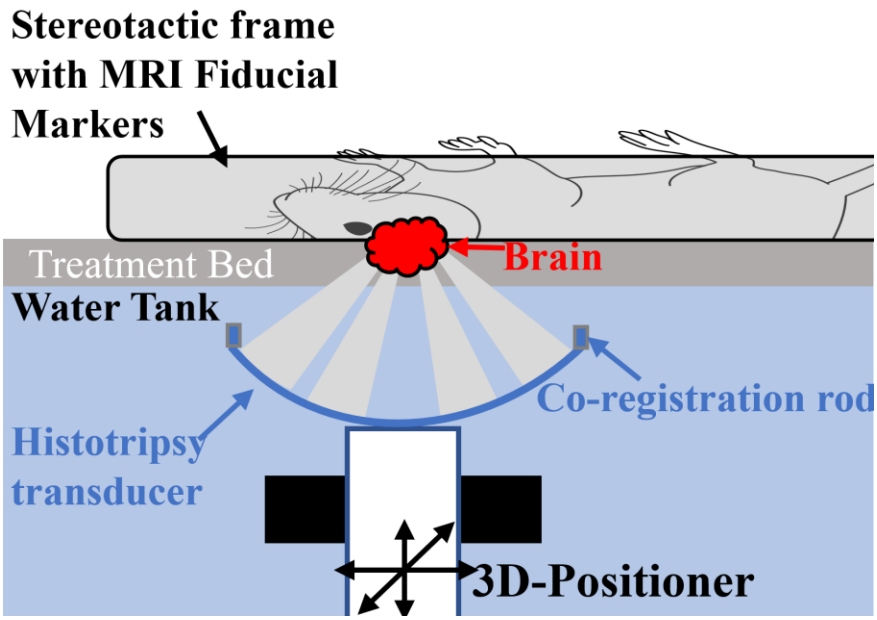

Figure 4.1. Schematic of the setup for transcranial histotripsy of the murine brain. A stereotactic frame with MRI fiducial markers immobilized the position of the mouse skull, and the co-registration features in the frame, treatment bed, and the histotripsy transducer allowed to co-register the focus of the brain respective to the brain. After co-registration, the histotripsy transducer was mechanically steered via a 3D positioner to deliver treatment to specific areas in the brain.

On the day of histotripsy treatment and during MR image acquisition, general anesthesia, as well as the body temperature of the mice, was maintained with the protocol described in [21]. Carprofen (Rimadyl, Pfizer, NY, USA) analgesic (5mg/kg) was administered subcutaneously on the day of histotripsy treatment and following two days after the treatment. Before the treatment, mice hair on the head was electrically shaved and chemically depilated (Nair, Church & Dwight Company, Ewing Township, NJ, USA) to ensure that no trapped air bubbles could block histotripsy pulses. After every histotripsy or MRI procedure, the animal was placed in a warm recovery chamber in isolation to fully wake up and rest before returning to the original cage with other mice. The protocol described in this manuscript and all mouse procedures were approved by the University of Michigan Institutional Animal Care Use Committee (IACUC).

4.2.2 Histotripsy Treatment

A 1 MHz, 8-focused element rodent histotripsy transducer (F# = 0.36) with a focal distance of 32.5mm was used to produce a peak rarefaction pressure of >28MPa to generate histotripsy cavitation.

A 3-5mm^3 volume in the brain in each mouse was treated with transcranial histotripsy. The treatment grid was formed by dividing the prescribed volume into 0.25mm spaced grid points for a raster scan. Each grid point was delivered with 15, 1.5-cycle pulses at 5Hz pulse repetition frequency (PRF) (0.0008% duty cycle).

4.2.3 Quantification of BBB opening through T1-Gd image

T1-Gd (gadolinium) images were acquired with a 7T small animal scanner (Varian Inc., Palo Alto, CA, USA) to evaluate the histotripsy ablation zone and the resulting BBB opening. T1-Gd hyperintensity indicated whether the BBB was open around the histotripsy ablation zone. For

quantitative evaluation of the BBBO based on T1-Gd images, MATLAB (Natick, MA, USA) was used to analyze T1-Gd MR images to calculate the pixel hyperintensity ratio of histotripsy side to contralateral healthy side and the average width of the hyperintense ring induced by BBBO (Fig. 4.2). The pixel hyperintensity ratio and the temporal changes over the study period were recorded to quantify the relative extent of gadolinium uptake on different days post-histotripsy (i.e. BBB opening permeability). Average ring widths of the histotripsy lesion were recorded to estimate the size of BBBO around the histotripsy ablation.

To quantify the hyperintense region induced by BBBO, the contralateral healthy region was selected, and the average pixel intensity and standard deviation (i.e. noise level) of the contralateral region were obtained. The threshold used to determine the hyperintense area on histotripsy side was determined by the region with pixel intensity exceeding the average pixel intensity of the contralateral untreated region plus four times the standard deviations:

$$Threshold = mean(normal_I) + 4\sigma_{normal}$$

Where $normal_I$ is the contralateral side pixel intensities and σ_{normal} is the standard deviation of the pixel intensity in the contralateral untreated side. Next, the pixel intensity ratio of the hyperintense region at the periphery of histotripsy ablation zone to the contralateral untreated region was calculated to indicate the relative enhancement of pixel intensity induced by BBBO using the equation below:

$$PI\ ratio = mean(lesion_I)/mean(normal_I)$$

Where $lesion_I$ is the hyperintense area in the histotripsy lesion determined by the threshold; mean($lesion_I$) is the mean pixel intensity over the $lesion_I$; mean($normal_I$) is the mean pixel intensity over the $normal_I$, which is the contralateral untreated side; and *PI ratio* is the pixel intensity ratio of the two. The average width of the hyperintense ring was determined by taking the average of

minor axis lengths of the thresholded hyperintense ROI binary mask as shown in Figure 4.2, 4th step.

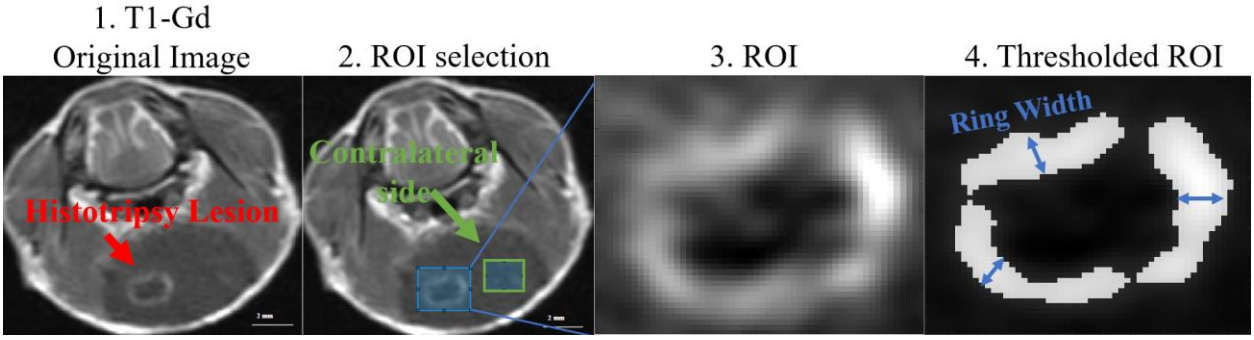

Figure 4.2. T1-Gd image processing steps for identifying hyperintensity and average ring width in murine brain treated with histotripsy. 1) Hyperintensity in the T1-Gd image of the brain around the histotripsy lesion indicates BBBO. 2) The contralateral untreated region of interest (ROI) was selected as well as the histotripsy lesion ROI. 3) The corresponding histotripsy ROI was thresholded. 4) The pixel intensity ratio and the average width of the hyperintense ring was calculated using the thresholded region.

4.2.4 Histology and T2 MRI*

After euthanization of the animal, the skull was partially cut open along the suture, and the brain was fixed in 10% formalin, in the skull for over 24 hours. Subsequently, the samples were extracted, cut coronally in half, and the front half of the brain, which included the olfactory bulbs, was packaged in a cassette to be sent to the University histology core (iLab, University of Michigan, Ann Arbor, MI, USA) to be embedded in paraffin and stained in H&E to be correlated with MR images.

T2* MR images were acquired to correlate with H&E for minor bleeding and iron products.

4.2.5 Immunofluorescence

Paraffin-embedded brain tissue was dewaxed and rehydrated through xylene and a series of alcohols (100, 95, 70 and 50%). Antigen retrieval was performed by boiling slides in 10 mM sodium citrate buffer (pH 6.0) for 10 min, followed by cooling and washing in PBS (pH

7.2). For immunofluorescence staining, brain samples were preincubated in blocking solution containing 5% normal goat serum and 0.05% Triton 100X (Sigma Aldrich) in PBS. Samples were then incubated overnight at 4°C with the following primary antibodies: claudin-5-Alexa-Flour 488 conjugated and ZO-1-Alexa Flour 594 conjugated. All samples were viewed on a confocal laser-scanning microscope (Nikon A1, Japan)

4.2.6 Interpretation of MRI and Histology

A blind reading of MR images was done to identify BBB opening and BBB repair by a board-certified neuro-radiologist and double, blinded reading of histology was performed by two board-certified neuro-pathologist.

4.3 Result

4.3.1 Qualitative Results

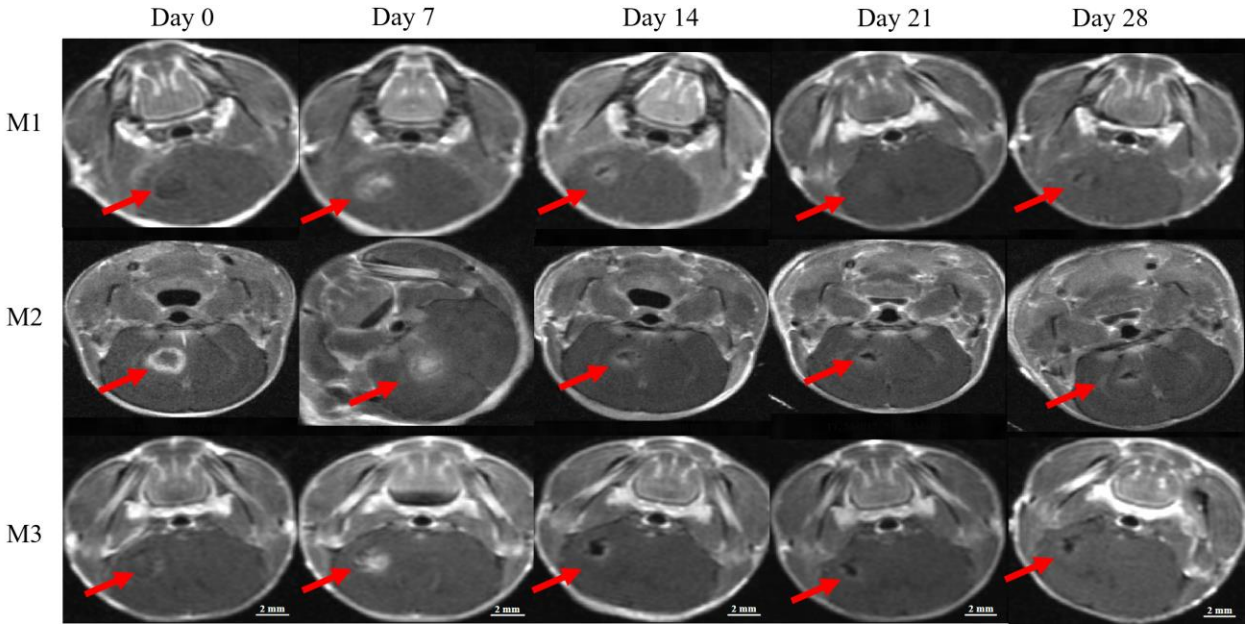

Figure 4.3.T1-Gd images of histotripsy-treated mice over 28 days. The histotripsy ablation zone is pointed out with red arrows and hyperintensity in the brain indicates BBBO via gadolinium (Gd)

enhancement. On day 0, the histotripsy ablation zone appeared dark, and the region surrounding the ablation zone boundary was hyperintense, indicating BBBO. The hyperintensity reached a peak by day 7, followed by a gradual decrease over the next 3 weeks.

T1-Gd MR images showed a rim of hyperintense zone surrounding the histotripsy ablation zone, indicating BBB opening (Fig. 4.3). On day 0 (histotripsy treatment day), the histotripsy ablation zone showed a hypo- to isointense core with a rim hyperintensity. On day 7, the volume of the hyperintense region reached a maximum and over days 14, 21, and 28, the hyperintensity around the histotripsy zone subsided gradually, indicating reduced gadolinium uptake in that area. On day 0, one mouse (M2) displayed a large hyperintense ring. In this mouse, hair was not completely removed, trapping air and blocking ultrasound propagation, thus a lower in situ pressure was used compared to the other two mice. It is likely that the lower pressure resulted in partial tissue disruption, which caused more Gd leakage into the partially disrupted region and a wider zone.

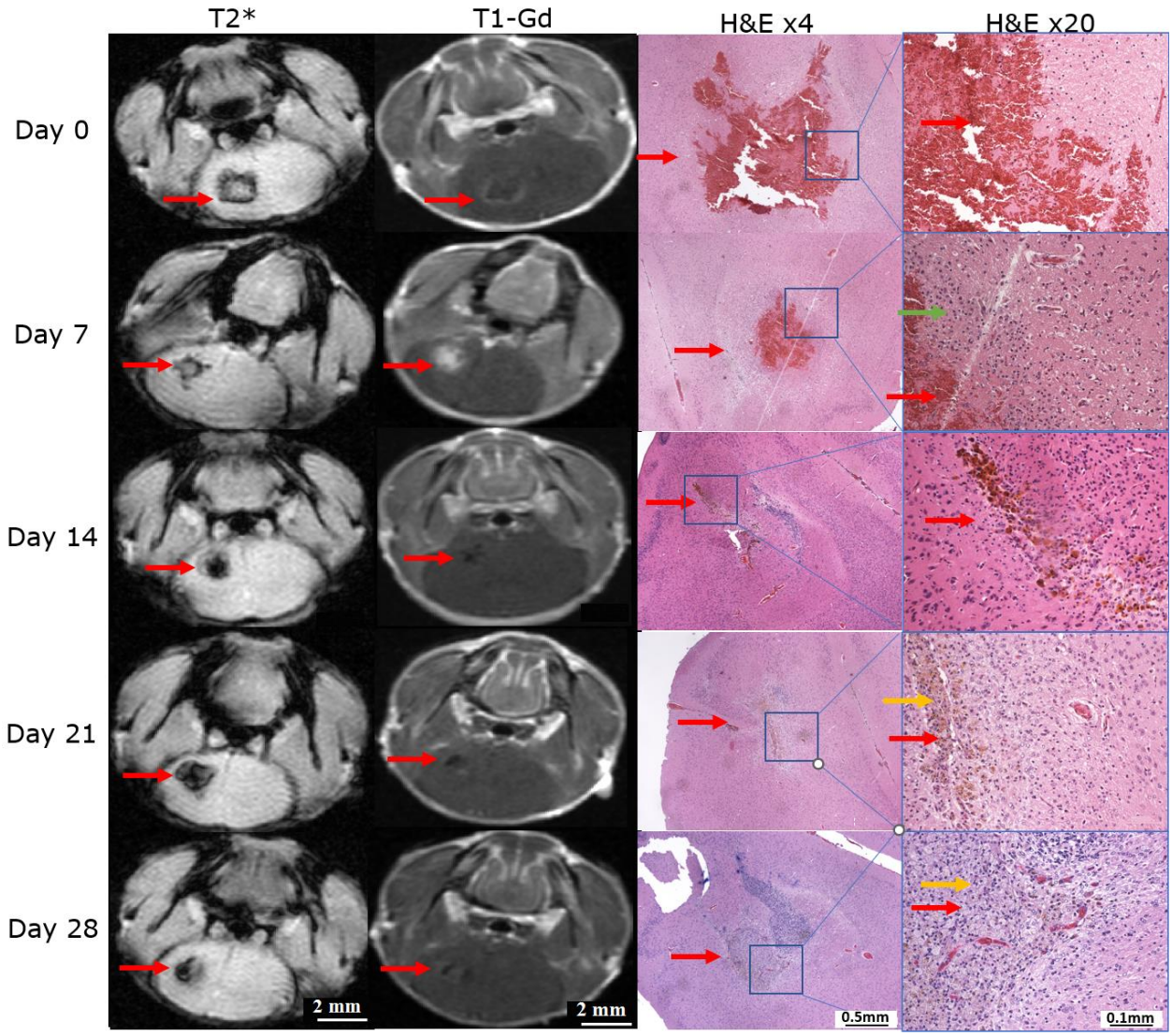

Figure 4.4. T2* images (first column), T1-Gd images (second column), H&E-stained slides at the lower (third column) and higher (fourth column) magnification of the histotripsy-treated murine brains. The red arrow indicates histotripsy ablation, the green arrow points to suspected immune cells, and the yellow arrow points to hemosiderin.

H&E histology slides showed that the histotripsy ablation core consisted of acellular debris and bleeding on days 0 and 7 (Fig. 4.4). Transcranial histotripsy led to acute bleeding in the treatment region that resolved within the first 7 days of treatment by histology and T2* MRI. Immune activity (Fig. 4.4**,** green arrow) was observed, noted by the wound healing as well as

multi-nuclear cells surrounding the histotripsy ablation, but this needs further investigation with specific staining.

On day 0, the hypointense zone in T2* MRI was correlated with coagulated blood and limited gadolinium uptake in the center of the ablation zone as seen on T1-Gd. On day 7, the blood products were significantly removed as seen in H&E and this was concurrent with the increased gadolinium leakage through the BBBO, as shown by hyperintensity on T1-Gd MRI. On day 14, the hyperintensity on T1-Gd appeared dimmer than the lesion on day 7, and this was observed with further cleaning of red blood cells and further reduction in histotripsy zone size. Similarly on days 21 and 28 of H&E histology, the processed blood products remained, and the histotripsy lesion size decreased, and the hyperintensity-induced by T1-Gd further decreased in intensity. T2* hypointense boundary perimeter remained stable in size despite decreasing histotripsy lesion size observed in H&E throughout the 28 days due to susceptibility artifact caused by the iron particles in the blood products.

The BBB tight junction damage was characterized by immunofluorescence staining of two TJ proteins, ZO-1 and Claudin-5 (Fig. 4.5). On the contralateral untreated side, an example of intact BBB can be observed as intensive and continuous staining for ZO-1 (red) and claudin-5 (green). The colocalization of the claudin-5 and ZO-1 (yellow = red + green) represent stable and functional TJ complex as the interaction between these two proteins play a critical role in regulating the paracellular space occlusion and BBB integrity.

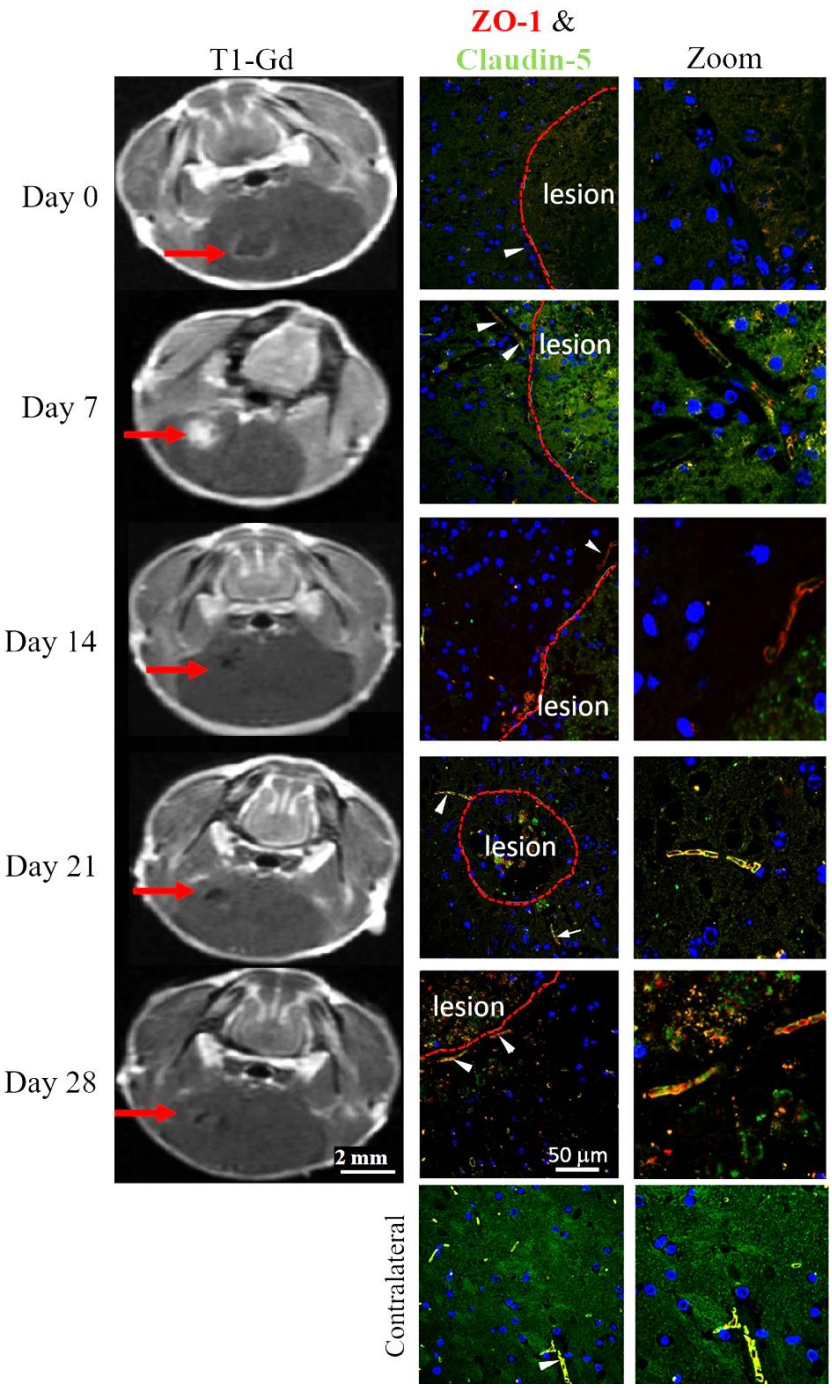

Figure 4.5. T1-Gd images, Claudin-5 (tight junction protein, green), ZO-1 (tight junction protein, red), and DAPI (cell nuclei, blue) stained slides of the mouse brain treated by transcranial histotripsy. Both claudin-5 and ZO-1 are essential protein components of BBB tight junction. The first column shows the T1-Gd images of the corresponding mice stained with Claudin-5, ZO-1 and DAPI on column two and three. The third column shows the zoomed-in version of the blood vessels (white arrowhead). Red dashed lines label the border of the lesion and the scale bar on the third column fifth row is 50um and applicable to the second column.

On day 0 of histotripsy, blood vessels in the histotripsy ablation and surrounding tissue showed little to no expression of claudin-5 and ZO-1 indicating the disassembly of TJ complex. On day 7-14 of histotripsy, partial TJ protein recovery is seen as blood vessels exhibit both claudin-5 and ZO-1 staining particularly on the border of ablation but characterized by the lack of TJ protein colocalization and the lack of continuous staining of both ZO-1 and claudin-5. The H&E histology and T1-Gd data of day 7 support this observation where the coagulated blood products in the center of the ablation have been cleaned and allowed the gadolinium leakage, indicating a presence of leaky BBB.

On days 21 and 28, the lack of coherent TJ proteins in the center of the lesion was observed while on the border of the lesion, most of blood vessels showed intensive staining for claudin-5 and ZO-1 and their colocalization. The scattered TJ proteins in blood vessels in the center of the lesion and the close-to-completely recovered TJ proteins at the periphery agree with the T1-Gd images and H&E: on days 21 and 28 post-histotripsy, the gadolinium leakage around the lesion and the size of the lesion have decreased significantly compared to days 0 and 7. The claudin-5 and ZO-1 staining indicate that the BBB "opening" induced by histotripsy is due to destabilization of TJ complex which is reversible and recovered after 7-14 days and within 28 days post histotripsy.

4.3.2 Quantitative Results

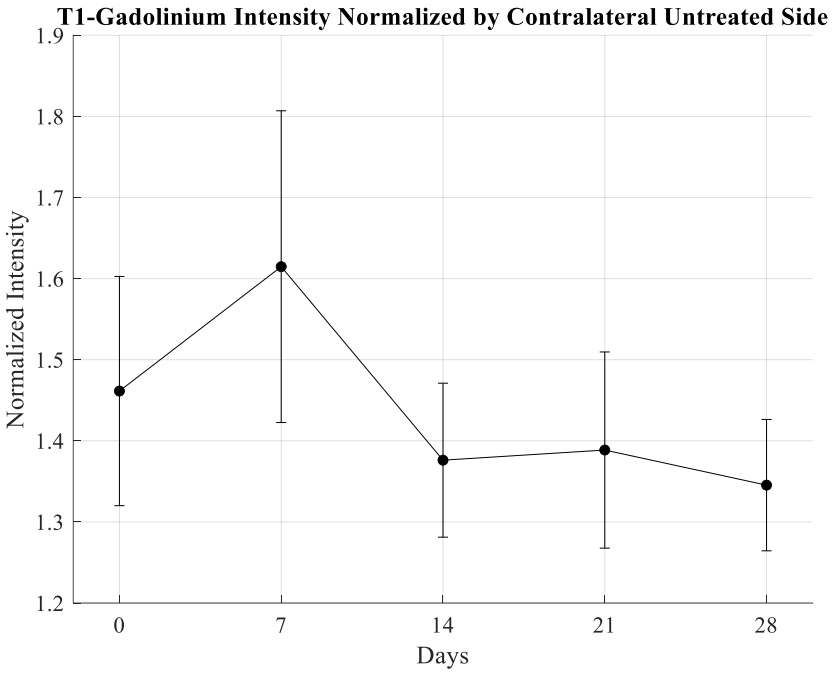

Figure 4.6. Histotripsy lesion intensity ratio change as observed in T1-Gd MRI. The hyperintensity ratio was calculated via dividing the mean of histotripsy hyperintense lesion intensity by mean of contralateral healthy side. The ratio indicated the relative amount of gadolinium uptake through the opening in the histotripsy zone.

T1-Gadolinium histotripsy zone hyperintensity ratio indicated that histotripsy lesion hyperintensity increased over the first 7 days post-histotripsy but subsided in intensity relative to the contralateral side from days 14 to 28 (Fig. 4.6). This trend indicates that gadolinium uptake around the histotripsy lesion peaked on day 7 and decreased after. This agrees with Figure 4.5 where on day 7, partially recovered TJ protein was observed on the *periphery* of histotripsy zone while on days 21 and 28, the TJ protein appearances resembled that of the healthy, contralateral side. Despite the healthy expression of TJ proteins on days 21 and 28, the histotripsy zone stayed 30% more hyperintense than the untreated contralateral side even after 28 days. This is attributed to the absence of BBB in the *center* of ablation zone.

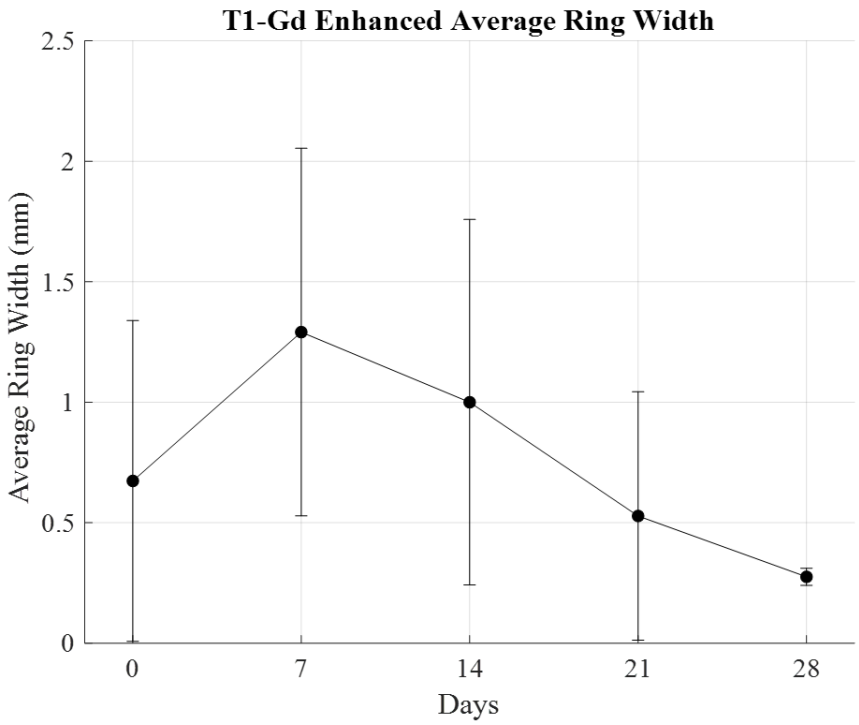

Figure 4.7. T1-Gd enhanced average ring width of histotripsy ablation zone as quantified in MRI. The ring width indicated the size of histotripsy-induced BBBO in millimeters as observed in T1-Gd MRI.

The average gadolinium-enhanced ring width, as an indication of histotripsy-induced BBB opening size, observed in T1-Gd MRI indicated that histotripsy-induced BBBO around the periphery of the ablation size peaks on day 7 and decreases after day 7 (Fig. 4.7). This trend is supported by observations made with H&E and TJ protein stains where the size of the histotripsy ablation zone decreases over time and the partially intact TJ proteins are visible after day 7. The enhancement ring width stayed around 0.3mm on day 28 despite the fully recovered periphery BBB.

4.4 Discussion

The BBB opening after histotripsy is investigated using T1-Gadolinium MRI and histology with two markers for the BBB integrity, TJP Claudin-5 and ZO-1, in the normal mouse brain. Histotripsy led to BBB disruption in the *center* of the ablation zone observed in T1-Gd MRI.

However, we found Gd penetration in the tissue *periphery* the histotripsy zone, and the permeability decreased over time in T1-Gd MRI. Immunofluorescence staining for claudin-5 and ZO-1 showed reversible TJP damage at the *periphery* of the histotripsy ablation zone, which indicated peak BBB opening at ~7 days of post-histotripsy and near-complete recovery at 21-28 days.

On day 0, the histotripsy treatment zone consisted of a center volume of hypointense zone surrounded by a slightly enhanced hyperintensity rim on T1-Gd MRI. The hypointense region within the histotripsy ablation zone is due to the coagulation of the ablated tissue and disrupted BBB. The hyperintense rim is explained by the BBB opening and is supported with the TJP damage observed at the periphery zone by Claudin-5 and ZO-1 absence of staining on days 0 and 7. On day 7, the hyperintensity increased on T1-Gd MRI and immune activity was observed by the cleaning of excess blood products on H&E. Partially intact BBB tight junction appeared at the periphery of the histotripsy ablation zone. After day 7, the hyperintensity on T1-Gd decreased and further processing of blood products and wound-healing were observed. Correspondingly, the immunofluorescent staining for the claudin-5 and ZO-1indicated the BBB restoration in the periphery by day 21. The immune activities observed in this study requires further investigation via performing specific staining for macrophages, microglia, and astrocytes in the future.

In this study, we observed the lack of TJ protein expressions in the *center* of the histotripsy ablation, and reversible TJ protein damage at the *periphery* of ablation, indicating temporary BBB opening. At the *center* of the ablation zone, histotripsy generates very high mechanical strain and stress to disrupt the target tissue including the small vessels. We hypothesize that the mechanical stress induced by histotripsy-generated cavitation decreases with increasing distance away from the cavitation site [19,27]. The literature on BBB opening induced by microbubble and low-

pressure ultrasound pulses shows that the shear stress by stable cavitation in the vessel wall causes disassembly of TJ complex, leading to temporary BBB "opening" [6-7]. At the periphery of the histotripsy zone, the mechanical stress is lower, not enough to disrupt tissue, but may be sufficient to damage the TJ complex, which would explain the enhanced rim surrounding the histotripsy zone on T1-Gd MRI on day 0, followed by recovered TJ protein expressions. The mechanisms underlying histotripsy-induced BBB opening needs to be investigated.

Recovery of the claudin-5 and ZO-1 in histotripsy affected boundary indicated that the BBB opening is reversible in the periphery of histotripsy lesion. BBB tight junction started recovery around day 7 post-histotripsy and exhibited a similar appearance to healthy BBB tight junction by day 28. Leveraging this BBB opening effect, histotripsy may be combined with drug delivery for treatment of brain tumors, where histotripsy can be used to debulk the tumor core, and the BBBO induced by histotripsy can be used to enhance the drug delivery (e.g., chemotherapy or immunotherapy drugs) at the periphery of the ablation zone to treat any residual tumor cells. The understanding of the BBB recovery timeline post-histotripsy can be beneficial to guide the drug delivery protocol.

Another aspect to consider for histotripsy brain treatment is the impact of gliosis on the brain [28]. Gliosis is a central nervous system wound healing process in response to a trauma. According to the T1-Gd MRI hyperintensity and average ring width graph (Fig. 4.6 & 4.7), the intensity was stronger by 30% than the contralateral untreated side and the average ring width was non-zero (0.3mm) on day 28. This enhancement may be attributed to the absence of BBB in the center of ablation, but this impact may be lessened by the gliosis in the center of the lesion. Further investigation is needed on the extent to which gliosis impacts the BBB permeability of the center of the histotripsy region.

This study provides early evidence of reversible BBB opening at the periphery of the histotripsy ablation zone in the brain and temporal changes of the transient BBB opening. Further studies need to be conducted to characterize the size of particles that can penetrate through the BBB opening, the spatial extent of the BBB opening, and the time point at which the tight junction recovery starts at the periphery of histotripsy zone. These future studies will also inform the optimal timing for efficient drug delivery to the brain tissue along with the extent and duration of the BBBO.

4.5 Reference

[1] N. J. Abbott, A. A. K. Patabendige, D. E. M. Dolman, S. R. Yusof, and D. J. Begley, "Structure and function of the blood-brain barrier," *Neurobiol. Dis.*, vol. 37, no. 1, pp. 13–25, 2010, doi: 10.1016/j.nbd.2009.07.030.

[2] C. Greene, N. Hanley, and M. Campbell, "Claudin - 5 : gatekeeper of neurological function," *Fluids Barriers CNS*, pp. 1–15, 2019, doi: 10.1186/s12987-019-0123-z.

[3] W. M. Pardridge, "The blood-brain barrier: Bottleneck in brain drug development," *NeuroRx*, vol. 2, no. 1, pp. 3–14, 2005, doi: 10.1602/neurorx.2.1.3.

[4] X. Shang, P. Wang, Y. Liu, Z. Zhang, and Y. Xue, "Mechanism of low-frequency ultrasound in opening blood-tumor barrier by tight junction," *J. Mol. Neurosci.*, vol. 43, no. 3, pp. 364–369, 2011, doi: 10.1007/s12031-010-9451-9.

[5] S. Meairs and A. Alonso, "Ultrasound, microbubbles and the blood-brain barrier," *Prog. Biophys. Mol. Biol.*, vol. 93, no. 1–3, pp. 354–362, 2007, doi: 10.1016/j.pbiomolbio.2006.07.019.

[6] N. Hosseinkhah, D. Goertz, and K. Hynynen, "Microbubbles and Blood Brain Barrier Opening: A Numerical Study on Acoustic Emissions and Wall Stress Predictions," vol. 62, no. 5, pp. 1293–1304, 2015, doi: 10.1109/TBME.2014.2385651.Microbubbles.

[7] Z. Khodabakhshi, N. Hosseinkhah, and H. Ghadiri, "Pulsating Microbubble in a Micro-vessel and Mechanical Effect on Vessel Wall: A Simulation Study," *J Biomed Phy Eng*, vol. 11, no. 5, 2021, doi: 10.31661/jbpe.v0i0.1131.

[8] R. M. Nisbet, A. Van Der Jeugd, G. Leinenga, H. T. Evans, P. W. Janowicz, and J. Götz, "Combined effects of scanning ultrasound and a tau-specific single chain antibody

in a tau transgenic mouse model," *Brain*, vol. 140, no. 5, pp. 1220–1230, 2017, doi: 10.1093/brain/awx052.

[9] J. F. Jordão *et al.*, "Antibodies targeted to the brain with image-guided focused ultrasound reduces amyloid-β plaque load in the TgCRND8 mouse model of Alzheimer's disease," *PLoS One*, vol. 5, no. 5, pp. 4–11, 2010, doi: 10.1371/journal.pone.0010549.

[10] S. B. Raymond, L. H. Treat, J. D. Dewey, N. J. McDannold, K. Hynynen, and B. J. Bacskai, "Ultrasound enhanced delivery of molecular imaging and therapeutic agents in Alzheimer's disease mouse models," *PLoS One*, vol. 3, no. 5, pp. 1–7, 2008, doi: 10.1371/journal.pone.0002175.

[11] Maxson & Mitchell, "Multiple sessions of liposomal doxorubicin delivery via focused ultrasound mediated blood-brain barrier disruption: a safety study," *Physiol. Behav.*, vol. 176, no. 1, pp. 139–148, 2016, doi: 10.1016/j.physbeh.2017.03.040.

[12] N. Sheikov, N. Mcdannold, S. Sharma, and K. Hynynen, "Effect of focused ultrasound applied with an ultrasound contrast agent on the tight junctional integrity of the brain microvascular endothelium," *Ultrasound Med. Biol.*, vol. 34, no. 7, pp. 1093–1104, 2008.

[13] N. Vykhodtseva, V. Sorrentino, F. A. Jolesz, R. T. Bronson, and K. Hynynen, "MRI detection of the thermal effects of focused ultrasound on the brain," *Ultrasound Med. Biol.*, vol. 26, no. 5, pp. 871–880, 2000, doi: 10.1016/S0301-5629(00)00216-7.

[14] K. Kooiman *et al.*, "Focal areas of increased lipid concentration on the coating of microbubbles during short tone-burst ultrasound insonification," pp. 1–21, 2017.

[15] N. Asquier *et al.*, "Blood-brain barrier disruption in humans using an implantable ultrasound device: Quantification with MR images and correlation with local acoustic pressure," *J. Neurosurg.*, vol. 132, no. 3, pp. 875–883, 2020, doi: 10.3171/2018.9.JNS182001.

[16] N. Lipsman *et al.*, "Blood-brain barrier opening in Alzheimer's disease using MR-guided focused ultrasound," *Nat. Commun.*, vol. 9, no. 2336, 2018, doi: 10.1038/s41467-018-04529-6.

[17] Z. Xu *et al.*, "Controlled ultrasound tissue erosion.," *IEEE Trans. Ultrason. Ferroelectr. Freq. Control*, vol. 51, no. 6, pp. 726–736, 2004, doi: 10.1109/TUFFC.2004.1304271.

[18] J. E. Parsons, C. A. Cain, G. D. Abrams, and J. B. Fowlkes, "Pulsed cavitational ultrasound therapy for controlled tissue homogenization," *Ultrasound Med. Biol.*, 2006, doi: 10.1016/j.ultrasmedbio.2005.09.005.

[19] E. Vlaisavljevich, A. Maxwell, L. Mancia, E. Johnsen, C. Cain, and Z. Xu, "Visualizing the Histotripsy Process: Bubble Cloud–Cancer Cell Interactions in a Tissue-Mimicking

Environment," *Ultrasound Med. Biol.*, vol. 42, no. 10, pp. 2466–2477, Oct. 2016, doi: 10.1016/J.ULTRASMEDBIO.2016.05.018.

[20] N. Lu *et al.*, "Transcranial MR-guided Histotripsy System," *IEEE Trans. Ultrason. Ferroelectr. Freq. Control*, vol. 68, no. 9, pp. 2917–2929, 2021, doi: 10.1109/TUFFC.2021.3068113.

[21] S. W. Choi *et al.*, "Stereotactic Transcranial Focused Ultrasound Targeting System for Murine Brain Models," *IEEE Trans. Ultrason. Ferroelectr. Freq. Control*, vol. 68, no. 1, pp. 154–163, 2021, doi: 10.1109/TUFFC.2020.3012303.

[22] R. Singh, A. J. Putnam, B. Fowlkes, E. Johnsen, and C. Cain, "Histotripsy Intrinsic Threshold for Cavitation," vol. 41, no. 6, pp. 1651–1667, 2016, doi: 10.1016/j.ultrasmedbio.2015.01.028.Effects.

[23] F. Vignon *et al.*, "Microbubble cavitation imaging," *IEEE Trans. Ultrason. Ferroelectr. Freq. Control*, vol. 60, no. 4, pp. 661–670, 2013, doi: 10.1109/TUFFC.2013.2615.

[24] J. J. Choi, S. Wang, Y. S. Tung, B. Morrison, and E. E. Konofagou, "Molecules of Various Pharmacologically-Relevant Sizes Can Cross the Ultrasound-Induced Blood-Brain Barrier Opening in vivo," *Ultrasound Med. Biol.*, vol. 36, no. 1, pp. 58–67, 2010, doi: 10.1016/j.ultrasmedbio.2009.08.006.

[25] I. M. Noebauer-Huhmann, P. Szomolanyi, V. Juras, O. Kraff, M. E. Ladd, and S. Trattnig, "Gadolinium-based magnetic resonance contrast agents at 7 tesla: In vitro T1 relaxivities in human blood plasma," *Invest. Radiol.*, vol. 45, no. 9, pp. 554–558, 2010, doi: 10.1097/RLI.0b013e3181ebd4e3.

[26] PubChem, "Gadoteridol," *Natl. Cent. Biotechnol. Information, PubChem Compd. Summ. CID 60714*, 2005.

[27] L. Mancia, M. Rodriguez, J. R. Sukovich, Z. Xu, and E. Johnsen, "Single – bubble dynamics in histotripsy and high – amplitude ultrasound : Modeling and validation," *Phys. Med. Biol.*, vol. 65, 2020.

[28] R. Cabezas *et al.*, "Astrocytic modulation of blood brain barrier: Perspectives on Parkinson's disease," *Front. Cell. Neurosci.*, vol. 8, no. AUG, pp. 1–11, 2014, doi: 10.3389/fncel.2014.00211.

Chapter 5 Neuronavigation-guided Transcranial Histotripsy (NaviTH) System

5.1 Introduction

Transcranial magnetic resonance-guided focused ultrasound (tcMRgFUS) thermal ablation has been approved by FDA to treat brain tumors, essential tremors, and Parkinson's Disease associated with tremors [1-6]. Image guidance during the tcMRgFUS procedure is achieved via real-time MR thermometry and allows visualization of the focal ablation spot [7]. However, MR guidance requires a long scanner time in the MR bore, is expensive, and limits clinical operational space to the bore of the magnet. Low amplitude tcMRgFUS for blood-brain barrier (BBB) opening has been performed to deliver therapeutic agents to the target tissue [8]. There are numerous tcMRgFUS BBB opening trials ongoing for the treatment of brain tumors (NCT03739905, NCT03321487, NCT04370665, NCT05565443). To step away from MR guidance due to difficulty in clinical adoption and expensive cost, neuronavigation-guided transcranial focused ultrasound (NaviFUS) for BBB opening has been shown to demonstrate high targeting accuracy of 2~4mm [9-10]. Ongoing clinical trials with this system are currently in progress for glioblastoma (GBM) (NCT03626896) and epilepsy applications (NCT03860298).

Transcranial histotripsy focuses microsecond-length, high-pressure ultrasound pulses to mechanically fractionate brain tissues via cavitation [11-12]. Histotripsy cavitation cloud has been shown to homogenize the tissue in the focal region into acellular homogenates, and the high strain and stress from cavitation expansion and collapse mechanically disrupt the cells in the focal region

[13]. Transcranial histotripsy has shown great promise as a neurosurgical tool by demonstrating minimal heating of the skull (<4^{o}C) while effectively fractionating the target brain tissue volume [14] and by demonstrating safety through brain volumetric treatments in the *in vivo* mouse brain tumor model and *in vivo* porcine normal brain through an excised human skull [15-17]. The cavitation cloud emits acoustic shockwaves that can be captured with our transmit-receive capable histotripsy array. Sukovich et al have demonstrated the real-time cavitation localization capability of the transcranial histotripsy array through an excised human skull [18], which provides a real-time cavitation and treatment monitoring tool for transcranial histotripsy.

Transcranial MR-guided histotripsy (tcMRgHt) has been also developed [16] and shown its capability in the *in vivo* porcine brain through an excised human skull. tcMRgHt poses the same disadvantages as it does on tcMRgFUS due to the high cost and the long MRI scanner time required, spatial restriction for the clinicians, and the requirement of MR-compatible equipment. On the other hand, neuronavigation is less costly than MR guidance, is compatible with existing surgical tools, and has been the hallmark guidance tool for neurosurgery for the past three decades [19].

Therefore, in this study, we integrate the neuronavigation-guidance system with transcranial histotripsy to develop a neuronavigation-guided transcranial histotripsy (NaviTH) system and associated workflow. First, we introduce A) components of the NaviTH system, B) the workflow for transcranial treatment using the NaviTH system, C) the setup and methods to evaluate the targeting error using the NaviTH system, which was divided into 1) target registration error (TRE)) and 2) focal shift due to skull aberration after aberration correction. Lastly, the feasibility and targeting accuracy of the NaviTH system was investigated in whole-body human

cadavers and excised human skulls. To the author's knowledge, this is the first study that integrates the neuronavigation system with transcranial histotripsy.

5.2 Materials and Methods

5.2.1 Components of Neuronavigation-guided Transcranial Histotripsy (NaviTH) System

There are three main hardware components to the NaviTH system (Fig. 5.1A): the histotripsy array, the neuronavigation system, and the transducer tracking instrument (TTI). The other supporting components are the coordinate reference frame (CRF), the co-registration wand, the stereotactic frame, the water coupling system to ensure ultrasound transmission from the histotripsy array to the skull, and a 3D positioning system attached to the water coupling system to move the histotripsy array.

Transcranial histotripsy array with transmit-receive capabilities

A transmit-receive capable, 360-element, 700 kHz hemispherical array with a focal distance of 150mm was used for both cadaver and skull experiments (Fig. 5.1B). Prior to the experiments, a pin hydrophone (CA-1135, Dynasen Inc., Goleta, CA, USA) was placed at the CAD geometric focus of the transducer to correct the deformation of the transducer scaffold.

Neuronavigation system, Co-registration wand, and CRF

StealthStation™ S7 surgical navigation system (Medtronic, Dublin, Ireland) was used for image guidance of transcranial histotripsy. The navigation system co-registers the location of the histotripsy array focus to the patient's skull based on a custom TTI attached to the histotripsy transducer and the CRF attached to the patient's head. Using the CRF attached to the stereotactic frame fixed to the patient's head, the neuronavigation system visualizes the 3D locations of the

head with the optical positioning system (OPS). Using a custom TTI attached to the histotripsy transducer, the neuronavigation system projects the 3D location of the histotripsy array focus. Then the neuronavigation system visualizes both the CRF and TTI, co-registers the location of the histotripsy array focus to the cadaver head, overlays the histotripsy focus onto pre-treatment MRI/CT brain scans of the cadaver, and track any movement of the histotripsy focal location respective to the brain scans.

Transducer Tracking Instrument (TTI)

To allow neuronavigation optical tracking of the histotripsy array geometric focus, a custom TTI was designed, fabricated, and attached to the transcranial histotripsy array. The TTI was equipped with retroreflective spheres (RRSs), and the unique geometry of the RRSs was recognized by the neuronavigation OPS. Then a tip/target was projected from the RRSs to the geometric focus of the array, which allows the neuronavigation system to co-register the histotripsy focal location.

Water Coupling Tank, Stereotactic Frame, and 3D positioning system

A custom water coupling tank (TTP, Hertfordshire, United Kingdom) containing a stereotactic frame to rigidly immobilize the patient head and hold the CRF, and a 3D positioning system to translate the histotripsy array, was designed and fabricated for the cadaveric experiments. The CRF was attached to the stereotactic frame, and the frame contained four screws for rigidly holding the cadaver head and an attachment slot at the bottom of the frame for connection to the water coupling tank.

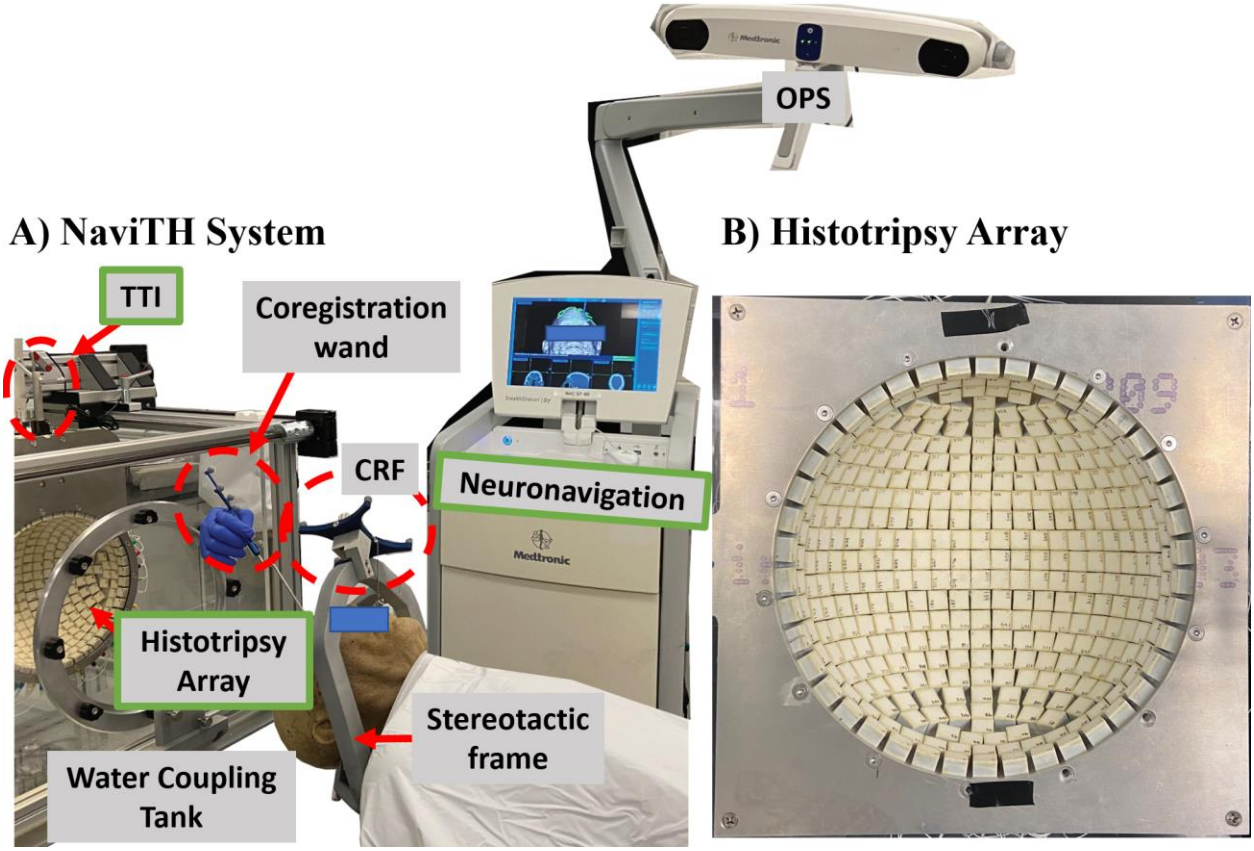

Figure 5.1. Neuronavigation-guided Transcranial Histotripsy (NaviTH) system. The NaviTH system (A) mainly consists of a neuronavigation system, a histotripsy array, and a transducer tracking instrument (TTI) fixed to the histotripsy array. The neuronavigation system has an optical positioning system (OPS) for the optical tracking of instruments such as the coordinate reference frame (CRF), a co-registration wand, and the TTI. The CRF is fixed to the stereotactic frame attached to the patient's head, the co-registration wand is used to map the patient CT/MRI to the CRF, and the TTI maps the focus of the histotripsy array. The water coupling tank contains the histotripsy array and TTI to ensure ultrasound transmission from the histotripsy array (B) to the patient's head.

5.2.2 Workflow

In this study, the feasibility and target accuracy of the NaviTH system was investigated using two <96 hours post-mortem, whole-body cadavers and two excised human skullcaps obtained from the Anatomical Donations Program (Michigan Medicine, University of Michigan, Ann Arbor, USA). Therefore, the workflow steps are described with reference to the cadaver head or the skull.

1. **TTI & Pre-treatment MRI and CT scans** – Before the treatment, the skull was scanned with CT, or the cadaver head was scanned with CT or MRI. Pre-treatment MRI and CT of the skull or the cadaver head and geometry file for the transducer tracking instruments (TTI) are uploaded to the neuronavigation system. TTI is recognized by the neuronavigation system OPS and maps the location of the histotripsy transducer focus. MRI scans are used to image the brain structures, and CT scans are used to analyze the skull thickness and surface geometry for aberration correction.
2. **Co-registration via neuronavigation -** The head is immobilized by a stereotactic frame with four screws and the CRF was rigidly mounted on the stereotactic frame. Neuronavigation is used to co-register the head surface locations to the histotripsy array focal location based on the CRF fixed to the stereotactic frame that is attached to the head, and the TTI that is rigidly attached to the transcranial histotripsy array.
3. **Patient position** - After co-registration, the patient or the skulls are positioned inside the histotripsy transducer. Guided by a pre-treatment CT & MRI head scan co-registered via neuronavigation, the geometric focus of the histotripsy array is placed inside the target brain volume by mechanically moving the array with a 3D positioning system.
4. **Aberration Correction (AC) -** Once the position of the histotripsy focus is set to the desired location in the brain, a neuronavigation-to-Kranion (N2K) transformation matrix containing the location of the patient CT relative to the transducer focus is transferred to Kranion, a software used for CT-based analytical AC [21] The 2-step aberration correction is then used for AC, where CT-based analytic AC is first performed via Kranion followed by cavitation-based AC [22]. The Kranion-based AC was used to correct for the focal shift resulting from the skull aberration and some pressure recovery to create an initial cavitation

cloud, and cavitation-based AC was performed to regain most of the pressure lost through aberration. With AC, the histotripsy focus is placed within the target, and an electronic focal steering grid pattern is created to cover the target volume.

5. **Treatment delivery** – The treatment is delivered by covering the target volume with electronic focal steering. During the treatment, the transmit-receive capable histotripsy array is used to collect and record acoustic cavitation emission signals to form cavitation mapping [18] that can overlay the pre-treatment MRI brain scans to provide treatment monitoring.
6. **Post-Treatment evaluation** – Post treatment, the cadaver head is scanned by MRI to identify histotripsy ablation and compared to the pre-planned target volume for treatment accuracy evaluation.

Step 1: TTI & Pre-operation MRI and CT scans

Before the treatment, MRI and CT were uploaded into the neuronavigation system, along with a transducer tracking instrument (TTI) geometry file. The TTI geometry file included detailed information regarding the locations of the retroreflective spheres (RRSs). The RRSs pattern was recognized by the optical positioning system (OPS) to project a tip or target (i.e. histotripsy transducer focus in this case) of the instrument. The design of the TTI is critical to minimize TRE, and critical design considerations are the distance from the RRSs to the tip, the rigidity of the instrument, and the RRSs' positions relative to the "target".

Before the treatment, the skull was scanned with CT, or the cadaver head was scanned with CT or MRI. CT scans for both cadaver and skull studies were obtained for aberration correction using Discovery CT750 HD (GE Medical Systems, Chicago, IL, USA) with the following imaging sequence: Stealth Protocol with reconstruction, 0.625mm isotropic resolution. The MRI scans

were acquired using a 3T MRI scanner (Ingenia, Philips, Amsterdam, Netherland) with the following imaging sequences (Sagittal 3D accelerated MPRAGE, 3D Axial T1, FFE 8ech ax, AX DWI_s3, dADC, eADC, T2 AX TSE SENSE, PADRE_T1FFE, T2_FFE_TRA, FLAIR_TRA_2MM). 3D Axial T1 (0.49mm x 0.49mm x 1mm resolution) was used to co-register with the CT images to identify the anatomical structures for targeting.

Step 2: Co-registration via neuronavigation

Co-registration of the cadaver CT/MRI image and histotripsy array via TTI was achieved by the neuronavigation system. The cadaver head was rigidly fixed using the stereotactic frame which held the CRF. The four screws on the stereotactic frame were tightened to lock the cadaver head in the frame. A "planar blunt tool" or co-registration wand from StealthStation was used to co-register the cadaver head or the skull to pre-treatment MRI/CT head/skull scans by tracing the contour of the head. The resulting contour mapping of the head was co-registered to the CRF, finishing the co-registration step. This co-registration wand is a calibrated tool provided with the navigation system. For the skull study, the wand was used to register skull CT to the physical skull, which was mapped to the CRF. CRF was rigidly mounted to an acrylic plate that held the skull. Once the medical images have been mapped, any disturbance to the location of the reference frame or the skull/patient necessitated a re-coregistration process to ensure that the co-registration between the skull and the CRF was correct.

Step 3: Patient Position

For the cadaver study, the patients were co-registered in prone positions, a water-tight rubber membrane was donned on the head, and the head was positioned inside the water coupling tank which contained the histotripsy array (Fig. 5.1B). Next, the stereotactic frame was screwed down to the water coupling tank. The tank was filled with degassed water, and the TTI-equipped

histotripsy array, attached to a 3D positioning system, was moved to place the histotripsy array focus on the target location in the brain. For the skull study, the skulls were positioned inside the histotripsy array after co-registration.

Step 4: Aberration Correction (AC)

Once the patient/skull has been positioned inside the histotripsy transducer, the two-step correction method described by Lu et al. [22] was performed to correct the aberration through the skull. First, the location of the histotripsy focus respective to the patient/skull CT from the neuronavigation system was sent to Kranion. Kranion was used to perform the CT-based analytic AC, to counter the impact of focal location shift that arose from the aberration and to regain back some pressure that was lost due to aberration. This neuronavigation-to-Kranion transformation (N2K) matrix calculation is shown in **appendix**.

Kranion is an open-source software for CT-based AC of focused ultrasound therapy that uses ray tracing. For this paper, we assumed a constant speed of sound (2300m/s) in the skull for CT-based AC as done in previous work [22]. The workflow of Kranion includes 1) uploading the *same* CT series used for the neuronavigation system, 2) uploading the histotripsy transducer geometry, 3) applying the N2K matrix containing the location of the focus relative to the CT of the skull, and 4) calculate CT-based AC time delays for correction. The N2K transformation was iterated until the histotripsy array foci depicted by both the neuronavigation system and Kranion were identical.

Following the CT-based aberration correction from Kranion, a cavitation cloud was generated through the skull by gradually increasing the input power until cavitation generation, and the resulting acoustic emission signals from the cavitation cloud were acquired with the transmit-receive capable histotripsy array. The emission signals were processed to perform

cavitation-based AC, which has been shown to regain >90% of pressure lost through aberration [22].

Step 5: Treatment Delivery

After the two-step aberration correction, for the cadaver study, histotripsy treatment was delivered to a hexagonally close-packed (hcp) lattice (dx,dy,dz =1.1mm) of 1 cm^3 volume using electronical focal steering at 200Hz pulse repetition frequency (PRF) with 50 pulses per location. For the skull study, histotripsy was delivered to generate cavitation in 3x3x3 = 27 locations (X,Y,Z = [-5, 0, 5] mm) using electronical focal steering at 5Hz PRF with 10 pulses per location. The cavitation locations for the skull study were chosen to mimic the extremities of the $1cm^3$ volume treatment used for the cadaver study. FOPH (HFO 690, Onda, Sunnyvale, CA, USA) was used to estimate the pressure levels used for the skull experiment. The electronics voltage level used to drive the histotripsy array elements for both the cadaver and skull experiments were identical, and therefore the pressure generated in the cadaver study was assumed to be similar to those of the skull study. The skulls were translated and rotated to mimic various positions possible during treatment, and the P_- with skulls varied between 39 to 61 MPa depending on the locations of the skulls in the histotripsy array.

Step 5: Post-treatment Evaluation

After treatment, for the cadaver study, the water coupling tank was drained, and the rubber membrane and the stereotactic frame were taken off to transport the cadaver to an MRI suite. MRI head scans were collected to evaluate the ablation generated by histotripsy using the same 3T MRI scanner with the same imaging sequences as the pre-treatment MRI.

5.3 System Error Evaluation

The targeting accuracy of the NaviTH system was tested in two human cadavers and two excised human skulls, which were obtained via the Anatomic Donation Program at the University of Michigan. **Table 5.1** lists the average and standard deviation of skull thickness in millimeters of each specimen and the skull density ratio (SDR) calculated by Kranion. Each step of the workflow for this study is detailed below.

Table 5.1. Cadaver and Skull Information: skull density ratio (SDR) and thickness

Specimen	Average SDR	Average Skull Thickness
Cadaver 1	0.72 ± 0.16	7.02 ± 2.03 mm
Cadaver 2	0.69 ± 0.18	7.24 ± 5.43 mm
Skull 1	0.44 ± 0.10	6.27 ± 1.98 mm
Skull 2	0.59 ± 0.11	7.19 ± 2.28 mm

The sources of targeting error of the NaviTH system are largely divided into two: 1) co-registration and 2) focal shifts induced by the skull aberration, and the corresponding errors arising from each are referred to as target registration error (TRE) and focal shift, respectively. The errors are assumed to have unbiased, random distributions. The feasibility of the initial NaviTH system was tested in two human cadavers, and the overall targeting error was calculated (section 5.3.1). For the cadaver study, the TRE and the focal shift could not be separately evaluated. The overall targeting error of the initial NaviTH system was found to be large from the cadaver study due to the TTI. Therefore, an improved TTI was built. The TRE and focal shift of the old and new NaviTH systems were measured separately using the excised human skulls via methods described in the

following sections (5.3.2-5.3.3). It should be noted that the focal shift here refers to the difference between the geometric focus of the histotripsy array and the actual treatment location after aberration correction (AC) through the skull. The overall targeting error of the new NaviTH system was finally evaluated in a tissue-mimicking phantom through the excised human skull (section 3.4).

5.3.1 Human Cadaver study

The two human cadaver experiments were performed in the brain of a full human cadaver obtained. Unfortunately, we had difficulty obtaining more cadavers since 2021 due to the impact of COVID. Thus, no new experiments could be carried out to test the targeting accuracy of the newly calibrated NaviTH system. The workflow of treating the human cadaver will follow the previous section. The targeting error was calculated as the distance between the center location of the intended and actual treatment volumes. The intended treatment volume was outlined on the pre-treatment MRI scan. The actual treatment volume was measured as the hypointense zone on the post-treatment T1-weighted MRI scan. The pre- and post-treatment MRI scans of the cadaver brain were co-registered via the Neuronavigation system, and the distance between the center location of the intended treatment volume based on the pre-treatment scan and the center location of the actual treatment volume on the post-treatment scan is measured.

5.3.2 Skull Study

After the cadaver study, the two ex vivo human skull experiments were conducted with the skulls obtained. The skulls were used to evaluate the TRE and the focal shift induced by skull aberration.

TRE Evaluation

One major source of targeting error for NaviTH is the position registration error from the histotripsy array to the geometric focus of the array (i.e. target) through the skull based on the TTI and the neuronavigation system, i.e., targeting registration error (TRE). Thus, the TTI has a major impact on the TRE.

Transducer Tracking Instrument (TTI)

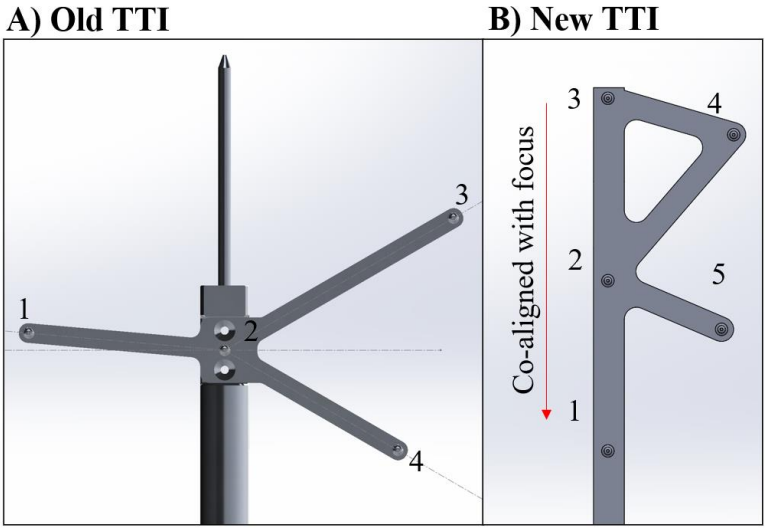

Figure 5.2. The old (left) and new (right) transducer tracking instruments (TTI). The numbers on the images denote the locations of the retroreflective spheres (RRSs) in the instruments. The geometry of the RRSs is tracked by the optical positioning system (OPS) and a target or the histotripsy focus is projected from the RRS pattern.

The transducer tracking instruments (TTI) were equipped with retroreflective spheres (RRSs) for the neuronavigation system to optically track the geometric pattern of the spheres to calculate in space where the target of the instrument was projected. The Polaris camera (Northern Digital, Inc, Waterloo, Ontario, Canada) is used for capturing the optical images of the TTI. A good TTI should be asymmetric, the average distance from the RRSs to the target is short, and the intra-sphere distances are large [23]. We constructed two TTIs (Fig. 5.2) and found that the TTI features (e.g., RRS locations respective to the target, the distance of the RRSs to the target, and intra-RRS distances) have an impact on the TRE. The features defining the old TTI were:

- 4 RRSs, spheres arbitrarily placed relative to the transducer geometric focus
- Average intra-RRS distance: ~50mm
- Average distance from the TTI RRSs to the target: 333mm

The defining features of the new TTI are:

- 5 RRSs, where the 3 of them are co-aligned with the geometric focus of the transducer, and all in the same plane as the focus
- Average intra-RRS distance: ~55mm
- Average distance from the TTI RRSs to the target: 370mm

For perspective, NaviFUS's average distance from the RRSs to the array focus is approximately 150mm [24]. The large average distances from the RRSs on the target of our TTI designs were due to the constraints with the water coupling system (Fig. 5.3A**)**. The histotripsy transducer is submerged in a water tank and the TTI and CRF both need to be outside the water tank to be visible to the neuronavigation OPS for accurate tracking. Even though the new TTI (Fig. 5.2B) had an average distance to the TTI RRSs and intra-RRS distance similar to the old TTI (Fig. 5.2A), the placement of the RRSs all in the same plane as the focus significantly reduced the TRE.

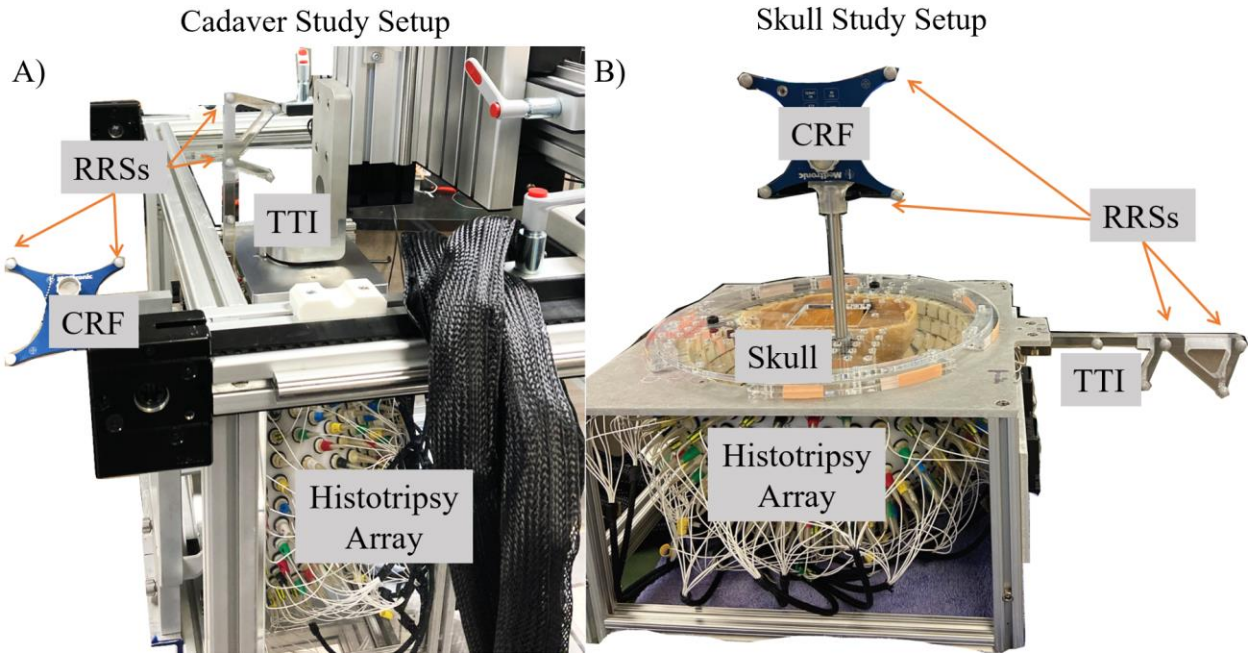

Figure 5.3. Cadaver (A) and skull (B) experiment setup. (A) The histotripsy transducer was placed inside a large acrylic water tank. Outside the water tank were the TTI and CRF with their RRSs facing the same direction for the OPS to visualize both instruments clearly for accurate tracking of instruments. The 3D positioning system allowed translation of the histotripsy transducer respective to the patient's head. The stereotactic frame equipped with CRF rigidly immobilized the head of the patient. **(B)** The skull study TRE evaluation setup has a similar configuration where the CRF is attached to the co-registered skull and the skull is mechanically co-registered to the histotripsy transducer via a laser-cut, acrylic plate. The histotripsy transducer is equipped with the TTI to allow tracking of the geometric focus relative to the skull. TTI stands for transducer tracking instrument, CRF for the coordinate reference frame, RRS for the retroreflective sphere, OPS for the optical positioning system of the neuronavigation system, and TRE for target registration error.

TRE Evaluation Setup

The TRE was evaluated using two excised human skulls. To evaluate the TRE, a focus structure (Fig. 5.4A & B) was designed (SolidWorks, Dassault Systemes, Velizy-Villacoublay, France) and 3D-printed (J750, Stratasys, Rehovot, Israel). The focus structure was connected to a laser-cut, ¼" acrylic plate rigidly attached to the histotripsy array front plate (Fig. 5.4C) and contained a point center that represents the geometric focus of the array (Fig. 5.4B). The CAD focus (i.e. the point center) represented the *true geometric focal location.* The acrylic plate

connected the skull, focus structure, and the array scaffold to achieve mechanical co-registration (Fig. 5.4C), informing the location of the array focus. The CT of the skull with the acrylic plate and the focus structure was acquired to enable co-registration via the neuronavigation system. After co-registration, the acrylic plate was rigidly mounted on the array scaffold via thumb screws. The transformation matrix regarding the histotripsy array and the skull CT was sent from the neuronavigation system to Kranion for aberration correction, and the Kranion scene was exported to 3D Slicer (Fig. 5.4D) for TRE measurement. The Kranion scene contained the locations of the histotripsy array elements, and the histotripsy array focus respective to the CT of the skull and the focal structure.

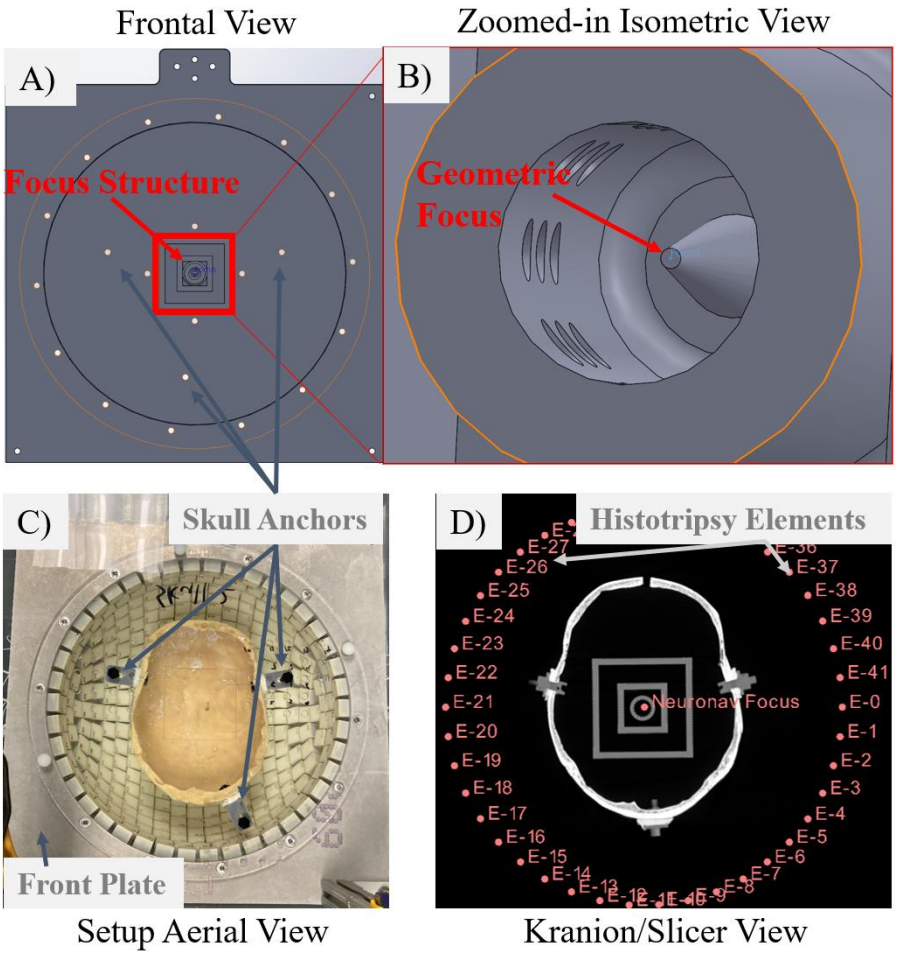

Figure 5.4. TRE evaluation setup. A focus structure (A & B) and a skull-holding acrylic plate were designed in SolidWorks and were 3D printed, and laser-cut, respectively. (A) and (B) provide a detailed view of the focus structure, and the setup view (C) provides how the setup can be positioned respective to the transducer front plate. The skull contained three L-brackets that allowed attachment to the acrylic plate and the acrylic plate connected to the histotripsy transducer front plate for mechanical co-registration. The skull anchors refer to the holes in the acrylic plate that attaches to the L-brackets of the skull. The Kranion/Slicer view (D) superimposes the co-registered element positions, the co-registered target (i.e. neuronavigation focus), and the CT of the skull and focus structure. The 'neuronavigation focus' depicted in (D) is the co-registered histotripsy focus from the TTI. Histotripsy array elements are denoted with E-#, where # is the number of the element.

The laser-cutter (VLS 6.60 laser systems, Universal Laser Systems, Inc. Scottsdale, AZ, USA) and the 3D printer were used to manufacture these parts, and the tolerances put into the design of parts for both laser cutting and 3D printing were 0.254mm (0.01").

TRE Measurement

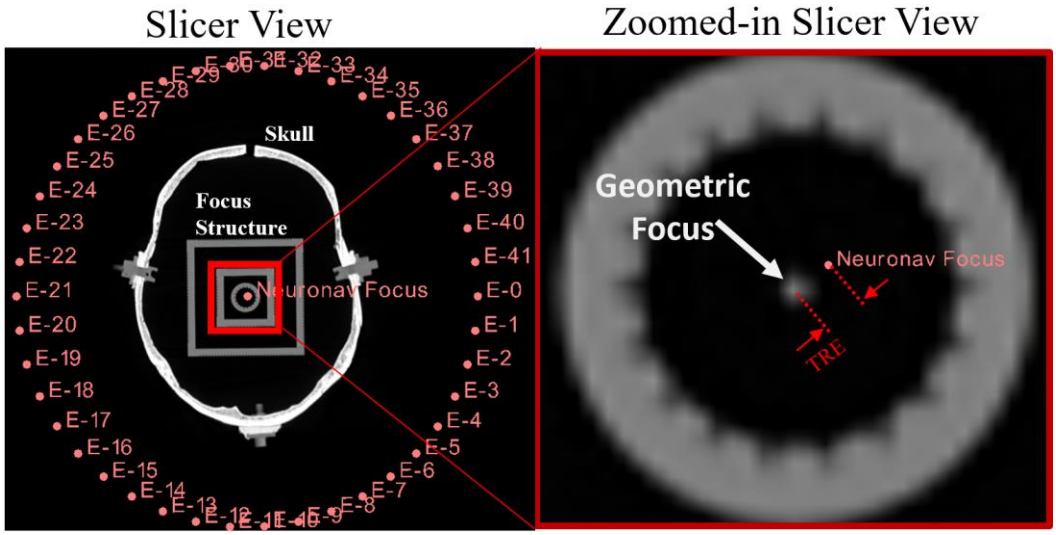

Figure 5.5. Calculating the TRE. The Kranion scene, which includes the skull and focus structure CT, transducer element locations, and the transducer focus (i.e. neuronavigation focus), is exported into Slicer, and the TRE is calculated from the focus structure central point, (i.e. geometric focus or the true target) to the 'neuronavigation focus'.

After the N2K transformation matrix is applied to Kranion, the Kranion scene is exported to 3D Slicer (open source, slicer.org) by the Kranion built-in function. In Slicer, the distance

between the focal location determined by neuronavigation and the actual location of the focus structure (i.e. true *target/focus*) (Fig. 5.5) is measured to calculate the overall TRE.

5.3.3 Focal Shift Evaluation setup

For the second part of the skull study, the focal shift between the geometric focus of the histotripsy array and true treatment location was measured after the two-step AC is performed. Even with AC, the array foal location can be slightly shifted from the geometric focus due to the aberration effect from the skull. The positions of the skull respective to the histotripsy array were varied to simulate patient positioning as well as different location treatments.

For the focal shift evaluation setup, a 1/4in-thick acrylic plate containing 0.75in-spaced 3x3 grid holes was laser-cut to achieve lateral translation and rotation around the cranial axis of the skull to simulate patient positioning. The front plate attachment holes allowed rigid mechanical co-registration of the acrylic plate to the array scaffold. Additional acrylic spacers were cut to simulate rigid 0.5in axial translation of the array.

0.75in of rigid translations (xy) along the plane of the acrylic plate, cranial-axis counter, and clockwise rotations of 360/14 = 25.7 degrees, and 0.5in of rigid elevation (z) were varied in combination to produce approximately 36 different positions (9, 0.75in spaced holes; 3 rotation positions: counter-clockwise, clockwise and original upright position; 1, 0.5in an elevated position). The histotripsy array front plate contained 14 holes (Fig. 5.4C) to allow rotation in the cranial axis. At each position, the N2K transformation matrix was saved, and the CT-based and cavitation-based AC (2-step AC) were obtained before treatment.

5.3.4 Focal Shift Measurement

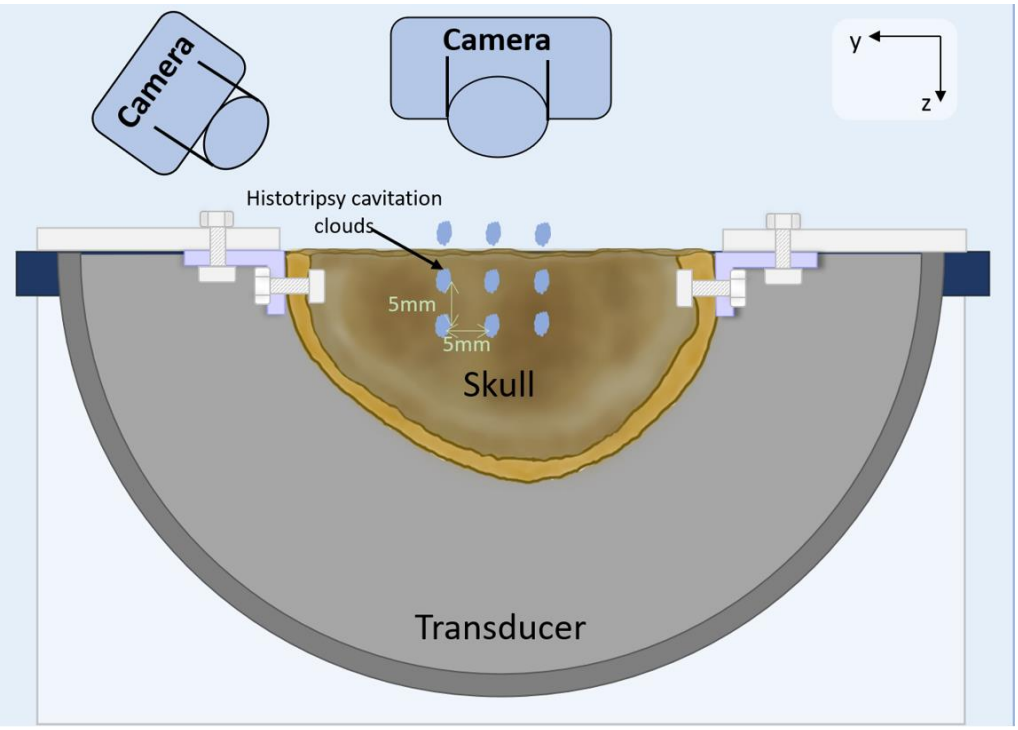

Figure 5.6. Focal shift evaluation setup. Two cameras were set up orthogonally to each other to extract bubble cloud locations. After two-step aberration correction, histotripsy cavitation clouds were formed via electronic focal steering at 27 different locations, where the locations were spaced out by 5mm.

To calculate the focal shift through the skull, a cavitation cloud was generated through the skull and imaged by two cameras (Chameleon and Flea, Point Grey, FLIR, Wilsonville, OR, USA) placed orthogonally to each other above the skull and the histotripsy array, facing the focal region of the transducer (Fig. 5.6). Histotripsy cavitation clouds were generated in the aforementioned pattern at the 27 locations. Camera images were acquired with and without the skulls (i.e. in free-field). The distances between the cavitation locations through the skulls and the freefield cavitation locations were calculated to evaluate the focal shift. This process was repeated 36 different times for the various skull positions.

5.3.5 Overall Targeting Error

The overall system error is defined as the discrepancy between the intended target (i.e. neuronavigation focus) and the resulting ablation location. For the skull study, a red blood cell (RBC) gel phantom was used to evaluate the post-calibration system targeting accuracy. An RBC phantom holder designed to place the RBC phantom at the CAD geometric focus (i.e. true focus) of the histotripsy array was 3D-printed (J750, Stratasys, Rehovot, Israel). The RBC phantom was made and placed at the center of the laser-cut acrylic plate. The same acrylic plate held the skull and connected the skull and the phantom to the transducer front plate, achieving mechanical coregistration as mentioned in section 3.2.3 and shown in Figure 5.7. The width and the height of the cylindrical phantom were 16mm and 25mm, respectively. The RBC phantom holder contained fiducial structures to allow localization of the histotripsy ablation point respective to the geometric focus of the array.

The workflow for the RBC phantom treatment was similar to the cadaver workflow presented in section 2: 1) pre-treatment MRI of the RBC gel phantom, 2) co-registration of the skull, 3) skull placement in the array, 4) two-step aberration correction, 5) placement of the phantom inside the skull and treatment delivery, and 6) post-treatment MRI of the RBC phantom.

The RBC phantoms (N=7) were made as previously done to visualize histotripsy damage [17,29-30]. 1.5% agarose gel was prepared by mixing degassed saline and agarose powder (DSA20070, Dot Scientific, Burton, MI, USA). The formed gel was mixed with bovine blood (Dunbar Meats, Milan, MI, USA) and poured into the RBC phantom holder to solidify.

1) The phantom was imaged with a 7T MRI scanner (Varian, Inc., Palo Alto, CA, USA) using a T2-weighted fast spin-echo sequence (FOV = 25 x 25 x 30 mm^3, resolution = 0.2 x 0.2 x 1 mm, TR = 3.8s, ESP=15ms, Kzero =3 (TE = 45ms)) at axial, coronal, and

sagittal orientations to locate the fiducial structures in the phantom and therefore, localize the geometric focus of the array.

2) The skull CT containing the focus structure and the acrylic plate was co-registered by the neuronavigation system.
3) The skull was placed in the array. Once both the TTI and skull were in the neuronavigation field of view, the intended focus (i.e. neuronavigation target) was visible respective to the focus point of the focal structure.
4) Two-step aberration correction was acquired.
5) The RBC phantom was placed inside the skull (Fig. 5.7A) and the treatment was delivered (single point ablation, 200pulses, 5Hz pulse repetition frequency). Single-point ablation was chosen to easily distinguish the center of the histotripsy ablation.
6) Post-treatment MRI was acquired. The accuracy of the system targeting was evaluated by overlaying the intended focus over the post-treatment MRI and comparing the center of the histotripsy ablated target to the intended target (Fig. 5.7B). A total of seven locations was randomly chosen from the 36 locations mentioned in section 3.3 to simulate treating different regions within the head of a patient.

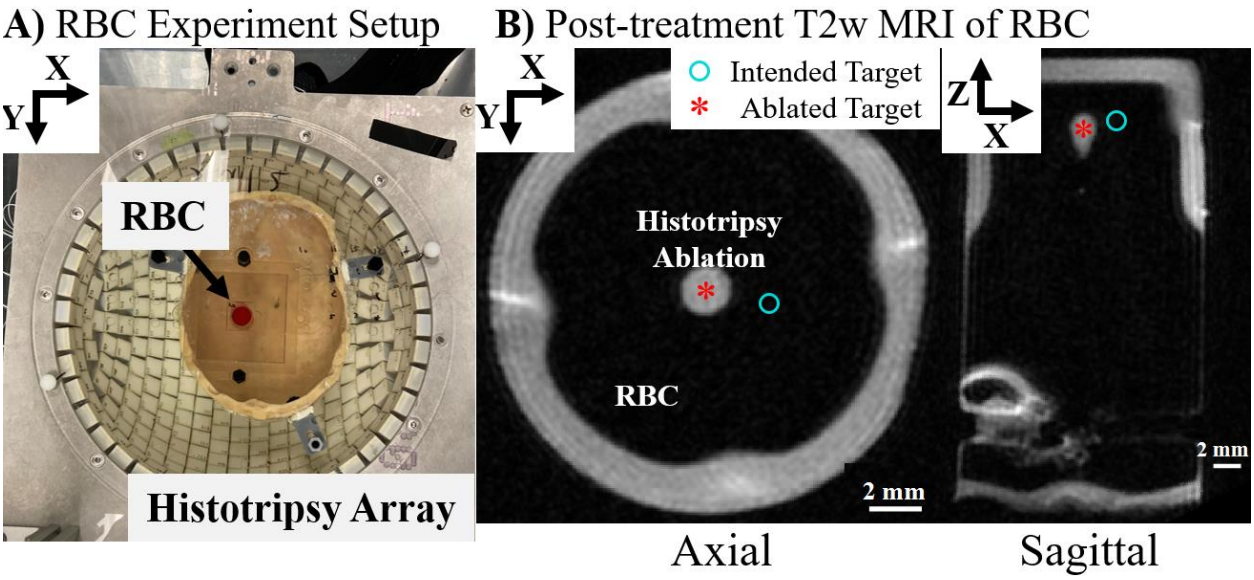

Figure 5.7. System targeting error evaluation setup by red blood cell (RBC) phantom. The experimental setup for system error is shown in (A). The RBC phantom is placed at the geometric focus of the histotripsy array and within the ex vivo skull cap. The system targeting error was calculated by (B) comparing the intended target (i.e. neuronavigation target) and the center of the histotripsy ablation point in the post-treatment MRI.

5.4 Results

5.4.1 Cadaver Experiment

The feasibility of the NaviTH system has been demonstrated in two human cadavers <96 hours post-mortem. Three ablations of 1cm^3 were created in three different locations (corpus callosum, septum pellucidum, and thalamus) in the brain of two whole-body human cadavers. The ablation zones were identified by post-treatment MRI (Fig. 5.7). The shape and size of the ablation zones matched well with those of the intended treatment volume. 3D Axial T1 MRI best depicted the lesions created near or in the ventricle (Fig. 5.7A & B) due to its high resolution. Apparent diffusion coefficient (ADC) MRI images best depicted the histotripsy lesion in the brain parenchyma (Fig. 7C). These two experiments were conducted in 2020. However, after these experiments, we were not able to obtain additional cadavers due to the lack of cadaver ability caused by COVID.

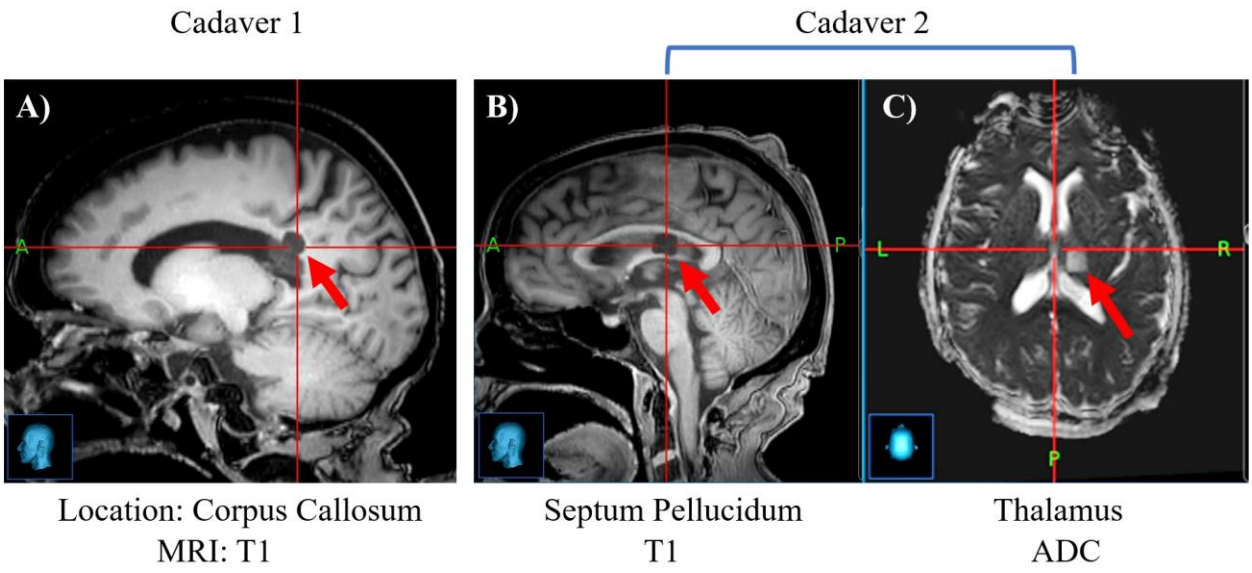

Figure 5.8. NaviTH cadaver experiments post-treatment MRI. MRI images best representing the lesions created in the cadavers are shown. A) presents the corpus callosum treatment of cadaver 1 and the corresponding post-treatment T1 MRI. For cadaver 2, two 1cm3 lesions, one in the septum pellucidum and another in the thalamus, were generated (B & C). B) is a post-treatment T1 MRI of the septum pellucidum lesion and C) is the post-treatment apparent diffusion coefficient (ADC) MRI image of the thalamic lesion created in cadaver 2. The red arrows point out the volume ablation created with NaviTH.

The overall targeting (TRE + focal shift) error for the two cadavers with the uncalibrated system is presented (Table 5.2) and the corresponding pre- and post-treatment MRI from the corpus callosum experiment are shown in Figure 5.8. A $1cm^3$ lesion was created using NaviTH and the targeting error ranged between 3.4-9mm with an average error of 5.6mm. We attribute the sources of the large targeting error encountered in the cadaver experiments to the design flaw of the old TTI and the imperfect workflow in this pilot study.

Table 5.2. Targeting errors for the cadaveric experiment

Cadaver	Target	Targeting error
1	Corpus callosum	9 mm
2	Septum	3.4 mm

	Thalamus	4.4 mm

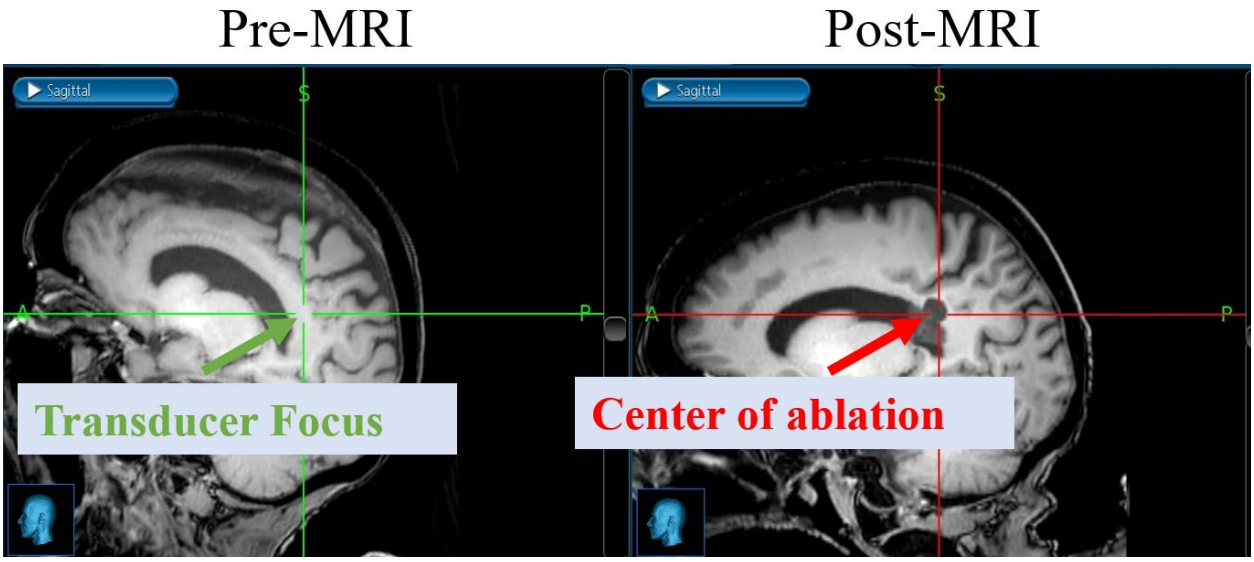

Figure 5.9. Pre-calibration cadaver experiment result with NaviTH: pre- and post-T1 MRI. With the initial setup, the corpus callosum of the cadaver was targeted and ablated. The green crosshair on the left pre-MRI points to the transducer focus at the time of treatment, and the right post-MRI image with a red crosshair shows the center of ablation created. The targeting error for this particular case was 9mm.

5.4.2 TRE Evaluation

To improve the targeting accuracy of the NaviTH system, a new TTI was designed and constructed. The target registration error (TRE) of the two different TTIs' was evaluated through two ex vivo human skulls (Fig. 5.9). The TRE resulted from the errors due to patient-to-image co-registration, the TTI-to-array focus tracking errors, and the neuronavigation-to-Kranion (N2K) transformation. For Skull 1, the TRE was 8.27mm (N=14) using the old TTI and 1.29 mm using the new TTI (N=12). For Skull 2, TRE was only measured with the new TTI and was 2.49mm (N=20). This large improvement in the TRE is attributed to the difference in the geometry of the two TTIs. In the new TTI, the reflective spheres were all located on the same plane as the

histotripsy array focus, and three of the spheres co-aligned with the array focus seemed to significantly reduce the TRE.

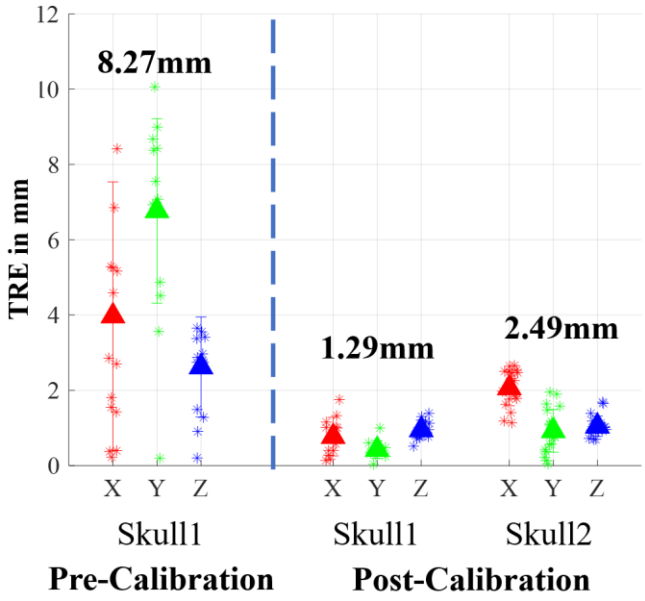

Figure 5.10. Target registration error (TRE) measurement pre and post-calibration. The calibration process in this study refers to changing the transducer tracking instrument (TTI) and correcting the neuronavigation-to-Kranion (N2K) transformation. The pre- and post-calibration Skull 1 TRE were 8.27 and 1.29mm, respectively, and the post-calibration TRE of Skull 2 was 2.49mm. Note the different y-axis scales on Skull 1 and Skull2.

5.4.3 Focal Shift due to skull aberration

Even with aberration correction, there is still a small shift of the focal location from the geometric focus of the array (focal shift) due to skull aberration. Focal shift due to skull aberration was evaluated *in vitro* using the ex vivo human skulls. Pin hydrophone was placed at the focus of the transducer in the freefield to align CAD focus to histotripsy array focus. Next, co-registration information of the skull from various skull locations was acquired, and two-step aberration correction was performed following the method described in our previous paper [22]. Cavitation clouds were generated at 27 different locations to evaluate the focal shift. The focal shift was evaluated by optically imaging the locations of the cavitation clouds generated in the freefield and

in the skulls (Fig. 5.10). Skull 1 had to be returned to the Anatomical Donations Program before the completion of the two camera experiments, and therefore only the focal shift in XY was obtained. The lateral (XY) offset of the cavitation clouds was 0.28mm in Skull 1, and the XYZ offset was 0.27mm in Skull 2, and no bias of the error was observed. Skull 1 lateral average focal shift (0.28mm) was larger than Skull 2 lateral average focal shift (0.15mm). Correspondingly, Skull 1 had a larger SDR (Table 5.1).

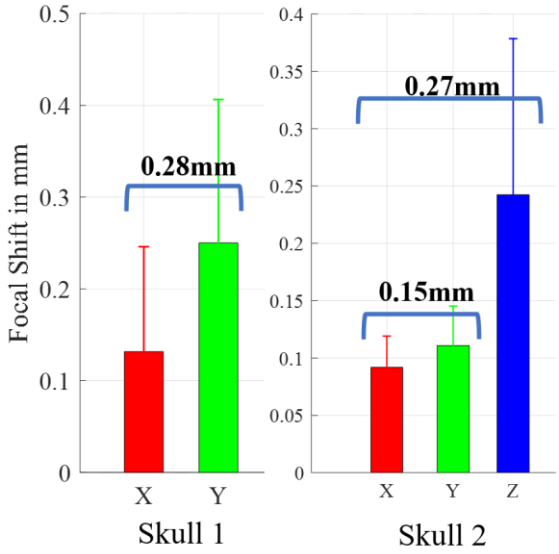

Figure 5.11. Focal shift induced by the skull aberrations measured with two orthogonally placed cameras. CT-based and cavitation-based AC were acquired, and histotripsy cavitation clouds were formed at various locations. The resulting shifts in the centroids of the cavitation clouds were recorded and subtracted from the freefield cavitation cloud locations. Skull 1 was returned to the Anatomical Donations Program and to the donor's family before the completion of the experiment and therefore, only XY focal shift data was obtained. The average lateral focal shift of Skull 1 was 0.28mm and the average focal shift of Skull 2 was 0.27mm.

5.4.4 Targeting accuracy of the NaviTH system using the new TTI

The system error was obtained by treating the red blood cell (RBC) phantoms (N=7) at various positions inside Skull 2. The system targeting error of 2.46mm (Fig. 5.12) was similar in total magnitude to the TRE of Skull 2 which was 2.49mm. The distribution of the errors in xyz

observed in this experiment was also similar to the distribution of Skull 2 TRE. Only Skull 2 was used for this experiment because Skull 1 was returned to Anatomical Donations Program.

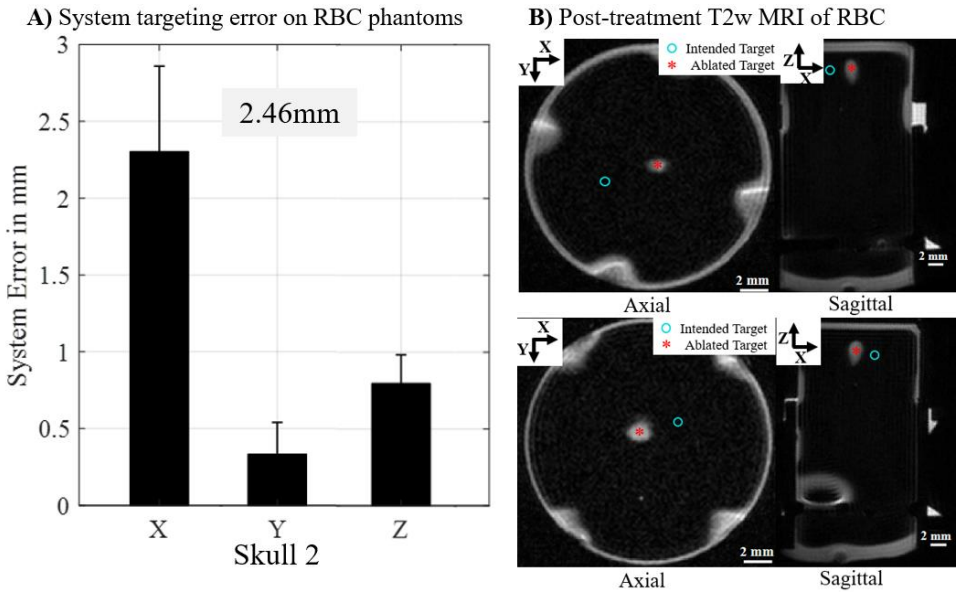

Figure 5.12. Post-calibration system targeting error of NaviTH system on RBC gel phantoms. (A) A total of seven RBC gel phantoms were ablated using the NaviTH system to produce a system targeting error of 2.46mm with Skull 2. B) shows two cases of T2w MRI of RBC gel phantoms after treatment by the NaviTH system.

5.5 Discussion

A neuronavigation-guided transcranial histotripsy (NaviTH) system was developed. The feasibility was demonstrated in human cadavers, and the system error was evaluated with excised human skulls. The system accuracy of the NaviTH has two primary sources of error: 1) the co-registration of the brain to the histotripsy array based on the neuronavigation device and 2) skull aberration. The co-registration error or the target registration error (TRE) was found to be mainly derived from the transducer tracking instrument (TTI). The error from the skull aberration is characterized by the focal shift compared to without the skull.

The feasibility of the NaviTH was demonstrated in the brains of two <96hours post-mortem human cadavers. However, the targeting error was large (3-9 mm), which was attributed to the initial development of workflow and equipment as well as the old TTI design flaws impacting the TRE. An example of the equipment flaw was the stereotactic head fixture, which was designed with the average size of an adult head in mind (circumference of 55-57cm) with adjustability. However, both cadavers had head sizes much smaller than average heads, so the patient head immobilization via the stereotactic frame was weak due to the short length of head fixing screws, which adds to the co-registration error (TRE).

The post-calibration NaviTH system was tested on red blood cell (RBC) gel phantoms with Skull 2. The system error of 2.46mm and the TRE of Skull 2 (2.49mm) were similar. The system error was within the range of the expected value considering both the TRE and the focal shift of Skull 2. Adding the uncertainties of TRE (2.49mm) and focal shift (0.27mm) by Skull 2 produces 2.50mm, which is very close to the TRE of Skull 2. This reinforces the need to improve the TRE in future studies to further minimize sources of error caused by co-registration.

The old TTI design had a major impact on the targeting error. In fact, the TRE reduced from ~8mm to ~2mm using the old TTI and new TTI. The main change in the alignment of the retroreflective sphere (RRS) on the TTI turned out to have a large impact on the co-registration accuracy. The TTI TRE may be further improved by incorporating manual divot verification. This method includes verifying the location of a divot or a target point with the coordinate reference frame (CRF), therefore, physically registering the location of the target. A similar workflow is performed with the co-registration wand and can be adopted for improving the TTI TRE via fabricating a rigid structure that has a point target at the geometric focus of the histotripsy transducer. The TTI remains in the same location on the transducer, but this new structure can be

temporarily attached to the transducer during instrument registration and before the co-registration process. The new structure divot or the transducer focus can be manually registered via the CRF, and the structure can be removed from the transducer.

The average TRE for Skull 1 was 1.2mm smaller than that of Skull 2. A 1/4in drill hole was present in Skull 1, which may have served as a fiducial marker for co-registration by the neuronavigation system. Fiducial markers or skull screws are known to minimize the TRE for neuronavigation co-registration [25-26]. The manual divot procedure described in the previous paragraph and the skull screws for fiducial markers may improve the TRE and will be considered for optimizing TRE for NaviTH in future cadaveric experiments.

For the NaviTH system, Kranion was used for skull aberration correction. Neuronavigation-to-Kranion (N2K) transformation was iterated to equate neuronavigation image space with Kranion image space. One major point of discovery was that Kranion coordinate system did not obey the right-hand rule, and therefore when transforming the neuronavigation exam space to Kranion coordinate space, a negation on the axial (z) direction was additionally applied to equate the neuronavigation scene to the Kranion scene. Another important aspect is to use the same CT series for both the neuronavigation and Kranion, for the DICOM file of different series may include different information such as the image origins that may miscalculate the location of the skull relative to the geometric focus of the transducer.

After the evaluation of co-registration, the focal shift induced by skull post-aberration correction was independently analyzed, and an average shift of 0.27mm in histotripsy cavitation cloud locations was observed between the freefield and through the skull. Most of the shift was observed in the z-axis (Fig. 5.10) of the transducer for Skull 2, as previously observed [18]. The focal shift magnitude after the two-step aberration correction also agreed with the previous

observation [22]. The focal shift, however minimal, may stem from the remnant TRE and the performance of CT-based aberration correction (AC). The CT-based AC is acquired after N2K, which includes the ~2mm TRE. Even if the skull thickness and the incidence angle stay relatively uniform within the 2mm window, the subtle differences may contribute to the error. In addition, the CT-based AC used for this study assumed a constant speed of sound at 2300m/s, which is an approximate, while in reality, the cortical and trabecular bones within the skull vary in speed of sound [27]. An improved co-registration, TRE, and CT-based AC may further minimize the skull aberration-induced focal shift.

In this experiment, a neuronavigation-guided transcranial histotripsy clinical workflow was developed. However, the number of steps involved in this workflow can be reduced if the neuronavigation system (co-registration) and CT-based AC can be combined into one platform [28] to streamline the workflow and further reduce the error. Replacing the neuronavigation system with an infrared stereoscopic camera connected to a laptop with one software platform that executes co-registration, CT-based AC, and treatment planning will not only simplify the system but also significantly increase technology adoption and minimize costs and components associated with the system.

This study presented the first NaviTH system, and its feasibility was demonstrated in the brain of human cadavers and through excused human skulls. Using the old TTI, the errors observed in preliminary cadaver experiments (4-9mm targeting error) were high but match well with that observed through the excised human skull (~8mm). Unfortunately, we have not been able to perform the treatment using the NaviTH system with the new TTI, as we could not obtain any human cadavers due to COVID in the past year and a half. We anticipate that the targeting accuracy of 1.9mm using the new TTI will translate to future human cadaveric experiments. More

experiments are needed to evaluate the robustness, efficacy, and treatment location envelop of this NaviTH system in the brain, which will inform the capabilities and limitations of the NaviTH as a potential neurosurgical tool and bring transcranial histotripsy closer to the clinic.

5.6 References

[1] N. Y. Jung, C. K. Park, M. Kim, P. H. Lee, Y. H. Sohn, and J. W. Chang, "The efficacy and limits of magnetic resonance–guided focused ultrasound pallidotomy for Parkinson's disease: A Phase I clinical trial," J. Neurosurg., vol. 1306, no. 6, pp. 1853–1861, 2019, doi: 10.3171/2018.2.JNS172514.

[2] D. Coluccia et al., "First noninvasive thermal ablation of a brain tumor with MR-guided focused ultrasound," J. Ther. Ultrasound, vol. 2, no. 1, pp. 1–7, 2014, doi: 10.1186/2050-5736-2-17.

[3] W. J. Elias *et al.*, "A randomized trial of focused ultrasound thalamotomy for essential tremor," *N. Engl. J. Med.*, vol. 375, no. 8, pp. 730–739, 2016, doi: 10.1056/NEJMoa1600159.

[4] W. J. Elias *et al.*, "A Pilot Study of Focused Ultrasound Thalamotomy for Essential Tremor," *N. Engl. J. Med.*, vol. 369, no. 7, pp. 640–648, 2013, doi: 10.1056/nejmoa1300962.

[5] N. Lipsman *et al.*, "MR-guided focused ultrasound thalamotomy for essential tremor: A proof-of-concept study," *Lancet Neurol.*, vol. 12, no. 5, pp. 462–468, 2013, doi: 10.1016/S1474-4422(13)70048-6.

[6] M. Wintermark *et al.*, "Imaging findings in mr imaging-guided focused ultrasound treatment for patients with essential tremor," *Am. J. Neuroradiol.*, vol. 39, no. 5, pp. 891–896, 2014, doi: 10.3174/ajnr.A3808.

[7] A. H. Chung, F. A. Jolesz, and K. Hynynen, "Thermal dosimetry of a focused ultrasound beam in vivo by magnetic resonance imaging," *Med. Phys.*, vol. 26, no. 9, pp. 2017–2026, 1999, doi: 10.1118/1.598707.

[8] K. Hynynen, N. McDannold, N. A. Sheikov, F. A. Jolesz, and N. Vykhodtseva, "Local and reversible blood-brain barrier disruption by noninvasive focused ultrasound at frequencies suitable for trans-skull sonications," *Neuroimage*, vol. 24, no. 1, pp. 12–20, 2005, doi: 10.1016/j.neuroimage.2004.06.046.

[9] K.-T. Chen *et al.*, "Neuronavigation-guided focused ultrasound for transcranial blood-brain barrier opening and immunostimulation in brain tumors," *Sci. Adv*, vol. 7, no. February, 2021.

[10] H. L. Liu, H. C. Tsai, Y. J. Lu, and K. C. Wei, “Neuronavigation-guided focused ultrasound-induced blood-brain barrier opening: A preliminary study in swine,” *AIP Conf. Proc.*, vol. 1503, pp. 29–34, 2012, doi: 10.1063/1.4769912.

[11] Z. Xu *et al.*, “Controlled ultrasound tissue erosion.,” *IEEE Trans. Ultrason. Ferroelectr. Freq. Control*, vol. 51, no. 6, pp. 726–736, 2004, doi: 10.1109/TUFFC.2004.1304271.

[12] J. E. Parsons, C. A. Cain, G. D. Abrams, and J. B. Fowlkes, “Pulsed cavitational ultrasound therapy for controlled tissue homogenization,” *Ultrasound Med. Biol.*, 2006, doi: 10.1016/j.ultrasmedbio.2005.09.005.

[13] E. Vlaisavljevich, A. Maxwell, L. Mancia, E. Johnsen, C. Cain, and Z. Xu, “Visualizing the Histotripsy Process: Bubble Cloud–Cancer Cell Interactions in a Tissue-Mimicking Environment,” *Ultrasound Med. Biol.*, vol. 42, no. 10, pp. 2466–2477, Oct. 2016, doi: 10.1016/J.ULTRASMEDBIO.2016.05.018.

[14] T. Gerhardson, J. R. Sukovich, A. S. Pandey, T. L. Hall, C. A. Cain, and Z. Xu, “Effect of Frequency and Focal Spacing on Transcranial Histotripsy Clot Liquefaction, Using Electronic Focal Steering,” *Ultrasound Med. Biol.*, vol. 43, no. 10, pp. 2302–2317, 2017, doi: 10.1016/j.ultrasmedbio.2017.06.010.

[15] T. Gerhardson *et al.*, “Histotripsy Clot Liquefaction in a Porcine Intracerebral Hemorrhage Model,” *Clin. Neurosurg.*, vol. 86, no. 3, pp. 429–436, 2020, doi: 10.1093/neuros/nyz089.

[16] N. Lu *et al.*, “Transcranial MR-guided Histotripsy System,” *IEEE Trans. Ultrason. Ferroelectr. Freq. Control*, vol. 68, no. 9, pp. 2917–2929, 2021, doi: 10.1109/TUFFC.2021.3068113.

[17] S. W. Choi *et al.*, “Stereotactic Transcranial Focused Ultrasound Targeting System for Murine Brain Models,” *IEEE Trans. Ultrason. Ferroelectr. Freq. Control*, vol. 68, no. 1, pp. 154–163, 2021, doi: 10.1109/TUFFC.2020.3012303.

[18] J. R. Sukovich, J. J. MacOskey, J. E. Lundt, T. I. Gerhardson, T. L. Hall, and Z. Xu, “Real-Time Transcranial Histotripsy Treatment Localization and Mapping Using Acoustic Cavitation Emission Feedback,” *IEEE Trans. Ultrason. Ferroelectr. Freq. Control*, vol. 67, no. 6, pp. 1178–1191, 2020, doi: 10.1109/TUFFC.2020.2967586.

[19] D. A. Orringer, A. Golby, and F. Jolesz, “Neuronavigation in the surgical management of brain tumors: Current and future trends,” *Expert Rev. Med. Devices*, vol. 9, no. 5, pp. 491–500, 2012, doi: 10.1586/erd.12.42.

[20] "StealthStation Surgical Navigation," Medtronic, Nov 10, 2022, https://www.medtronic.com/us-en/healthcare-professionals/products/neurological/surgical-navigation-systems/stealthstation/cranial-neurosurgery-navigation.html

[21] F. Sammartino, D. W. Beam, J. Snell, and V. Krishna, “Kranion, an open-source environment for planning transcranial focused ultrasound surgery: technical note,” *J. Neurosurg.*, pp. 1–7, 2019, doi: 10.3171/2018.11.jns181995.

[22] N. Lu *et al.*, “Two-step aberration correction: application to transcranial histotripsy,” *Phys. Med. Biol.*, vol. 67, no. 12, 2022, doi: 10.1088/1361-6560/ac72ed.

[23] J. B. West and C. R. Maurer, “Designing optically tracked instruments for image-guided surgery,” *IEEE Trans. Med. Imaging*, vol. 23, no. 5, pp. 533–545, 2004, doi: 10.1109/TMI.2004.825614.

[24] S. Y. Wu *et al.*, “Efficient blood-brain barrier opening in primates with neuronavigation-guided ultrasound and real-time acoustic mapping,” *Sci. Rep.*, vol. 8, no. 1, pp. 1–11, 2018, doi: 10.1038/s41598-018-25904-9.

[25] D. P. Perrin *et al.*, “Image Guided Surgical Interventions,” *Curr. Probl. Surg.*, vol. 46, no. 9, pp. 730–766, 2009, doi: 10.1067/j.cpsurg.2009.04.001.

[26] D. Pinggera *et al.*, “Accuracy Validation of Neuronavigation Comparing Headholder-Based System with Head-Mounted Array—A Cadaveric Study,” *World Neurosurg.*, vol. 120, pp. e313–e317, 2018, doi: 10.1016/j.wneu.2018.08.059.

[27] S. Pichardo, V. W. Sin, K. Hynynen, and P. Net, “Multi-frequency characterization of the speed of sound and attenuation coefficient for longitudinal transmission of freshly excised human skulls,” *Phys Med Biol*, vol. 56, no. 1, pp. 219–250, 2011, doi: 10.1088/0031-9155/56/1/014.

[28] V. Chaplin *et al.*, “On the accuracy of optically tracked transducers for image-guided transcranial ultrasound,” *Int. J. Comput. Assist. Radiol. Surg.*, vol. 14, no. 8, pp. 1317–1327, 2019, doi: 10.1007/s11548-019-01988-0.

[29] A. D. Maxwell, T. Y. Wang, L. Yuan, A. P. Duryea, Z. Xu, and C. A. Cain, “A tissue phantom for visualization and measurement of ultrasound-induced cavitation damage,” *Ultrasound Med. Biol.*, 2010, doi: 10.1016/j.ultrasmedbio.2010.08.023.

[30] S. P. Allen *et al.*, “The response of MRI contrast parameters in in vitro tissues and tissue mimicking phantoms to fractionation by histotripsy,” *Phys. Med. Biol.*, vol. 62, no. 17, pp. 7167–7180, 2017, doi: 10.1088/1361-6560/aa81ed.

Chapter 6 Summary and Future Work

6.1 Summary

This dissertation is focused on the transcranial application of pulsed cavitational ultrasound therapy (histotripsy) on the murine model and its translation to the cadaver model, with a focus on the development of image-guided transcranial histotripsy platform and radio-histological features following histotripsy. The work starts with a demonstration of the submillimeter targeting accuracy of the transcranial histotripsy stereotactic platform on a murine model with a glioblastoma (GBM) tumor. This is followed by an investigation of *in vivo* murine magnetic resonance (MR) temporal signatures post-histotripsy treatment and correlated with the H&E histological feature. Next, the blood-brain barrier (BBB) disruption caused by transcranial histotripsy is characterized in a group of healthy mice to provide insight into the behavior of BBB at the periphery of histotripsy ablation. The dissertation ends with the systemic evaluation of the neuronavigation-guided transcranial histotripsy (NaviTH) system designed for cadavers. The intention of the mouse portion of the work is to provide targeting, workflow, monitoring tools, and basic *in vivo* characteristics of transcranial histotripsy. In addition, this will provide tools for future immunological studies to investigate the immunomodulatory effects of transcranial histotripsy on brain tumors. The cadaver work is a foundational work that establishes the workflow for human patient treatments and prepares the transcranial histotripsy system for future cadaveric experiments and potentially, clinical trials.

Research & Development: A stereotactic transcranial focused ultrasound platform was developed and characterized for *in vivo* murine application. A reliable workflow was created for this stereotactic procedure and an accuracy of 0.48 ± 0.38 mm was achieved with this workflow

after correcting for a systematic error found by the propagation of error analysis []. Subsequently, the initial long-term MR signature of transcranial histotripsy volume ablation was investigated on *in vivo* murine model and correlated to H&E histology to provide a basic understanding of *in vivo* transcranial histotripsy. The aforementioned stereotactic platform was used to generate ~5mm^3 histotripsy ablation volume in both mice with and without tumors. The study observed normal mice up to 28 days post-histotripsy, and histotripsy was well-tolerated by the normal mice. The glioma cell line used in this study was the most aggressive glioblastoma cells and this limited the observation period for tumor-bearing mice to 7 days post-histotripsy. The results provide a library of T2, T2*, T1, and T1-contrast MR images and corresponding H&E histology to guide future monitoring of murine transcranial histotripsy experiments. The set of T1-contrast MR images and corresponding tight junction protein-stained images provided further understanding of the BBB opening at the periphery of the histotripsy ablation. The T1 contrast images around the histotripsy ablation zone are most hyperintense on day 7 post-histotripsy but the intensity subsides over time after day 7, suggesting the recovery of BBB opening caused by histotripsy. The tight junction (TJ) protein stains support this observation: ZO-1 and Claudin-5 expressions are not observed on day 0 and are sparsely observed on days 7 and 14. On days 21 and 28, at the periphery of histotripsy ablation, TJ protein expression resembles that of a healthy BBB. Finally, the neuronavigation-guided transcranial histotripsy of the cadaveric model was developed. Its feasibility was tested in two, <96 hours post-mortem, whole-body cadavers, and the targeting accuracy was characterized with two *ex vivo* human skulls. Its developed workflow for the evaluation of the system provides an accurate and reliable surgical tool for future cadaveric studies.

6.2 Future Work: Transcranial histotripsy for mice

6.2.1 Improved stereotactic platform for transcranial histotripsy

This work provided the development and evaluation of a stereotactic targeting platform for transcranial histotripsy. The workflow can be improved by upgrading *a) the stereotactic frame and b) the experimental setup.*

a) Stereotactic frame: The current stereotactic frame is composed of fiducial markers, a nose cone, and ear bars (Fig. 2.1). The ear bars are inserted deep inside the mice ears until the mice skull is adequately immobilized. This adequate immobilization is tested by gently pushing the mice's heads. However, inserting the ear bars into the ears of the mice often leads to the narrowing of the airway and leads to asphyxiation for mice. Occasionally, this ear bar insertion does not immobilize the head and the mouse's head moves in the stereotactic frame during histotripsy surgery, resulting in poor co-registration and mistargeting of the brain tumor.

The next generation stereotactic frame can be improved by adopting features from existing stereotaxic instruments (Lab Standard Stereotaxic, Rat and Mouse, Stoelting, Chicago, Illinois, USA) such as bite bar and additionally ear bars to clamp on the skull by the ear [1]. The bite bar can minimize the mouse head movement inside the frame, and the ear bars contacting the skull further immobilize the mouse head. The bite bars and the ear bars can contribute to a more reliable fixation of the mouse's head in the stereotactic frame.

b) Experimental setup: The experimental setup for the stereotactic transcranial histotripsy setup is shown in Figure 2.2, and the transducer-to-motor positioner connection (Fig. 2.2b, 5) needs improvement. The current connection is achieved by a pair of long optical rods with each optical rod fixed to the motor positioner by one 1/4-20 screw. As a result of this moment arm, the histotripsy transducer is rotated along the yz axis (Fig. 2.2b) and the transducer aperture surface is not parallel to the bottom surface of the treatment bed. The bottom surface of the treatment bed is where the stereotactic frame holding the mouse is placed. If the treatment bed and the transducer

aperture surface are not parallel, this introduces a small rotation of the transducer and results in inaccurate co-registration, leading to overall system targeting error. By introducing a setup that ensures parallel surface contact between the treatment bed and the aperture surface, a more robust stereotactic transcranial histotripsy targeting system can be built. A simple improvement is introduced by another set of ¼-20 screws on the optical rod, spaced two inches from the other screws to ensure a perpendicular optical rod and to minimize the moment arm of the transducer-to-positioner connection.

6.2.2 Transcranial histotripsy MRI and histology follow-up

The response of transcranial histotripsy has been recorded via T2, T2*, T1, and T1-Gd MRI and related to H&E histology in both mice with GBM tumor and without tumor. Two important observations from this study were: a) in T1-Gd MRI, the histotripsy ablation zone has a higher intensity than the residual tumor zone, and b) histotripsy blood product, hemosiderin, is left in normal mice brain up to day 28 after histotripsy.

a) Dynamic Contrast-enhanced (DCE) T1-Gd MRI to study gadolinium uptake difference in tumor and histotripsy lesion: DCE T1-Gd MRI in the brain records the different degrees of BBB permeability (i.e. gadolinium uptake differences) [3-5]. Both tumor and histotripsy lesions lead to open BBB and DCE can inform the BBB permeability difference between histotripsy lesions and tumors. The tumor cells rapidly replicate and recruit blood vessels for nutrients, leading to the blood-tumor barrier (BTB). BTB does not have the selectivity or the narrow paracellular space as seen in BBB [6]. Therefore, the gadolinium leaks out through the BTB and can be visualized in T1-Gd. On the other hand, the histotripsy treatment zone is completely ablated, devoid of BBB, BTB, or any tumor cells. Therefore, the small gadolinium molecules are hypothesized to leak through the histotripsy zone faster than they do in the BTB environment.

b) Effects of post-histotripsy blood products in the brain: Transcranial histotripsy on mice brains have shown residual iron-product (i.e. hemosiderin) in the brain parenchyma even after 28 days after treatment. The reported effects of blood products on the brain are not favorable [7] and have been shown to affect the cognitive function of the brain [8]. Therefore, the effects of histotripsy blood products on the brain should be further investigated to decide whether iron-chelating agents should be administered, or the blood products should be extracted to minimize harmful effects on the animals and patients.

6.2.3 Effects of transcranial histotripsy on the blood-brain barrier (BBB)

The state of BBB at the periphery of the histotripsy zone has been qualitatively studied via T1-Gd MRI and BBB tight junction protein stains (ZO-1 and Claudin-5). However, the exact physical mechanism of BBB disruption by histotripsy cavitation bubble clouds at the periphery of the treatment zone remains unknown. This may be studied via high-speed imaging with an *in vitro* BBB. A combination of biofabrication techniques can be used to culture BBB in hydrogels [9]. Then this hydrogel can be treated with histotripsy and the cellular disruption at the periphery of the histotripsy zone can be observed with high-speed imaging similar to previous work to visualize histotripsy cavitation bubble clouds [10].

6.3 Future Work: Neuronavigation-guided Transcranial Histotripsy (NaviTH)

The first NaviTH system was developed. The feasibility of treating the cadaver brain with histotripsy was demonstrated and the system was evaluated to increase its targeting accuracy. However, the system can be further improved in *a) target registration error (TRE), b) workflow, and c) setup* to improve NaviTH system and bring the technology closer to the clinic.

6.3.1 Improving the TRE:

The TRE in NaviTH describes the co-registration error between the patient to medical image and the transducer focus location determined by the transducer tracking instrument (TTI). TRE was decreased from ~8mm to 2mm, but it can be further decreased by i) implementing rigid transducer scaffold components, ii) placing the TTI closer to the histotripsy focus, and iii) attempting manual registration of the focus.

i) First, the current transducer scaffold manufactured with Delrin plastic has deformed over the years due to the weight of the transducer elements and wires weighing on the scaffold. By fabricating the next histotripsy transducer scaffold with aluminum, the transducer scaffold deformation (i.e. creeping) over time can be minimized and ensure the consistent geometry of the transducer over years of usage. In addition, the current transducer front plate that holds the TTI was laser-cut with a general-purpose ¼in thick general-purpose (6061) aluminum. This aluminum sheet plate had a small warping and thickness tolerance of 0.254mm (0.01”). The warping of the aluminum transducer front plate combined with the deformed transducer scaffold is thought to contribute to the magnitude of uncertainty observed in TRE. By manufacturing the transducer front plate to be made out of high-precision (i.e. tight thickness tolerance) metal instead of general-purpose aluminum, the uncertainty can be decreased.

ii) The current TTI is placed ~370mm from the transducer focus on the transducer front plate and is 3D-printed. The placement provides a long lever arm where 1 degree of misalignment of the TTI respective to the transducer focus can translate to 6.5mm of misalignment ($\tan(1^{o})$ * 370mm). The current TTI placement is restricted by the water-coupling setup (**Fig. 5.3A**). By improving the water-coupling setup and the placement of the TTI closer to the focus of the transducer, the TRE uncertainty can be further decreased. The schematic of the improved TTI location and the water-coupling setup is presented and discussed in section 6.3.3.

iii) The concept of manual registration of the target of the TTI (i.e. histotripsy focus) by a physical focus-informing structure is discussed in section 5.5. The manual registration can be incorporated into the workflow before the patient-to-CRF co-registration process.

6.3.2 Improving the workflow:

The proposed improved workflow is presented in Figure 6.1. The major change to the workflow is the addition of a "CT-based treatment planning optimization" step. 1) After obtaining CT and MRI, the treatment targets are determined. 2) The target treatment planning is simulated with ray-tracing or K-wave to calculate the best position of the histotripsy array relative to the intended treatment target. This simulation also provides CT-based aberration correction (AC) information. 3) At the time of treatment, the patient is co-registered, and 4) the transducer is positioned at the optimal location relative to the patient. The optimal location obtained from the treatment planning simulation achieves the best incidence angles for histotripsy transducer elements to increase the chances of initial cavitation at the desired location. 5) Initial histotripsy cavitation bubbles are generated and subsequent acoustic cavitation emission-based AC is obtained. The treatment is delivered and 6) the post-histotripsy system targeting accuracy is evaluated by MRI.

Figure 6.1. Proposed future NaviTH workflow. A new NaviTH workflow is proposed. 1) Array tracker (TTI) information and pre-operative CT and MRI images are uploaded to the neuronavigation system. From the medical images, the treatment target in the brain is selected. 2) CT-based treatment planning by ray-tracing or K-wave simulation is conducted to acquire the best

rotation angle and position of the histotripsy transducer relative to the head of the patient. TTI manual target co-registration process is performed, and this is followed by 3) the co-registration of the patient to the medical images. 4) The histotripsy transducer focus is positioned at the treatment target of interest. 5) Two-step aberration correction (AC) is achieved, and histotripsy treatment is delivered. 6) The system targeting accuracy is performed by comparing the pre and postoperative MRI.

6.3.3 Improving the setup:

The next-generation transducer setup is presented in Figure 6.2. The main components for improvement are a) water-coupling, b) TTI, c) stereotactic frame, and d) transducer positioner. Improving the setup will also simplify the workflow and decrease uncertainty in the TRE.

a) Water-coupling: The current water-coupling consists of a cubic acrylic water tank capable of holding 50 gallons of water with the side of the water tank open for cadaver head insertion (Fig. 6.2i). A rubber membrane with a center hole is donned over the dome of the cadaver head. The side of the rubber membrane is pulled down to the ears, and the back of the membrane is pulled down to the bottom of the occipital bone. After the rubber membrane is secure, the cadaver head is inserted into the water tank to close the open side of the water tank. However, this membrane-to-cadaver contact is not watertight. Occasionally, water leaks from the rubber membrane-to-head interface. This leakage during the experiment and the burden of degassing 50 gallons of water, which usually takes several hours, add logistical burdens to the experimental workflow. By replacing the water tank with a watertight membrane encompassing the histotripsy array as shown in Figure 6.2ii (element A), the cumbersome water tank can be eliminated to improve workflow. Ultrasound gel can be applied to the scalp of the patient before the patient positioning inside the histotripsy array to minimize the chance of trapping air bubbles between the membrane and the scalp of the cadaver.

b) Rigid TTI: As previously mentioned, the current TTI is attached to the transducer front plate, placed higher than the acrylic water tank (Fig. 6.2i, element B) to be visible under the

neuronavigation system camera. This positions the TTI far from the transducer focus and contributes to the uncertainties observed in the TRE. Moreover, the TTI's connection to the transducer front plate is secured by two screws at the bottom of the TTI, creating a long moment arm. The long moment arm of the TTI over time can contribute to the deformation of the fragile 3D-printed material, and further contribute to the TRE.

Placement, retroreflective spheres (RRSs) pattern, and material of the TTI can be improved to decrease TRE-associated uncertainty. The placement of the TTI can be improved as demonstrated in Figure 6.2ii (element B), by decreasing the distance between TTI retroreflective spheres (RRSs) and the focus of the transducer. The TTI can be further immobilized by supporting beam placement connecting the transducer scaffold to the body of the TTI, deterring any rotational misalignment that can contribute to the TRE. Next, all the RRSs on the TTI can be designed to be colinear with the focus of the transducer. Currently, three out of the five spheres are co-axially placed and the remaining two spheres are arbitrarily placed off to the side. Those two side spheres can form a line from the transducer focus to decrease TRE uncertainty (Fig. 6.2ii, element B, green dotted lines). The TTI can be fabricated out of aluminum to increase the rigidity of the structure.

c) Stereotactic frame: The current stereotactic frame connects to the water coupling system by an extension at the bottom of the frame and immobilizes the head of the patient with four pointed screws (Fig. 6.2i, element C). The frame extension impinges on the shoulder of the human cadavers, and it is difficult to achieve mechanical co-registration of the frame to the water coupling system. For the hand-tightened four-pointed screws on the current frame, the head immobilization is achieved by contacting the pointed screws to the zygomatic bones and the bottom of the occipital bone of the cadaver skull. However, the stereotactic frame screw positions are fixed and do not account for the different dimensions of the cadaver heads.

An adjustable Mayfield clamp-like (MAYFIELD Skull Clamps, Integra LifeSciences, Princeton, NJ, USA) stereotactic frame that can clamp onto the zygomatic bone as well as the bottom of the occipital bone to better immobilize the skull may be better suited for NaviTH system. This proposed frame has larger skull contact areas than the pointed screws to spread the immobilization force and can extend towards the x direction in Figure 6.2ii (element C) to avoid the shoulder-frame impingement experienced by the current stereotactic frame. The frame can be mechanically co-registered to the supporting metal board laying at the bottom of the head. This supporting board can also serve to partially support the transducer if the transducer and the electronic wires are heavy for the mechanical arm (Fig. 6.2ii, element D).

d) transducer positioner: The current setup only allows 3-axis positioning without rotation (Fig. 6.2i, element D), and the transducer is fixed at one orientation. However, to treat a variety of locations within the skull, a transducer mechanical arm capable of both rotation and translation is necessary to optimize the transmission of ultrasound through the skull. This rotation angle and the transducer position relative to the cadaver head can be determined by the pre-treatment CT-based simulation mentioned previously. The mechanical arm capable of rotation and translation has been demonstrated in histotripsy [11], but this arm was designed for light and small transducers. For NaviTH, the load capacity of the arm needs to account for the new aluminum scaffold, the TTI, the transducer elements, and the wires connected to the elements.

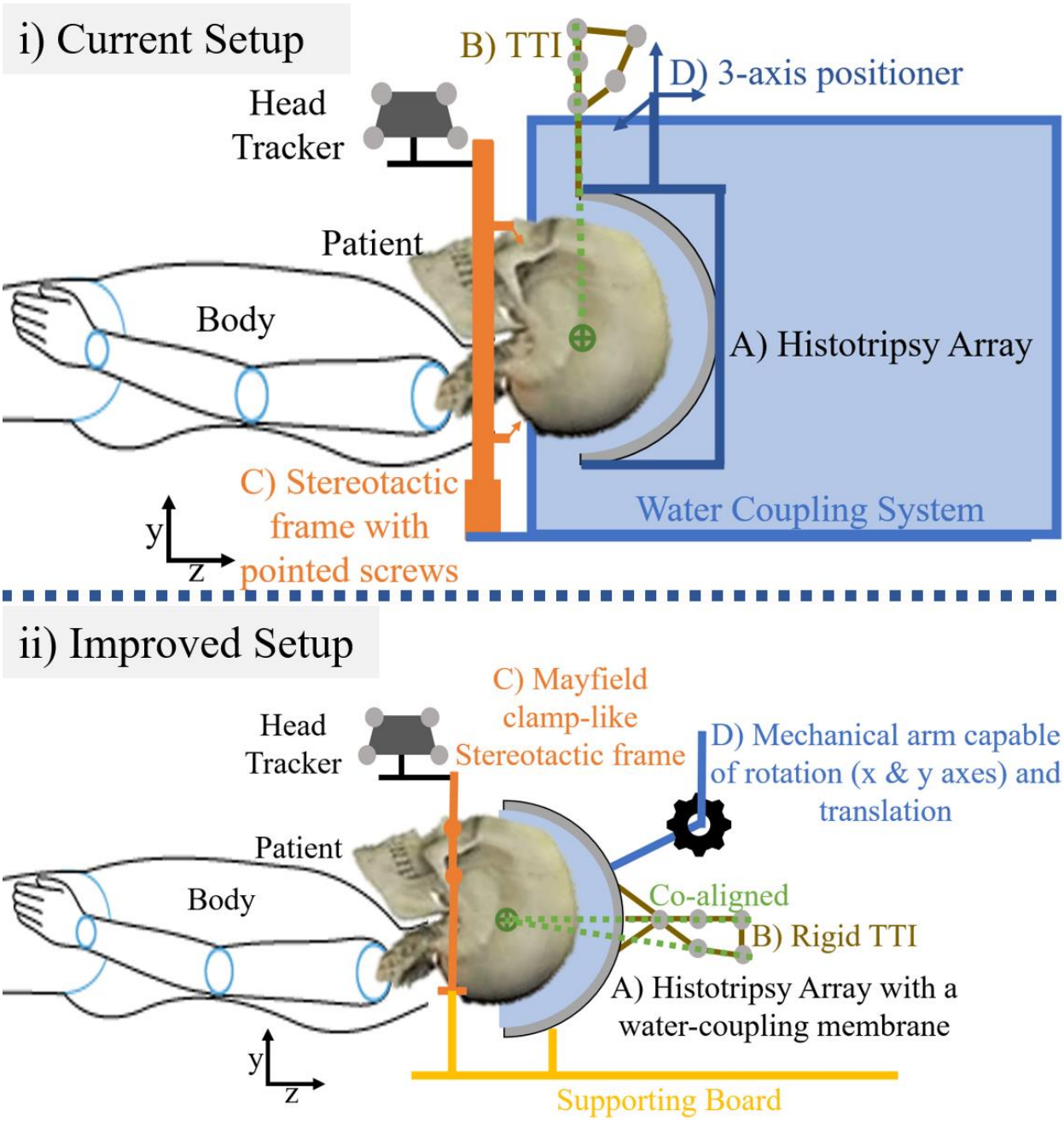

Figure 6.2. Schematics of current and improved NaviTH experimental setup. i) depicts the current NaviTH experimental setup: The histotripsy array (A) equipped with TTI (B) is submerged in a 50-gallon acrylic water tank. The water tank is part of the water coupling system. The stereotactic frame (C) that immobilizes the patient is connected to the water coupling system. The histotripsy array is translated by the 3-axis positioner (D) that is part of the water coupling system. ii) depicts the proposed improved setup NaviTH setup schematic. The 50-gallon water tank is replaced by a watertight, water-coupling membrane that envelopes the histotripsy array (A). The new TTI (B) is positioned coaxially with the histotripsy array. The new TTI design has three major improvements. First, the distance from the retroreflective spheres (RRSs) to the histotripsy focus is reduced. Next, all the RRSs are co-aligned with the histotripsy focus as illustrated by the two dotted green lines

connecting the five spheres. Third, the TTI is securely rooted to the histotripsy array and by the supporting beams at the body of the TTI. The beams serve to eliminate any misalignment of the TTI respective to the histotripsy focus. C) The new stereotactic frame does not use pointed screws but uses Mayfield clamp-like design to immobilize the skull. The frame also does not impinge on the shoulder of the cadaver due to the frame extending out of the page (x-axis). The frame is attached to the supporting metal board/table underneath the head and the histotripsy array. Finally, the transducer mechanical arm capable of rotation and translation (D) replaces the 3D-positioning system from i). The mechanical arm safely moves the transducer and can rotate and position the transducer in a pre-calculated location respective to the patient's head. The pre-calculated location comes from the CT-based treatment planning mentioned in Figure 6.1.

6.4 References

[1] P. Osten, A. Cetin, S. Komai, M. Eliava, and P. H. Seeburg, "Stereotaxic gene delivery in the rodent brain," *Nat. Protoc.*, vol. 1, no. 6, pp. 3166–3173, 2007, doi: 10.1038/nprot.2006.450.

[2] J. E. Lundt, S. P. Allen, J. Shi, T. L. Hall, C. A. Cain, and Z. Xu, "Noninvasive, Rapid Ablation of Tissue Volume Using Histotripsy," doi: 10.1016/j.ultrasmedbio.2017.08.006.

[3] S. S. Oh *et al.*, "The use of dynamic contrast-enhanced magnetic resonance imaging for the evaluation of blood-brain barrier disruption in traumatic brain injury: What is the evidence?," *Brain Sci.*, vol. 11, no. 6, 2021, doi: 10.3390/brainsci11060775.

[4] J. B. Ware *et al.*, "Dynamic contrast enhanced MRI for characterization of blood-brain-barrier dysfunction after traumatic brain injury," *NeuroImage Clin.*, vol. 36, no. June, p. 103236, 2022, doi: 10.1016/j.nicl.2022.103236.

[5] P. S. Tofts and A. G. Kermode, "Measurement of the blood-brain barrier permeability and leakage space using dynamic MR imaging. 1. Fundamental concepts," *Magn. Reson. Med.*, vol. 17, no. 2, pp. 357–367, 1991, doi: 10.1002/mrm.1910170208.

[6] F. Yuan, H. A. Salehi, Y. Boucher, R. K. Jain, U. S. Vasthare, and R. F. Tuma, "Vascular Permeability and Microcirculation of Gliomas and Mammary Carcinomas Transplanted in Rat and Mouse Cranial Windows," *Cancer Res.*, vol. 54, no. 17, pp. 4564–4568, 1994.

[7] T. Garton, R. F. Keep, Y. Hua, and G. Xi, "Brain iron overload following intracranial haemorrhage," *Stroke Vasc. Neurol.*, vol. 1, no. 4, pp. 172–184, 2016, doi: 10.1136/svn-2016-000042.

[8] R. R. Crichton, R. J. Ward, and R. C. Hider, "The efficacy of iron chelators for removing iron from specific brain regions and the pituitary—Ironing out the brain," *Pharmaceuticals*, vol. 12, no. 3, 2019, doi: 10.3390/ph12030138.

[9] T. J. DePalma, H. Sivakumar, and A. Skardal, “Strategies for developing complex multi-component in vitro tumor models: Highlights in glioblastoma,” *Adv. Drug Deliv. Rev.*, vol. 180, p. 114067, 2022, doi: 10.1016/j.addr.2021.114067.

[10] E. Vlaisavljevich, A. Maxwell, L. Mancia, E. Johnsen, C. Cain, and Z. Xu, “Visualizing the Histotripsy Process: Bubble Cloud–Cancer Cell Interactions in a Tissue-Mimicking Environment,” *Ultrasound Med. Biol.*, vol. 42, no. 10, pp. 2466–2477, Oct. 2016, doi: 10.1016/J.ULTRASMEDBIO.2016.05.018.

[11] A. R. Smolock *et al.*, “Robotically Assisted Sonic Therapy as a Noninvasive Nonthermal Ablation Modality: Proof of Concept in a Porcine Liver Model,” *Radiology*, vol. 287, no. 2, p. 171544, 2018, doi: 10.1148/radiol.2018171544.